



*Highly advanced Probabilistic design and Enhanced Reliability methods
for high-value, cost-efficient offshore WIND*

HIPERWIND Final Project Report: Highly advanced Probabilistic design and Enhanced Reliability methods for high-value, cost-efficient offshore WIND

Deliverable no: D7.11

Delivery date: 30-09-2024

Lead beneficiary: DTU

Dissemination level: Public



*This project has received funding from the European Union's
Horizon 2020 Research and Innovation Program under Grant
Agreement No. 101006689*

Author information (in order of affiliation):

Name	Organization	Email
Nikolay Dimitrov	DTU	nkdi@dtu.dk
Asger Bech Abrahamsen	DTU	asab@dtu.dk
Mark Kelly	DTU	mkel@dtu.dk
Moritz Gräfe	DTU	mograf@dtu.dk
Büsra Yildirim	DTU	bysyi@dtu.dk
Michael McWilliam	DTU	mimc@dtu.dk
Asta Hannesdottir	DTU	astah@dtu.dk
Athanasios Kolios	DTU	atko@dtu.dk
Mostafa Bakhoday-Paskyabi	UiB	mostafa.bakhoday-paskyabi@uib.no
Anais Lovera	EDF	anais.lovera@edf.fr
Suguang Dou	EDF	suguang.dou@edfenergy.com
Emmanuel Ardillon	EDF	emmanuel.ardillon@edf.fr
Elias Fekhari	EDF	elias.fekhari@edf.fr
Christophe Peyrard	EDF	christophe.peyrard@edf.fr
Fabien Robaux	EDF	fabien.roboux@edf.fr
Vincent Chabridon	EDF	vincent.chabridon@edf.fr
Baptiste Jezequel	EDF	baptiste.jezequel@edf.fr
Pierre Gruet	EDF	pierre.gruet@edf.fr
Jerome Longchamp	EDF	jerome.lonchamp@edf.fr
Nassif Berrabah	EDF	nassif.berrabah@edf.fr
Martin Guiton	IFPEN	martin.guiton@ifpen.fr
Mohamed Reda Al Amri	IFPEN	mohamed-reda.el-amri@ifpen.fr
Alexis Cousin	IFPEN	alexis.cousin@ifpen.fr
Pierre-Antoine Joulin	IFPEN	pierre-antoine.joulin@ifpen.fr
Marine Dupoirion	IFPEN	marine.dupoirion@ifpen.fr
Adrià Borràs Nadal	IFPEN	adria.borras-nadal@ifpen.fr
Nicolas Bonfils	IFPEN	nicolas.bonfils@ifpen.fr
Guillaume Huwart	IFPEN	guillaume.huwart@ifpen.fr
Maria Laura Mayol	IFPEN	
Miguel Munoz-Zuniga	IFPEN	miguel.munoz-zuniga@ifpen.fr
Lucas Franceschini	IFPEN	
Stefano Marelli	ETH Zurich	marelli@ibk.baug.ethz.ch
Styfen Schär	ETH Zurich	styfen.schaer@ibk.baug.ethz.ch
Clement Jacquet	EPRI	cjaquet@epri.com
Benjamin Paz	EPRI	BPaz@epri.com
Erik Vanem	DNV	Erik.Vanem@dnv.com
Christian Agrell	DNV	Christian.Agrell@dnv.com
Sebastian Winter	DNV	Sebastian.Winter@dnv.com
Simen Eldevik	DNV	

Acknowledgements/Contributions::

Matteo Capaldo	Anand Natarajan	Hai Bui
M. Mohammadpour Penchah	Marie Renner	Carla Ferreira
Hong Wang	Dheelibun Remigius	Xiaodong Zhang
Bruno Faria		

Document information:

Version	Date	Description	Prepared by	Reviewed by	Approved by
1.0	2024	Official	Authors listed above	Marie Renner N. Dimitrov	N. Dimitrov

Contents

1	Introduction and executive summary	1
2	Use cases and model definition (WP1 outcomes)	7
2.1	Use cases definition	8
2.2	Code-to-code comparison of aeroelastic tools	10
3	Uncertainty in environmental conditions (WP2 outcomes)	11
3.1	Challenges addressed in WP2	12
3.2	Multi-scale flow modelling and uncertainty quantification: scientific contributions	12
3.3	Multi-scale flow modelling and uncertainty quantification: examples of developed models and tools	14
3.3.1	Mesoscale model uncertainty mitigation: A case study	14
3.3.2	WRF-PALM wind-wave-wake model	16
3.3.3	WRF-LES wind-wake model	16
3.3.4	Wave-affected theoretical coherence function	16
3.4	Wave model uncertainty	22
3.4.1	Engineering state of the art and research models used in WP2	22
3.4.2	Wave conditions	22
3.4.3	Wave crest distribution	22
3.4.4	Wave kinematics distribution	23
3.4.5	Drag parameters distribution	23
3.4.6	Conclusions	23
3.5	Extreme transient events	31
3.5.1	Summary of results, interpretation, & conclusions	31
3.6	Joint distributions of environmental conditions	35
4	Probabilistic load assessment (WP3 outcomes)	37
4.1	Challenges addressed in WP3	38
4.2	Wind farm wake and layout parameterization	38
4.2.1	Wind farm wake effect parameterization using surrogates for local wind estimates	39
4.2.2	Wind farm wake effect parameterization using layout encoding	40
4.2.3	Turbine clustering	43
4.3	Wake model uncertainty	45
4.4	Simulation of special turbulence cases	50
4.4.1	Turbulence box generation with the Hipersim tool	50
4.4.2	Generation of non-Gaussian turbulence boxes	50
4.4.3	Impact of transient event profiles on wind turbine loads	55
4.5	Hydrodynamics model uncertainties	58
4.5.1	Approximations of MacCamy-Fuchs approach for monopiles	58
4.5.2	Uncertainty in fitting drag coefficient for floating wind turbine	58
4.6	Aerodynamics model uncertainties	63
4.7	Wake analysis for floating wind turbines	66
5	Advanced uncertainty propagation and structural reliability assessment method-	

ologies (WP4 outcomes)	68
5.1 Surrogate Modelling of High-Dimensional Input/Output Time-Series	69
5.1.1 Introduction	69
5.1.2 Problem Statement	69
5.1.3 Computational Model and Validation	69
5.1.4 mNARX autoregressive modelling	69
5.1.5 Surrogate performance	71
5.1.6 Conclusions	71
5.2 Probabilistic surrogate models using Bayesian Neural Networks	72
5.3 Data-driven model validation and updating	75
5.4 Floating wind turbine design procedure including SLS	78
5.4.1 Sensitivity analysis using an automated design evaluation framework	78
5.4.2 System Response: Time and Frequency Domain	78
5.4.3 Global Sensitivity Analysis	78
5.4.4 Serviceability Limit State Assessment	80
5.4.5 SLS evaluation	80
5.4.6 FWT design evaluation: summary and conclusions	80
5.5 Uncertainty model definition for reliability assessment	82
5.6 Reliability assessment for ULS	84
5.6.1 ULS reliability calculations for stationary conditions	84
5.6.2 ULS reliability calculations for transient conditions	86
5.7 Reliability assessment for FLS	88
5.7.1 Fatigue reliability assessment problem	88
5.7.2 Methodology (computational aspects)	88
5.7.3 Use case description: numerical simulation model, probabilistic model	88
5.7.4 Some results	89
5.8 Design utilization study and updates	91
6 Component reliability assessment (WP5 outcomes)	93
6.1 Load-based bearing degradation model	94
6.2 Wind farm reliability map	97
6.3 Validation of the bearing degradation model	98
6.4 Reliability of electrical components and effect of grid events on mechanical loads	102
6.4.1 Method overview	102
6.4.2 Results	102
6.4.3 Conclusion	104
7 Impact assessment and optimizations (WP6 outcomes)	105
7.1 Optimization of O&M scheduling	106
7.1.1 Framework of the optimization	106
7.1.2 Formulation of the optimization problem	106
7.1.3 Numerical implementation	106
7.2 O&M optimization for value	107
7.3 LCOE modelling tool and Hiperwind impact assessment	109
7.3.1 Method overview	109
7.3.2 Cost reductions from HIPERWIND improvements	109
7.3.3 LCOE results	109

8	Conclusions	114
	Acknowledgements	115
	References	115
9	Appendix: Additional resources	126
	Resources	126
9.1	List of project deliverables	127
9.2	List of software tools created in the project	129
9.3	Links to additional project resources	131
9.4	External peer-reviewed publications generated by Hiperwind as of September 2024	132

List of Figures

1.1	Illustration of the effect of uncertainty on design safety	2
1.2	Hiperwind concept	3
1.3	Overview of Hiperwind technical work packages	5
1.4	Hiperwind result highlights	6
1.5	Summary of main conclusions from Hiperwind and suggestions for further work.	6
2.1	Layout and location of the Teesside wind farm.	8
2.2	Overview of the South Brittany site. Left: site bathymetry and location of virtual wind farm (red rectangle). Right: layout of the virtual floating wind farm. Plots reproduced from Hiperwind D3.2 (Ardillon et al., 2022)	9
2.3	Illustration of code-to-code comparison results. Left: comparison of spectra of structural response at a location primarily affected by wave loads; Right: comparison of fore-aft bending moment time series for simulations with step changes in the wind speed.	10
3.1	Modified Van der Hoven’s Horizontal Wind Speed Spectrum from (Rodriguez-Hernandez et al., 2016).	13
3.2	(a) 10-minute averaged LiDAR wind speed profiles, combined with meteorological mast measurements below 100 meters, collected over a 5-day period in July 2015. (b) Time series comparison of wind speed at the 90-meter height, measured by FINO1’s cup anemometer (black line) and LiDAR (red line), with accompanying regression analysis results. (c) Time series comparison of wind direction at the 90-meter height, recorded by FINO1’s wind vane (black line) and LiDAR (red line), along with corresponding regression analysis. (d) Obukhov length (L) values, derived from sonic anemometer measurements at 15 meters above mean sea level during July 2015, are shown. These values are categorized into five stability classes, color-coded to indicate their frequency of occurrence, with the shaded red areas highlighting the study period from July 1–5, 2015. Source Bakhoday-Paskyabi and Flügge (2021).	18
3.3	Comparison of observed and modeled horizontal wind speeds at FINO1 from July 1 to 5, 2015: (a) shows LiDAR measurements, with vertical dashed lines marking the first three Low-Level Jet (LLJ) events. White gaps in the LiDAR plot represent data filtered out due to poor quality or unavailability; (b) presents WRF simulation results without Data Assimilation (DA); (c) displays WRF simulation with DA using the regional Background Error (BE) matrix (WRFDA-REGBE); and (d) shows WRF simulation with DA employing the global BE matrix (WRFDA-GLOBE). Source Bakhoday-Paskyabi and Flügge (2021).	19
3.4	(Top) Topographic height and WRF model domains are shown on the left, with the geographical locations of FINO1 and Alpha Ventus displayed on the right; and (Bottom) The model chain for the multi-scale wind-wave coupled simulation is illustrated(Ning and Bakhoday-Paskyabi, 2023).	20
3.5	Comparison of Instantaneous Wind Speed at 90 Meters Above Ground Level in the 40-Meter Domain (D05) at 08:00 UTC on September 24, 2016, Between Two Experiments, see more in (Bui et al., 2024).	20

3.6	(Top-left) Comparison of vertical wind turbulence coherence between the Davenport empirical model (Term1) and wind–wave coherence. (Top-right) Time series of the wave-affected frequency spectrum measured by the sonic anemometer. (Bottom-left) Second-order structure function estimated from both measured and wave-filtered sonic data. (Bottom-right) Measured coherence spectrum from the sonic anemometer compared to the reconstructed coherence using the developed theoretical coherence function (Bakhoday-Paskyabi, 2024).	21
3.7	Parameters of the sea states considered in this study. Here gamma refers to the peak-enhancement parameter of the JONSWAP spectrum, and λ_p and κ_p are calculated from the peak period T_p using the linear dispersion relation	23
3.8	Estimated distributions of hourly maximum crest heights from long-crested HOSM simulations, compared to relevant reference distributions	24
3.9	Estimated distributions of hourly maximum crest heights from short-crested HOSM simulations, compared to relevant reference distributions	25
3.10	-	26
3.11	-	27
3.12	-	28
3.13	-	29
3.14	Joint distribution of 10-minute $P(\dot{s}_{99} U)$ at 100 m height, for low-pass filter scales of 0.1 Hz (left) and 1/3 Hz (right). Solid line is exponential fit to $\text{mode}\{\dot{s}_{99} U\}$, gray dashed is 90th percentile, white dotted is 99th percentile, and color dash-dotted is 99.9th percentile of $P(\dot{s}_{99} U)$	32
3.15	Expected \dot{s}_{99} per return period t , for the three different filter scales considered and two heights analyzed. Thick lines correspond to $T_{\text{base}} \simeq 39$ minutes; thin lines bounding shaded area for each correspond T_{base} spanning 10–119 minutes, to indicate uncertainty.	33
3.16	Joint PDFs $P(\dot{s}_{99}, \sigma_s)$ of all 10-minute $\{\dot{s}_{99}, \sigma_s\}$ at both heights analyzed, for low-pass $f_c = \{1/10, 1/3\}$ Hz. White lines show $\text{mode}\{\dot{s}_{99} \sigma_s\}$	34
4.1	Sketch of a wind farm wake effect parameterization workflow using surrogates for local wind estimates. Diagram reproduced from McWilliam et al. (2022).	39
4.2	Illustration of turbulence field being modified by a single wake. Plots reproduced from McWilliam et al. (2022).	40
4.3	Proportion of number of wakes required to fit the vertical plane deficits for Teesside wind farm. Plot reproduced from McWilliam et al. (2022).	40
4.4	Comparison of blade flapwise DEL predictions with the surrogate model vs. reference simulations. Plot reproduced from McWilliam et al. (2022).	41
4.5	Sketch of a wind farm wake effect parameterization workflow using layout encoding. Diagram reproduced from McWilliam et al. (2022).	42
4.6	Sketch of load modelling workflow using wind farm layout encoding as surrogate model inputs. Diagram reproduced from McWilliam et al. (2022).	42
4.7	Normalized blade damage-equivalent load accumulation history for turbines at Teesside. Figure reproduced from McWilliam et al. (2022).	43
4.8	Marginal distribution for mean speed (left) and turbulence intensity (right) on floating turbines of a theoretical wind farm in South Brittany, France. Figure reproduced from Ardillon et al. (2022).	44
4.9	Mean absolute MMD errors (in percent) in wind speed and turbulence intensity over the full domain for every clustering solution for the South Brittany wind farm. Figure reproduced from Ardillon et al. (2022).	44

4.10	Figure reproduced from Ardillon et al. (2022)	45
4.11	Figure reproduced from Ardillon et al. (2022)	46
4.12	Neutral atmosphere: vertical and horizontal cuts of mean wind speed at the middle row position and at hub height, respectively. Figure reproduced from Ardillon et al. (2022)	47
4.13	Stable atmosphere: vertical (up) and horizontal (down) cuts of mean wind speed at the middle row position and hub height, respectively. The vertical lines show selected positions to extract vertical and horizontal profiles downstream of the first turbine. Figure reproduced from Ardillon et al. (2022)	48
4.14	Teesside: FarmShadow TM and DWM-HAWC2 model results: normalized mean speed difference on the left, and normalized turbulence difference on the right. Figure reproduced from Ardillon et al. (2022)	49
4.15	Figure reproduced from Ardillon et al. (2022)	49
4.16	Coherence and spectra of turbulent fields generated with the Python-based tool Hipersim, compared to analytical targets. Figure is reprinted from Dimitrov et al. (2024b)	51
4.17	Illustration of the application of constraints in Hipersim. Figure is reprinted from Dimitrov et al. (2024b)	52
4.18	Gaussian and non-Gaussian turbulence fields of the transverse velocity component.	53
4.19	Histograms of non-Gaussian velocity increments (full lines) and Gaussian fits (dashed lines) for three different separations (Δx).	53
4.20	Mean skewness (pink) and mean kurtosis (blue) as function of the C parameter for 4 turbulence simulations of different seeds. Error bars show the standard deviation.	53
4.21	Maximum Tower Bottom Bending Moment For-Aft due to non-Gaussian turbulence	54
4.22	Maximum Tower Bottom Bending Moment For-Aft due to non-Gaussian turbulence	54
4.23	The largest filtered streamwise acceleration compared to the corresponding turbulence box generated with HIPERSIM	55
4.24	The largest filtered transverse acceleration compared to the corresponding turbulence box generated with HIPERSIM	55
4.25	The different locations for placing the time series	56
4.26	Tower bottom over-turning moment statistics, due to significant stream-wise acceleration events at 100m	56
4.27	Root flapwise bending moment statistics, due to significant stream-wise acceleration events at 100m	56
4.28	Comparison of tower bottom over-turning moment time series, due to significant stream-wise acceleration events at 100m	57
4.29	Comparison of tower bottom over-turning moment time series, due to significant direction changes	57
4.30	Relative DEL error between MCF and linear Potential Flow theory (positive value means MCF produces higher DEL), for a large water depth and large TP diameter modified from Teesside case study. Figure is reprinted from Peyrard et al. (2022)	59
4.31	Relative DEL error between MCF and second-order Potential Flow theory (positive value means MCF produces higher DEL), for a large water depth and TP diameter of Teesside case study. Figure is reprinted from Peyrard et al. (2022)	59
4.32	UMaine floater sketch with components modelled by CFD in red. Figure is reprinted from Peyrard et al. (2022)	60

4.33 Neptune_cfd (colored dots), OpenFOAM® (cross and diamonds) results of L_2 fitting, compared to experiments of Venugopal (2002). Figure is reprinted from Peyrard et al. (2022).	61
4.34 Zones used to extract the Morison coefficients. Figure is reprinted from Peyrard et al. (2022).	61
4.35 Drag coefficient for zone 3, with two different extraction methods. Heave and pitch imposed motions. KC varying. Figure is reprinted from Peyrard et al. (2022).	62
4.36 3D illustration of a of wake accommodation technique with the CASTOR library Blondel et al. (2024). In the near wake, the size of the filaments (vortex elements) increases progressively (“shed merging” technique). After a transition, only the tip vortices remain to model the far wake. For this illustration, the wake has been frozen. Figure is reprinted from Peyrard et al. (2022).	63
4.37 GP std of the time averaged power from Vortex simulations, with candidates and new points selected for the second iteration of the DoE. Figure is reprinted from Peyrard et al. (2022).	64
4.38 Mean and standard deviation of GP for the time-averaged aerodynamic thrust from BEM and Vortex simulations. Teesside case study (left), South Brittany case study (right). Figure is reprinted from Peyrard et al. (2022).	65
4.39 Representation of the two nested iterative loops solving the wind field in the farm. Figure is reprinted from Ardillon et al. (2022).	66
4.40 Axial velocity profile ahead of the second rotor in the middle row depending on the wind direction. Case A (top): 8m/s, head-wind with vertical shear. Case C (middle): 11m/s, crosswind with vertical shear, Case D (bottom): 11 m/s crosswind, no vertical shear. The rotor is represented as a red dashed line. Figure is reprinted from Ardillon et al. (2022).	67
4.41 Yearly averaged farm production taking different effects into account. Figure is reprinted from Ardillon et al. (2022).	67
5.1 Graphical representation of the mNARX surrogate modelling strategy	70
5.2 Original vs. reconstructed wind field after truncating its spectral representation to the first 16 DCT modes. Left: original 2D turbulence box slice. Middle: 2D DCT coefficients. Right: reconstructed turbulence box slice after truncation.	70
5.3 Graphical representation of the performance of the mNARX surrogate for the blade root moment for a realization in the extreme operating gust out-of-sample validation set. Left: prediction (red) with high relative error with respect to the true response (black); Right: prediction (green) with low relative error with respect to the simulator output (black).	71
5.4 Comparison of epistemic (model) uncertainty and aleatory (realization-to-realization) uncertainty effects for extreme blade root flapwise bending moments. Left: scatter plots raw data including aleatory uncertainty and averages over multiple seeds (realizations) at each sample point; Center: histograms of the model uncertainty compared to the realization-to-realization uncertainty; Right: correlation between the model uncertainty and the realization-to-realization uncertainty.	72
5.5 Comparison of the probability densities of fatigue damage-equivalent load predictions from a BNN model and an ensemble of deterministic models, for six wind turbine load signals.	73
5.6 Comparison of the tail probability distribution predictions by a BNN model and an ensemble of deterministic models, for four load channels.	74

5.7	Simulation vs. field measurements. Fore-aft (left) and side-side (right) bending moment.	75
5.8	Example of time series prediction from field and simulation model, case A	76
5.9	Prediction RMSEN of simulation data-based model, tested on field measurements.	77
5.10	Flow diagram with overview of the FWT design evaluation framework	79
5.11	Overview of floater geometry and design variables considered in the evaluation framework	80
5.12	Overview of the random variables and uncertainties considered for reliability assessment. Figure reproduced from Dimitrov et al. (2024a)	82
5.13	. Estimated 50-year return values on a 2D toy problem from sequential sampling, as function of the number of Short Term simulation used to train the GP. Results from brute-force sampling and from a direct sampling contour method are also included. Figure reproduced from Cousin et al. (2024)	85
5.14	. 2D projection of the DoE used in the sequential sampling method. Figure reproduced from Cousin et al. (2024)	85
5.15	Survival plot for maximum tower base Von-Mises stress, based on different Monte-Carlo simulation configurations. Each simulation consisted of 100,000 samples. Figure reproduced from Cousin et al. (2024)	86
5.16	The direction in standard space vs. distance in standard space, for the simulations responsible for the largest stress, within the Monte-Carlo simulations. Figure reproduced from Cousin et al. (2024)	87
5.17	. Failure probability estimation with transient input wind along the active learning iterations. Figure reproduced from Cousin et al. (2024)	87
5.18	Time series of the bending moment for tower base (top) and monopile at mudline (bottom) with mean speed of 35m/s, Turbulence Intensity of 11%, yaw and wind-wave misalignments of 30°, significant wave height of 13 m and wave peak period of 43 s. Figure reprinted from Hiperwind D4.2 report (Cousin et al., 2024).	91
5.19	Profiles of the nominal design and the new design (with normalized axes). Figure reprinted from Hiperwind D4.2 report (Cousin et al., 2024).	92
5.20	Mass reduction for each part of the structure. Figure reprinted from Hiperwind D4.2 report (Cousin et al., 2024).	92
6.1	Main bearing equivalent load P_{eq} of the aeroelastic simulation representing $u = 4-26$ m/s and $I_{ref} = 0.1-0.18$. The IEC turbulence wind classes A, B and C with $I_{ref} = 0.16, 0.14$ and 0.12 are shown by dashed lines.	96
6.2	Main bearing basic lifetime L_{10y} of the aeroelastic simulation representing $u = 4-26$ m/s and $I_{ref} = 0.1-0.18$. The IEC turbulence wind classes A, B and C with $I_{ref} = 0.16, 0.14$ and 0.12 are shown by dashed lines.	97
6.3	Main bearing basic lifetime L_{10y} shown as function of the annual average wind speed v_{ave} of the Rayleigh distribution and the reference turbulence intensity I_{ref} . The IEC design wind class IIB of the SWT 2.3 - 93 turbines is shown as a dot and the annual average wind speed $v_{ave} = 7.1$ m/s of the Teesside offshore wind farm is shown as a vertical dashed line Moros et al. (2024)	98
6.4	Main bearing basic lifetime L_{10y} shown for the position of the wind turbines WT1 to WT27 (red numbers) of the Teesside wind farm in units of the turbine rotor diameter.	99

6.5	Failure probability of the main bearing of the Teesside wind farm as function of the basic lifetime L_{10y} . The horizontal dashed lines indicate a failure rate corresponding to 1, 2, and 3 out of the 27 turbines experiencing bearing failure.	100
6.6	Probability of observing a main bearing temperature in the SCADA data of the 27 SWT 2.3 - 93 turbines of the Teesside offshore wind farm in 2019 as a function of the wind speed measured at the turbines. The prediction of the main bearing temperature from the physics-based thermal model is shown in the red open circles for the reference turbulence intensities of $I_{ref} = 0.14$ corresponding to the Teesside offshore wind farm. The predicted main bearing temperatures of the range of reference turbulence intensities $I_{ref} = 0.10 - 0.18$ is also shown for comparison.	101
6.7	Active power generation during Grid voltage sag at 12m/s wind speed. The response has been simulated using an IEC-2.5MW type 4 wind turbine model in powerFactory.	102
6.8	HAWC2 response time series during Low Voltage Ride Through (LVRT) at $t = 20s$ under <i>DLC 2.4</i> with a turbulence intensity of $I_{ref} = 0.16$. Only 50 seconds out of 100 seconds are shown to highlight the features after the LVRT, whereas all 100 second time series are used for the fatigue evaluation.	103
7.1	The average revenue loss throughout the life time of the wind farm for the 104 failure scenarios. Market price case was used in the short-term optimization.	108
7.2	Increase in the market value factor throughout the life time of the wind farm for the 104 failure scenarios. Market price case was used in the short-term optimization.	108
7.3	LCOE results for the Teeside wind farm without considering HIPERWIND improvements (baseline case)	111
7.4	LCOE results for the Teeside wind farm considering all HIPERWIND improvements (optimized case)	111
7.5	LCOE results for the virtual wind farm without considering HIPERWIND improvements (baseline case)	112
7.6	LCOE results for the virtual wind farm considering all HIPERWIND improvements (optimized case)	113

List of Tables

5.1	Marginal distributions used for the Z -variables considered for the reliability analysis	89
7.1	Results for LCOE calculation for the Teesside wind farm both for the baseline and optimized case.	110
7.2	Results for LCOE calculation for the virtual wind farm both for the baseline and optimized case.	112
9.2	List of dedicated software tools developed during the project	130

List of Abbreviations

AK	Adaptive Kriging
AEP	Annual Energy Production
ARMA	Auto Regressive Moving Average
ASE	Aero Servo Elastic
BEM	Blade Element Momentum method
BoP	Balance of Plant
BNN	Bayesian Neural Network
CAPEX	Capital Expenditure
CCD	Central Composite Design
CfD	Contract for Difference
CFD	Computational Fluid Dynamics
DCT	Discrete Cosine Transform
DEL	Damage Equivalent Load
DLB	Design Load Basis
DLC	Design Load Case
DOE	Design of Experiment
DWM	Dynamic Wake Meandering
EDC	Extreme Direction Change
EOG	Extreme Operating Gust
FNN	Feedforward Neural Network
FWT	Floating Wind Turbine
FLS	Fatigue Limit State
GP	Gaussian Process
HOS(M)	High-Order Spectral (Method)
IEC	International Electrotechnical Committee
LCOE	Levelized Cost of Energy
LES	Large Eddy Simulation
LHS	Latin Hypercube Sampling
LiDAR	Light Detection And Ranging
LLJ	Low Level Jet
LVRT	Low Voltage Ride-Through
MCF	MacCamy-Fuchs correction
MCR	Major Component Replacement
MMD	Maximum Mean Discrepancy
OPEX	Operating Expenses
O&M	Operations and Maintenance
ULS	Ultimate Limit State
SCADA	Supervisory Control And Data Acquisition
SLS	Serviceability Limit State
SO	Specific Objective
TP	Transition Piece
WP	Work package
WRF	Weather Research and Forecasting
WT	Wind Turbine

1 Introduction and executive summary

HIPERWIND (Highly advanced Probabilistic design and Enhanced Reliability methods for high-value, cost-efficient offshore WIND) is a research project funded by EU’s Horizon2020 program under Grant Agreement number 101006689. Hiperwind answered the LC-SC3-RES-31-2020 call: Offshore wind science and balance of plant. The project activities took place between December 2020 and September 2024. This document provides a summary of the scientific results from the project and highlights important findings. Parts of the document include references and extracts from project deliverable reports or associated scientific publications, including reproduction of key figures. The reader is referred to the other project publications for full details on the scientific work. These publications are listed in section 9.1 (Deliverable reports) and section 9.4 (Scientific papers).

The overall objective of HIPERWIND is achieving a **9% reduction in the Levelized Cost of Energy** of offshore wind farms, through advancements of basic wind energy science which will lead to **reductions in risk and uncertainty**.

A key focus area of Hiperwind is managing uncertainties. Uncertainties translate into higher safety margins (see illustration in Figure 1.1), adding materials to components, shorter maintenance cycles, and increases in the cost of financing wind farms. Uncertainty management is consequently a driver in reducing costs and improving the production, reliability, and thereby the value of offshore wind.

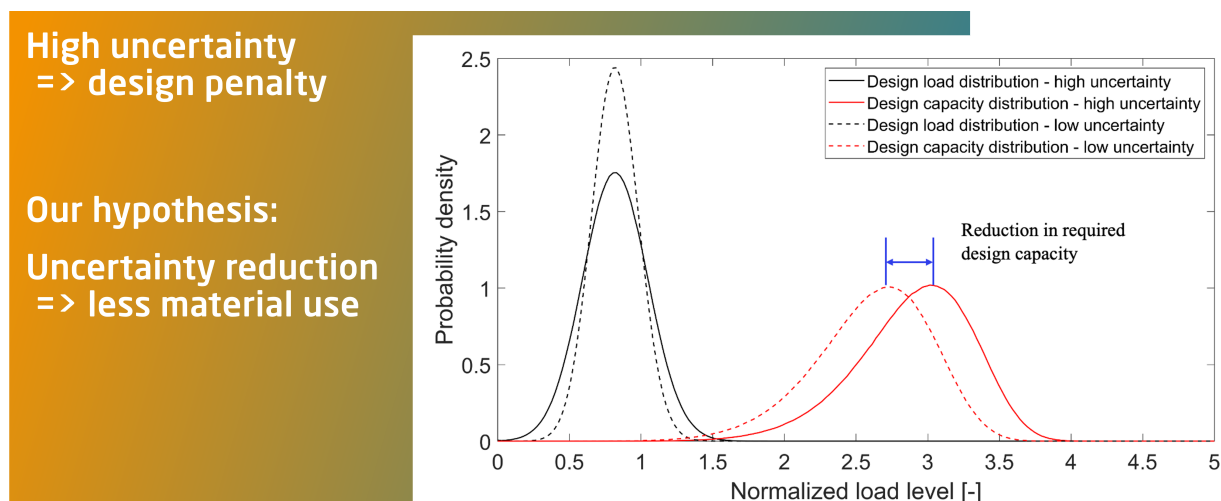


Figure 1.1: Illustration of the effect of uncertainty on design safety

Leveraging measured data and advanced physics-based and data-driven models, this uncertainty management and reduction philosophy is applied throughout the offshore wind turbine design modelling chain. The specific project objectives include:

- **SO1:** Improve the accuracy and spatial resolution of met-ocean models and quantify key uncertainties in environmental conditions that affect offshore wind farm design and operation, including wind resource, wind turbulence, waves, and their interactions, and joint probability distributions – to achieve a 30% total reduction of uncertainty in environmental exposure (WP2).
- **SO2:** Develop novel load assessment methods tailored to the dynamics of large offshore fixed-bottom and floating wind turbines, realistically capturing complex phenomena such as fluid-structure interaction, wake effects and transient weather events, thus leading to a

30% reduction in load assessment uncertainty (WP3).

- **S03:** Develop an efficient reliability computation framework, treating uncertainties in a consistent way and making full-scale probabilistic design approach feasible (WP4).
- **S04:** Develop and validate the modelling framework for degradation of offshore wind turbine components due to loads and environment, to establish representative design load criteria for major components and enable reduction in maintenance costs (WP5).
- **S05:** Prioritize concrete, quantified measures that result in LCOE reduction of at least 9% and market value improvement of 1% for offshore wind energy, based on the developed new technologies (WP6).

The HIPERWIND concept for delivering these objectives (Figure 1.2) establishes a sequential strategy: improved modelling of environmental conditions, leading to improved load predictions, which in turns leads to better reliability assessment and lower uncertainty, resulting in more cost-efficient design and operations, for more cost-efficient and higher-value offshore wind. Uncertainty quantification and reduction through advanced physical models that are supplemented with measurements is a cross-cutting theme across all work packages covering the entire project. In the design phase, the uncertainty reduction results in a more efficient use of materials, together with a reduction in engineering studies needed for the development of a given offshore wind farm. In the operation phase, uncertainty reduction means lower operating risk, increased energy production, and less unscheduled maintenance.

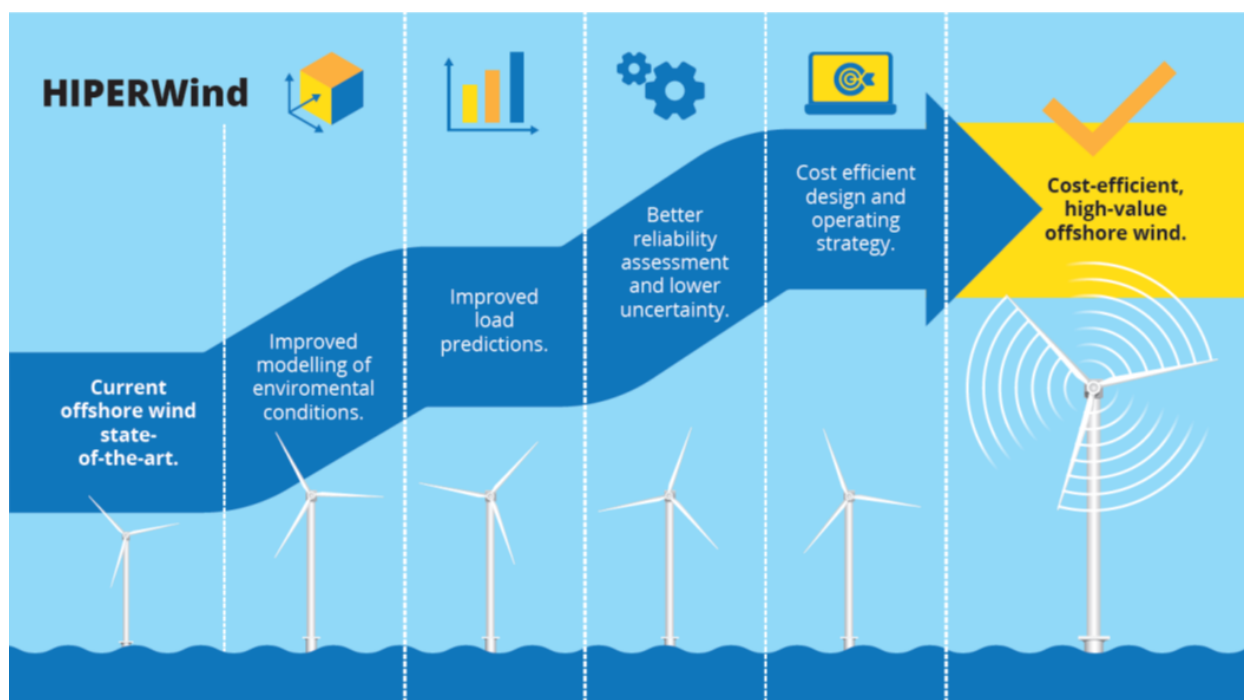


Figure 1.2: Hiperwind concept

The scientific work in Hiperwind is distributed in six technical work packages. Figure 1.3 illustrates some of the key activities, and the scopes of the individual work packages are briefly outlined below.

- **WP1 Data Acquisition and Case Study Definition:** WP1 provides essential inputs to ensure timely start of other project activities. The available measurement data are

formatted into useable samples for other work packages. The aero-hydro-servo-elastic models of the turbines to be studied are defined, and are used to build an initial set of aero-hydro-servo-elastic simulations allowing work on lifetime and reliability models (WP4 and WP5) to begin before WP2 and WP3 are complete.

- **WP2 Environmental Condition Modelling:** WP2 aims towards fulfilling SO1. This is achieved by improving multiscale flow modelling of the atmospheric boundary layer (from mesoscale to microscale) using available observational data and modelling tools, to efficiently understand and model the key global uncertainties and relevant physical processes for the offshore wind energy design and operation. A coupled ocean-atmosphere-wave-sediment transport (COAWST) modelling system, integrated with a wave atmospheric boundary layer mode, is used to identify and quantify important and potentially not-well-resolved processes in the air-sea interaction. Data assimilation is employed in order to reduce the propagation of boundary errors. Additional focus is given to wave modelling, where nonlinear wave models are deployed to study the wave propagation and interactions for extreme wave realizations. The wave spectral evolution during extreme events is identified and quantified. Finally, the joint statistics of environmental wind and wave parameters and their corresponding uncertainties are quantified, feeding as inputs to WPs 3-6. The advanced modelling techniques supplemented with data provide a reduction of uncertainty which is propagated further in the modelling chain to the wind turbine design.
- **WP3: Farm and Turbine Loads Modelling** WP3 constitutes the main effort towards achieving SO2. The main objective is to develop novel load analysis techniques, to allow characterizing and reducing the uncertainties which are constituents of the reliability computations for ultimate and fatigue designs in WP4 and WP5. In contrast to WP2 where the focus is purely on the environment on kilometre scales down to wind farm scales, WP3 introduces the wind farm in the landscape and focuses on the phenomena taking place within a wind farm and down to turbine level due to their interactions with the environment. This includes realistic modelling of wake interactions, structural response of wind turbines to aerodynamic and hydrodynamic loading under stationary conditions, and the effect of transient events on wind turbine loads.
- **WP4: Life Assessment of Wind Turbine Structures** The main objective of WP4 is to develop and validate mathematical models for structural reliability, which will enable probabilistic design in practice in line with SO3 while maintaining consistency with the design load case approach currently used in international design standards IEC61400-1 and IEC61400-3. This capability will also allow the demonstration of the effect of the uncertainty reduction efforts carried out in WP2 and WP3, on the design reliability. The results are compared against the current design practise, which is the partial safety factor-based design approach, and thereby the reduction in uncertainty and conservatism is quantified.
- **WP5: Life Assessment of Wind Turbine Components** This Work Package focuses on achieving SO4. It develops and validates a modelling framework which estimates the effect of environmental conditions and operating strategy on the reliability of main bearings. The choice of bearings as focus of the study is dictated by the significant downtime caused by frequent bearing failures combined with lengthy repair actions, leading to large expenses, further exacerbated offshore due to the difficulty of access. The demonstration and validation of this model should pave the way for a shift in O&M strategy, where the effect of loading on component degradation is taken into account and the operation is adjusted

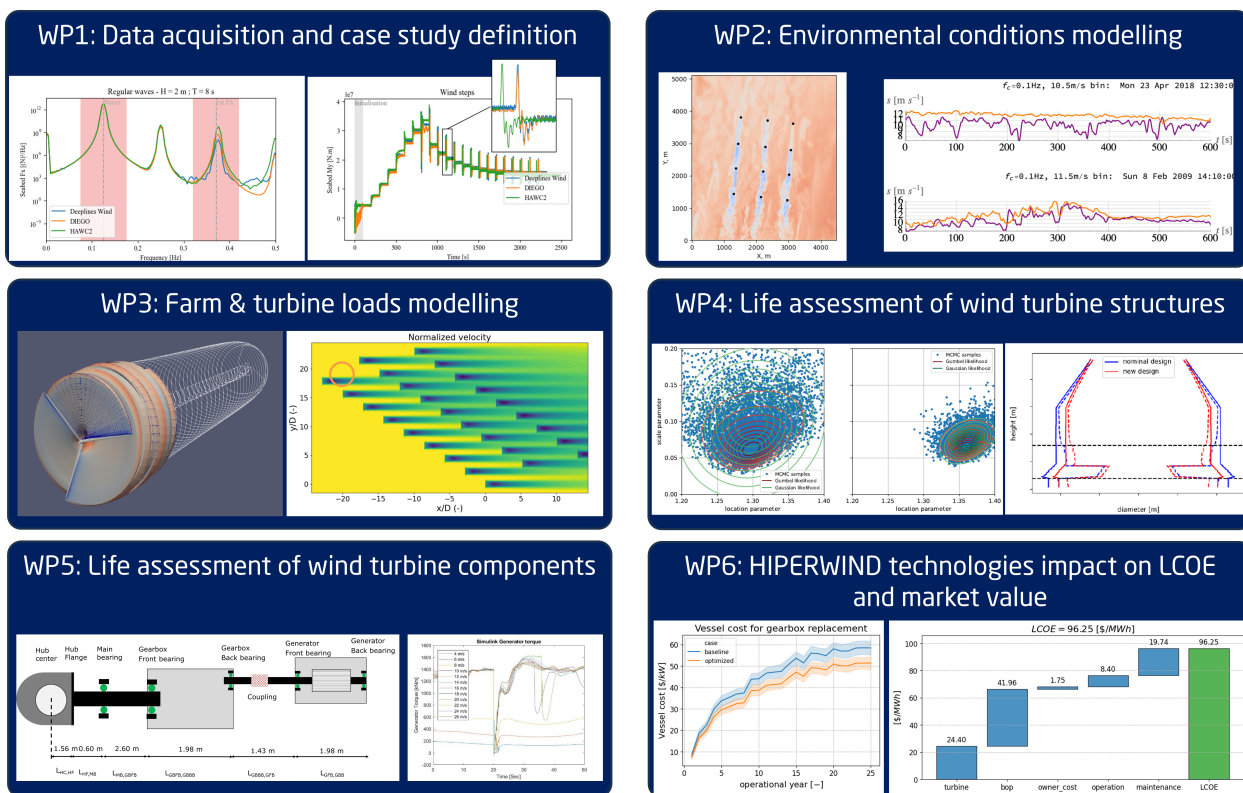


Figure 1.3: Overview of Hiperwind technical work packages

accordingly, to reduce the possibility for unscheduled failures, or increase performance in situations with low impact on reliability.

The reliability estimation is based on detailed component models, which use the load assessments produced in WP3 as inputs, and estimate the material deterioration using physics-based degradation laws. These models are used, together with measured wind turbine load data, to identify reasons for component health degradation under specific turbine operating conditions. The calibrated model for estimating probability of failure vs. turbine operational years conditional on operating conditions serves as input to WP6.

- WP6: Impact on LCOE and Market Value** The primary objective of WP6 is utilising the impact opportunities created in WPs 2-5, quantifying the expected effects, and evaluating them with respect to the targets set by SO5. A risk-based O&M model will be developed, which uses the improved component reliability modelling established in WP5, to devise O&M strategies which minimize financial risk. A cost uncertainty propagation model is developed, which computes the effect of the uncertainties quantified in WP2 and WP3 on the uncertainty in power production, fatigue life, and subsequently LCOE. A methodology will be developed to assess the value of wind farm assets depending on their O&M strategy and the state of the electricity market. A final impact assessment is carried out to quantitatively verify how the technological achievements of HIPERWIND transform into market value improvement and reduction of LCOE.

A short overview with the Hiperwind result highlights is given in Figure 1.4. The primary conclusions from the project, along with several areas where further work is necessary are outlined in Figure 1.5

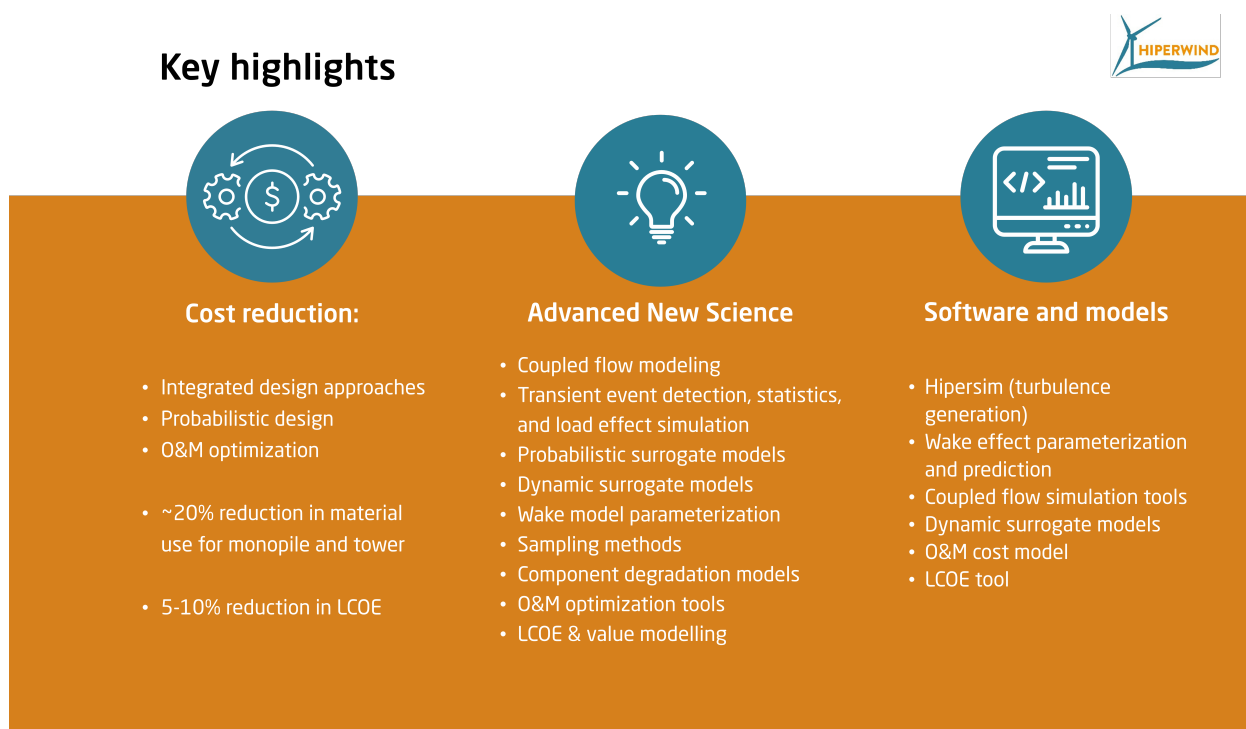


Figure 1.4: Hiperwind result highlights

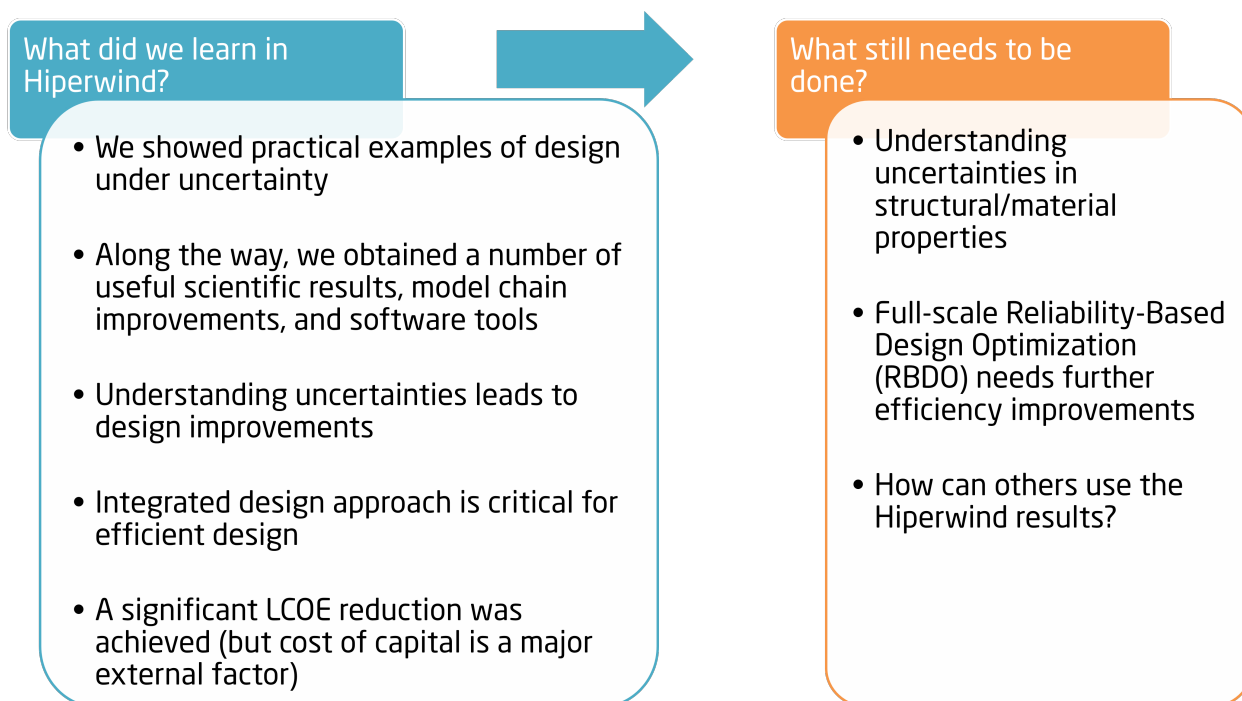


Figure 1.5: Summary of main conclusions from Hiperwind and suggestions for further work.

2 Use cases and model definition (WP1 outcomes)

2.1 Use cases definition

Hiperwind considers two primary use cases:

- 1) The operating Teesside bottom-fixed offshore wind farm located east of the river Tees estuary in the United Kingdom. Teesside has 27 SWT2.3-93 (Siemens 2.3MW with 93m rotor) wind turbines mounted on monopiles at relatively shallow water depth. The wind farm layout and a map of the farm vicinity are shown in Figure 2.1. Several years of SCADA data along with met mast measurements and wind turbine aeroelastic model data are available to partners.
- 2) South Brittany: floating wind turbines (FWTs) placed at a virtual site south of the coast of the Brittany peninsular in France (Figure 2.2). The water depths at this location are in the order of 60-150m. An area of the site with greater water depth is chosen in order to make it more suitable for the floating wind turbine technology studied in the project. The environmental conditions at the site are based on the ANEMOC reanalysis database (Tiberi-Wadier et al., 2016), which contains 20 years of hindcast data for the metocean conditions in the region. For the asset model, we use the Umaine semi-submersible floater concept Allen et al. (2020) together with the IEA 15MW reference wind turbine Gaertner (2020). Some additional details on the aeroelastic model of the floating wind turbine are given in Capaldo et al. (2021), and in Kim et al. (2022) where an aeroelastic code-to-code comparison is carried out. A large part of the studies in Hiperwind are carried out on a single FWT model which is sufficient for assessing uncertainty in e.g., hydrodynamic load models. The tasks in Deliverable 3.2 (Ardillon et al., 2022) however required a scenario with an entire virtual wind farm in order to evaluate wake interactions. A simple rectangular wind farm layout with spacing of 5 to 7 rotor diameters was chosen (Figure 2.2, right plot).



Figure 2.1: Layout and location of the Teesside wind farm.

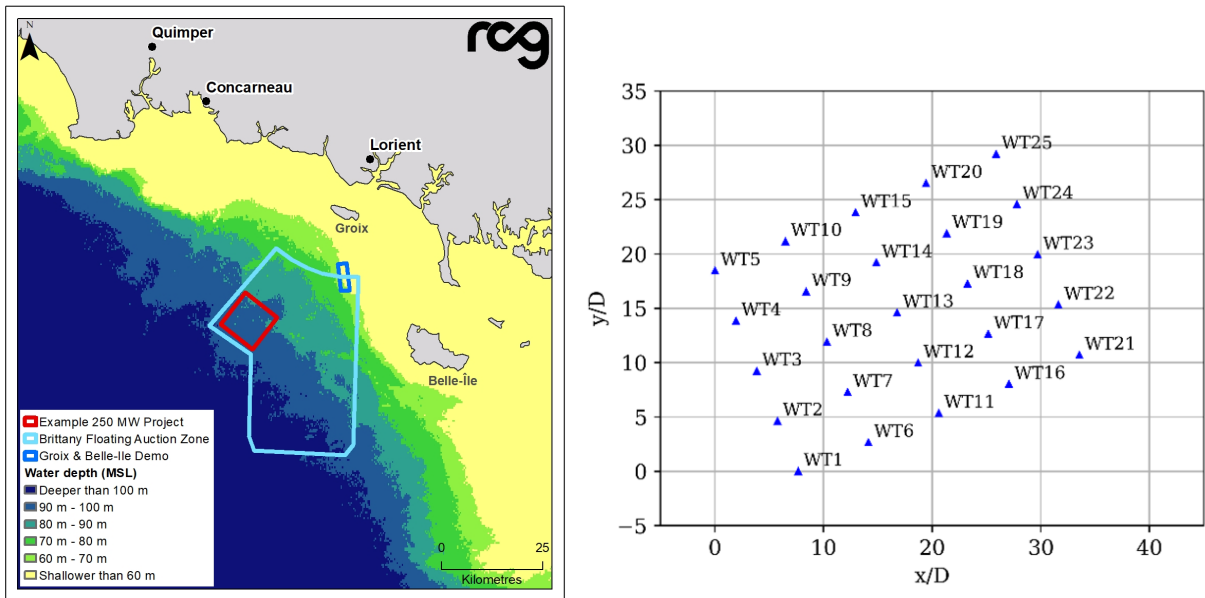


Figure 2.2: Overview of the South Brittany site. Left: site bathymetry and location of virtual wind farm (red rectangle). Right: layout of the virtual floating wind farm. Plots reproduced from Hiperwind D3.2 (Ardillon et al., 2022)

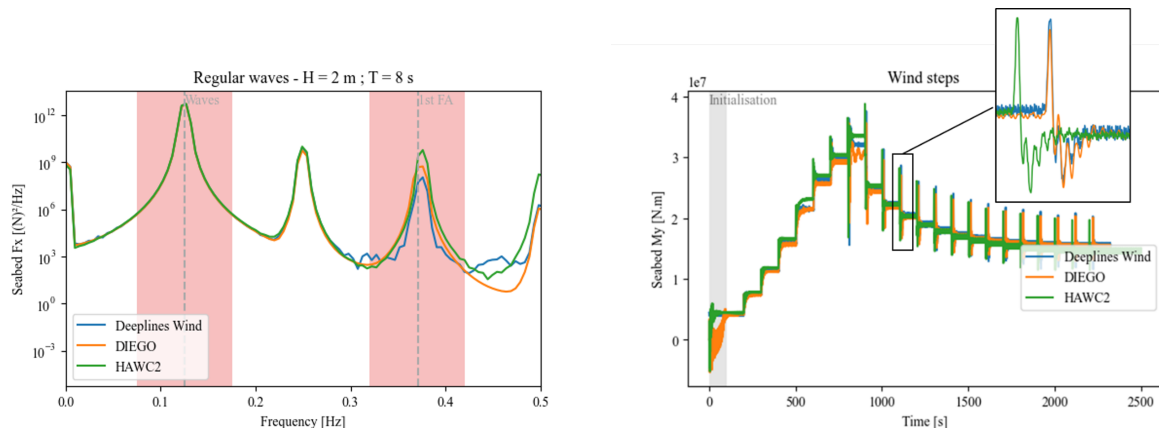


Figure 2.3: Illustration of code-to-code comparison results. Left: comparison of spectra of structural response at a location primarily affected by wave loads; Right: comparison of fore-aft bending moment time series for simulations with step changes in the wind speed.

2.2 Code-to-code comparison of aeroelastic tools

Three different proprietary aeroelastic load simulation tools are available to project partners: DTU uses the HAWC2 software (Larsen and Hansen, 2023), EDF use the DIEGO tool (Milano et al., 2019), while IFPEN use DeeplinesWind (Le Cunff et al., 2013). Each tool is proprietary and deeply integrated in the respective partners' modelling workflows, making it impractical to replace with a common tool. Instead, a thorough code-to-code comparison and validation was carried out, to ensure that results are consistent across codes, and that conclusions based on simulations with any of the three aeroelastic codes are representative.

Code-to-code comparisons were carried out for both use cases (fixed-bottom and floating). The aeroelastic models were used to simulate several predefined load scenarios with exactly the same inputs and boundary conditions simulated in each tool. The general comparison results showed excellent agreement for the Teesside use case, and a similarly good agreement in most scenarios for the floating wind turbine case. Two of the test scenarios are illustrated in Figure 2.3 - a comparison of the spectra of wind turbine response excited by waves (left side of the figure), and a comparison of the transient response for a case of step changes in the wind speed (right hand side plot). A detailed overview of the code-to-code comparison for the South Brittany floating wind turbine case is given in Kim et al. (2022).

3 Uncertainty in environmental conditions (WP2 outcomes)

3.1 Challenges addressed in WP2

The profitability of wind farms throughout their lifecycle depends on a variety of factors, including the structural design of turbines, optimization of wind farm sites and layouts, and effective wind farm control. All these aspects are closely linked to a comprehensive understanding of wind, wave, and wake flow fields and the complex interactions between them.

Work Package 2 of the HIPERWIND project focuses on exploring these factors in detail, specifically aiming to reduce uncertainties in environmental modeling. For offshore wind energy systems, environmental uncertainties are driven by the dynamic and constantly changing conditions to which turbines and wind farms are exposed. One major challenge in the expansion of wind energy projects is however the limited understanding of flow field variations, particularly in the case of large offshore wind farms. The interactions between wind turbines and the thermally stratified atmospheric boundary layer become particularly significant for large wind farms, operating under different atmospheric stability conditions and extreme weather events. Additionally, current engineering models struggle to accurately represent crucial factors that affect wind farm power production, such as wake and blockage effects.

One other major challenge is the interaction between wind and waves, which significantly influences wind resources but is often oversimplified or excluded in many resource assessment studies. Fortunately, recent advancements have improved the understanding and incorporation of these interactions.

Additionally, wake effects — regions of reduced wind speed and increased turbulence downstream of turbines — are a key cause of power losses in wind farms. As individual turbine wakes merge, they create an extended area of reduced momentum, which impacts the efficiency of the entire wind farm. While traditional models simplify wake interactions, more advanced techniques like wake steering (yaw control) and induction control offer potential solutions. These methods allow front-row turbines to reduce power output, thereby improving performance in downstream turbines by either weakening (induction control) or deflecting (yaw control) the wakes. Optimizing these strategies can enhance overall wind farm performance, especially when supported by accurate environmental data regarding wind speeds and turbulence properties.

3.2 Multi-scale flow modelling and uncertainty quantification: scientific contributions

To tackle the aforementioned challenges, WP2 focuses on three tasks that involve developing and applying methodologies to quantify and mitigate environmental modeling uncertainties. Key achievements of WP2 within environmental (flow) modelling include:

- Development of two novel multi-scale model chains, ranging from mesoscale down to microscale (i.e. Fig. 3.1) and structural turbine level responses ([Bakhoday-Paskyabi et al., 2022b](#); [Bakhoday-Paskyabi and Flügge, 2021](#); [Bakhoday-Paskyabi et al., 2022a](#); [Bui et al., 2024](#); [Ning and Bakhoday-Paskyabi, 2024, 2023](#)).
- Incorporation of large eddy simulation (LES) models, such as the Parallelized Large Eddy Simulation (PALM) ([Bakhoday-Paskyabi et al., 2022b](#)) and Weather Research and Forecasting (WRF) models, for more realistic simulations of turbine wakes and turbulence. More specifically, we developed the Simple Actuator Disc for Large Eddy Simulation (SADLES), an advanced wind turbine wake model, implemented within the Weather Research

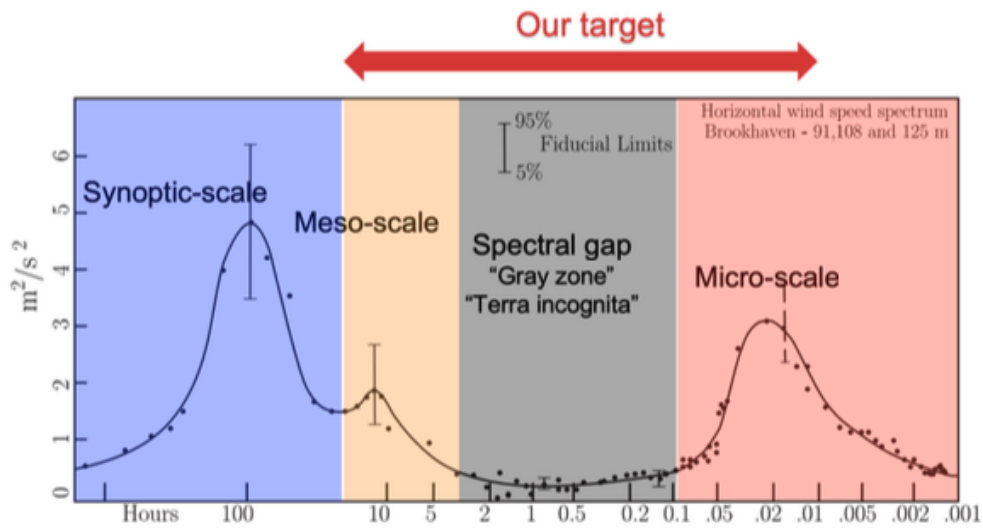


Figure 3.1: Modified Van der Hoven's Horizontal Wind Speed Spectrum from (Rodriguez-Hernandez et al., 2016).

and Forecasting (WRF) model. While still under development, this tool is designed to provide more accurate simulations of turbine wakes under various atmospheric conditions. The initial source code has been made publicly accessible for the WRF user community, contributing to open science initiatives (Bui et al., 2024).

- Creation of an offline wind-wave interaction module, allowing for in-depth studies of wind-wave interactions.
- Development of a theoretical wave-affected coherence function to integrate wind-wave interactions into the turbulence wind generation process, specifically for structural analysis studies. This allows for more accurate and physics-informed modeling of wind turbulence by considering the influence of wave dynamics, enhancing the reliability of simulations used in structural assessments of offshore wind turbines (Bakhoday-Paskyabi, 2024).
- Employment of data assimilation techniques to improve mesoscale predictions, integrating available observations for better alignment with real-world conditions (Bakhoday-Paskyabi and Flügge, 2021; Bakhoday-Paskyabi et al., 2022a).
- Providing multiple validated model and reanalysis datasets to support other tasks and WPs within the project.

It is worth to mention that although LES models are computationally intensive for real-time farm operations, they are highly valuable for design-time validation and simulation of turbine-to-turbine interactions. As such, the WP2 modelling framework not only reduces environmental uncertainties but also provides a more comprehensive understanding of wake effects, wind-wave interactions, and wind farm control strategies. This offers significant improvements for the future operation and design of offshore wind farms.

3.3 Multi-scale flow modelling and uncertainty quantification: examples of developed models and tools

3.3.1 Mesoscale model uncertainty mitigation: A case study

The mesoscale models and specifically the WRF model experiences various uncertainties, including initial condition, model structural, parameterization, boundary condition, data quality, numerical, and output uncertainties. Data Assimilation (DA) addresses these issues by integrating real-time observational data to refine initial conditions, optimize parameterization, and improve forecast accuracy. Techniques such as observational nudging, 3D Variational (3DVAR), and Ensemble Kalman Filter (EnKF) facilitate continuous updates, helping to minimize errors and enhance model reliability. Overall, effective DA may significantly improve the WRF model's predictive capabilities in weather and atmospheric simulations. Here, we will provide a brief summary of the 3DVAR method utilizing Light Detection and Ranging (LiDAR) measurements.

Over the past decade, wind LiDARs have gained widespread acceptance in wind energy applications for mapping wind fields with high precision. These measurements provide high-resolution data, offering fine temporal and spatial resolutions (e.g., range gate ≤ 25 m and frequencies up to 0.04 Hz), which are critical for understanding atmospheric boundary layer dynamics, including phenomena such as Low-Level Jets (LLJs), wind shear, and veer. Recently, researchers have employed LiDAR data to improve the prediction of LLJs by assimilating these observations into Numerical Weather Prediction (NWP) models, such as the Weather Research and Forecasting (WRF) model. Data Assimilation (DA) techniques enhance the accuracy of prognostic variables by integrating high-quality observational data. Given the intermittent nature of wind, improving wind forecasts through DA and probabilistic models is essential for bolstering the reliability of power systems.

In this study, we utilize the WRF model to simulate offshore wind patterns in the North Sea, focusing on the area around the FINO1 research platform ([Bakhoday-Paskyabi and Flügge, 2021](#)). Our key objectives are to address two main questions: (1) Does the assimilation of LiDAR measurements improve the forecast accuracy of the WRF model for simulations conducted at moderately coarse horizontal resolutions? (2) To what extent does LiDAR data assimilation enhance the prediction of lower Marine Atmospheric Boundary Layer phenomena, such as Low-Level Jets (LLJs)?

We implemented and applied two distinct types of Data Assimilation (DA): nudging and three-dimensional variational DA (3DVAR). For the sake of brevity, this report focuses exclusively on 3DVAR, and we direct the reader to [Bakhoday-Paskyabi et al. \(2022b\)](#) for further details on the nudging approach. We utilize 10-minute averaged data from cup anemometers and wind vanes collected during July 2015. To minimize the effects of severe flow distortion, wind data from directions approximately between $310^\circ \pm 30^\circ$ were excluded from the analysis. For the assimilation process in the WRF model, LiDAR data from the OBLEX-F1 measurement campaign, conducted at the FINO1 platform between May 2015 and October 2016, were utilized. Notably, several instances of Low-Level Jets (LLJs) were recorded in July 2015, with peak wind speeds observed between 200 and 300 meters above mean sea level at FINO1 (Fig. 3.2).

A comparison between the interpolated LiDAR data at 90 meters and corresponding wind speed measurements from the FINO1 cup anemometer at the same height shows a strong correlation, with a coefficient of $r \geq 0.93$, indicating excellent agreement and a slope near 1, alongside an average wind speed offset of 1.38 m/s. Furthermore, Fig. 3.2c presents the time series

of wind direction, comparing the interpolated LiDAR readings at 90 meters with the wind vane measurements at FINO1, demonstrating consistency in directional data. Lastly, Fig. 3.2d displays the time series of atmospheric stability during July 2015 and the broader study period.

The 3DVAR assimilation framework in WRF optimally combines background field data and observational inputs by minimizing a cost function, as described by Barker (2019):

$$J(x) = \frac{1}{2}(x - x_b)^T B^{-1}(x - x_b) + \frac{1}{2}(y - y_o)^T R^{-1}(y - y_o).$$

In this framework, the analysis field is represented by the vector x , the background state by x_b , and the observations by y . The background and observation error covariance matrices are denoted by B and R , respectively, where R is assumed diagonal, indicating no correlations between measurements. The observation vector $y_o = H(x)$, obtained by applying the operator H , transforms the model variables x into observation space, typically through linear interpolation from the model's 3D grid to observation points.

In this study, we utilize two methods for defining the background error covariance matrix B : the global default matrix and a computationally efficient NMC method (Bakhoday-Paskyabi and Flügge, 2021). In the NMC approach, B is estimated as:

$$B = (\overline{x_{24h} - x_{12h}})(\overline{x_{24h} - x_{12h}})^T.$$

Here, x_{12h} and x_{24h} refer to 12-hour and 24-hour forecast states, and the overbar indicates an average over time and space.

Three experiments were conducted from July 1 to 5, 2015, during periods of strong Low-Level Jet (LLJ) events observed by LiDAR: WRFDA-GLOBE (with a global background error matrix), WRFDA-REGBE (using a regional background error matrix), and WRF-NODA (without Data Assimilation, DA). The DA experiments employed a one-hour cycling assimilation process, with a 12-hour spin-up preceding the model runs. Post-spin-up WRF output was used to initialize the DA experiments. The regional background error covariance matrix was derived using the National Meteorological Center (NMC) method. Only horizontal wind speed and direction data from LiDAR measurements were used as control variables for DA. The analyses focused on the WRF grid point closest to the FINO1 site (54.0148618N, 6.5876398E). Figure 3.3 presents wind speed data from all simulations, extracted at the nearest WRF grid point to FINO1, spanning from the surface to 500 meters. The observed horizontal wind speeds at FINO1 during July 1–5 reveal three distinct Low-Level Jet (LLJ) events: a prolonged LLJ from July 1–2, followed by two shorter LLJs on the afternoon of July 2 and around midnight on July 3 (Fig. 3.3a). A weaker LLJ occurred around noon on July 4, although LiDAR data for this event is sparse. Another brief event appeared in the afternoon of July 5.

The WRF-NODA model generally overestimates wind speeds, particularly under stable atmospheric conditions (see Fig. 3.2d). Additionally, WRF-NODA struggles to accurately capture the timing and characteristics of the July 2 and July 3 LLJ events. In contrast, simulations with WRFDA demonstrate better agreement with LiDAR observations in terms of key metrics, including mean difference, wind speed vertical profiles, and root mean square error. Notably, the WRFDA-GLOBE simulation closely matches LiDAR data, outperforming WRF-NODA. Although minor discrepancies in the timing of the July 5 event (ranging from minutes to hours) may arise from grid interpolation at FINO1's location.

3.3.2 WRF-PALM wind-wave-wake model

In this work, we developed a multi-scale simulation framework for marine atmospheric boundary layer flows by integrating the meso-scale WRF-SWAN model with the micro-scale LES model PALM, see Fig. 3.4 (Bakhoday-Paskyabi et al., 2022b). This nested approach allows for the detailed simulation of offshore wind under realistic sea state conditions and varying atmospheric stability. We thoroughly examine the model's sensitivity to different wave roughness parameterizations by analyzing their impact on mean wind profiles, turbulence characteristics, and spectral behavior, comparing the results with observational data (Ning and Bakhoday-Paskyabi, 2023). Further details regarding the development of this methodology and the associated tools can be found here Bakhoday-Paskyabi et al. (2022a).

3.3.3 WRF-LES wind-wake model

In this section, we briefly present the implementation of the Simple Actuator Disc Large Eddy Simulation (SADLES) model within the Weather Research and Forecasting (WRF) system (Fig. 3.5). Unlike previous wind turbine parameterizations such as the General Actuator Disc (GAD) model (Mirocha et al., 2014; Kale et al., 2022), SADLES leverages the power and thrust coefficient curves already utilized in the Wind Farm Parameterization (WFP) (Fitch et al., 2012). This allows SADLES to simulate turbine wakes more explicitly in nested downscaling applications from mesoscale to turbine-scale resolution, targeting a balance between WFP's coarse representation and the GAD's higher complexity.

SADLES models wind turbines as thin discs that induce thrust forces, decelerating the wind to create wakes. Although the model assumes uniform thrust coefficients, which limits the detailed turbulence and tangential velocity components behind turbines, turbulent kinetic energy is implicitly captured, affecting the wake structure. Compared to the PALM LES model (Bakhoday-Paskyabi et al., 2022b,a), WRF-SADLES achieves more realistic wake representation at various grid resolutions, particularly between 10-m and 30-m scales. We applied SADLES in a real-data simulation, downscaling ERA5 data from 31 km to a turbine-scale resolution of 40 meters using a five-domain nested setup. In this experiment, limited interaction between turbines within the Alpha Ventus wind farm was observed, but a nearby wind farm led to a 14% reduction in ambient wind speed and a 35% decrease in turbine power.

One current limitation of SADLES is that it assumes the actuator disc is always perpendicular to the wind flow, restricting its ability to simulate wake deflection. Future improvements may include refining wake representation through Turbulent Kinetic Energy (TKE) and incorporating wake deflection to explore turbine yaw control strategies.

3.3.4 Wave-affected theoretical coherence function

Understanding spatial coherence and separating wave-coherent structures from wind measurements are essential for accurately generating turbulence data used in structural load analysis models, optimizing wind turbine and wind farm control systems, and simulating wind-wave interactions during swell conditions. We therefore analyzed near-surface wind and wave measurements obtained during the OBLEX-F1 campaign at the FINO1 offshore meteorological mast (met mast) in June 2015. Utilizing these data, we investigated turbulent structures within the Wave Boundary Layer (WBL) and examined the interactions between wind stress and waves under varying atmospheric stability and sea-state conditions (Bakhoday-Paskyabi, 2024). Additionally, we calculated

the momentum fluxes induced by swell, drawing from both established theoretical models and high-frequency observational data. The work specifically addressed the following key objectives:

- Evaluating the impact of swell on atmospheric velocity and two-point coherence structures during swell-dominated conditions, including the development of a theoretical model to represent wave-induced coherence.
- Applying a spectral technique to eliminate wave-induced peaks from wind velocity spectra and reconstruct turbulence and wave time series from sonic anemometer data affected by wave interference, particularly under predominantly stable atmospheric conditions.

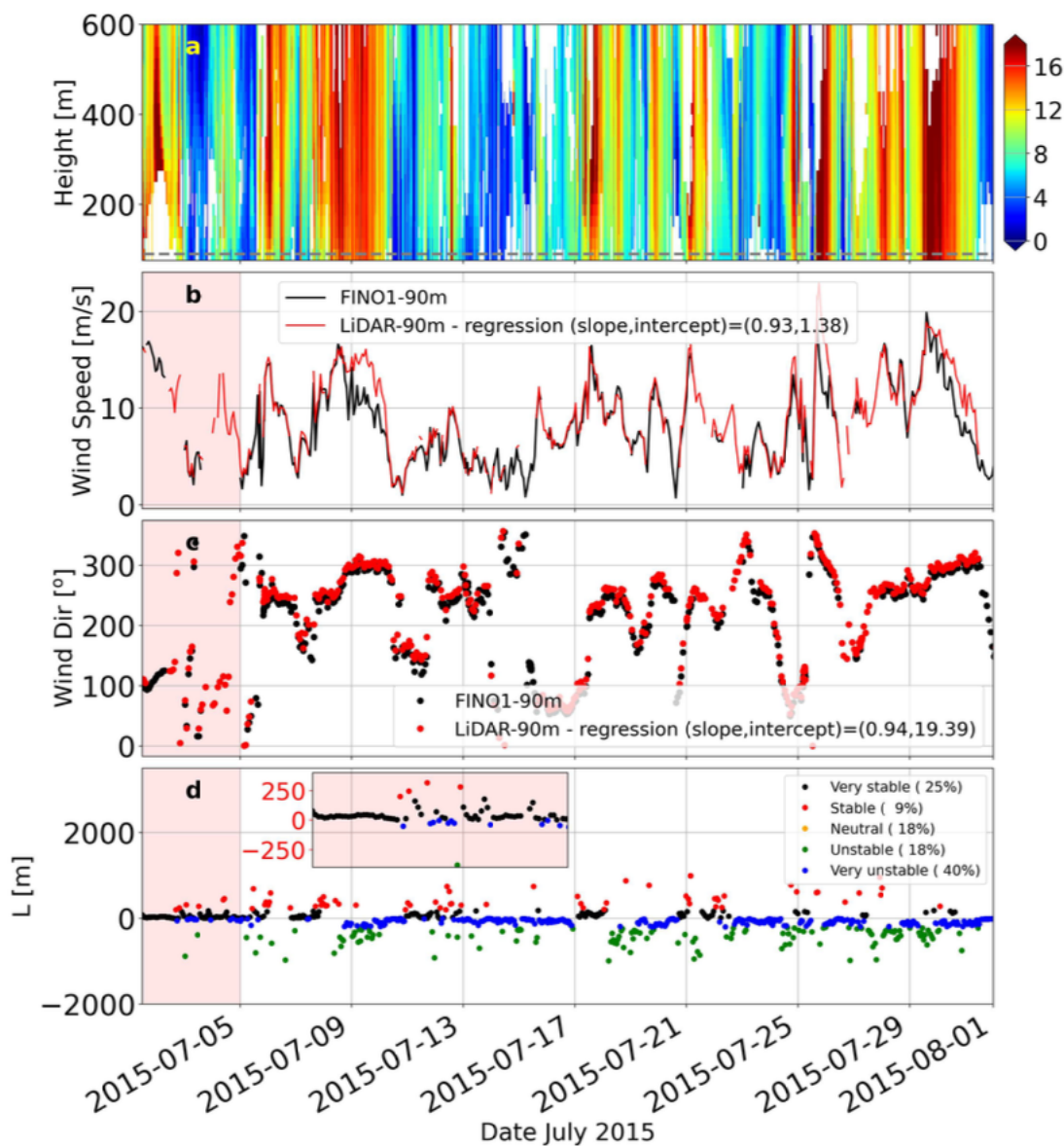


Figure 3.2: (a) 10-minute averaged LiDAR wind speed profiles, combined with meteorological mast measurements below 100 meters, collected over a 5-day period in July 2015. (b) Time series comparison of wind speed at the 90-meter height, measured by FINO1’s cup anemometer (black line) and LiDAR (red line), with accompanying regression analysis results. (c) Time series comparison of wind direction at the 90-meter height, recorded by FINO1’s wind vane (black line) and LiDAR (red line), along with corresponding regression analysis. (d) Obukhov length (L) values, derived from sonic anemometer measurements at 15 meters above mean sea level during July 2015, are shown. These values are categorized into five stability classes, color-coded to indicate their frequency of occurrence, with the shaded red areas highlighting the study period from July 1–5, 2015. Source [Bakhoday-Paskyabi and Flügge \(2021\)](#).

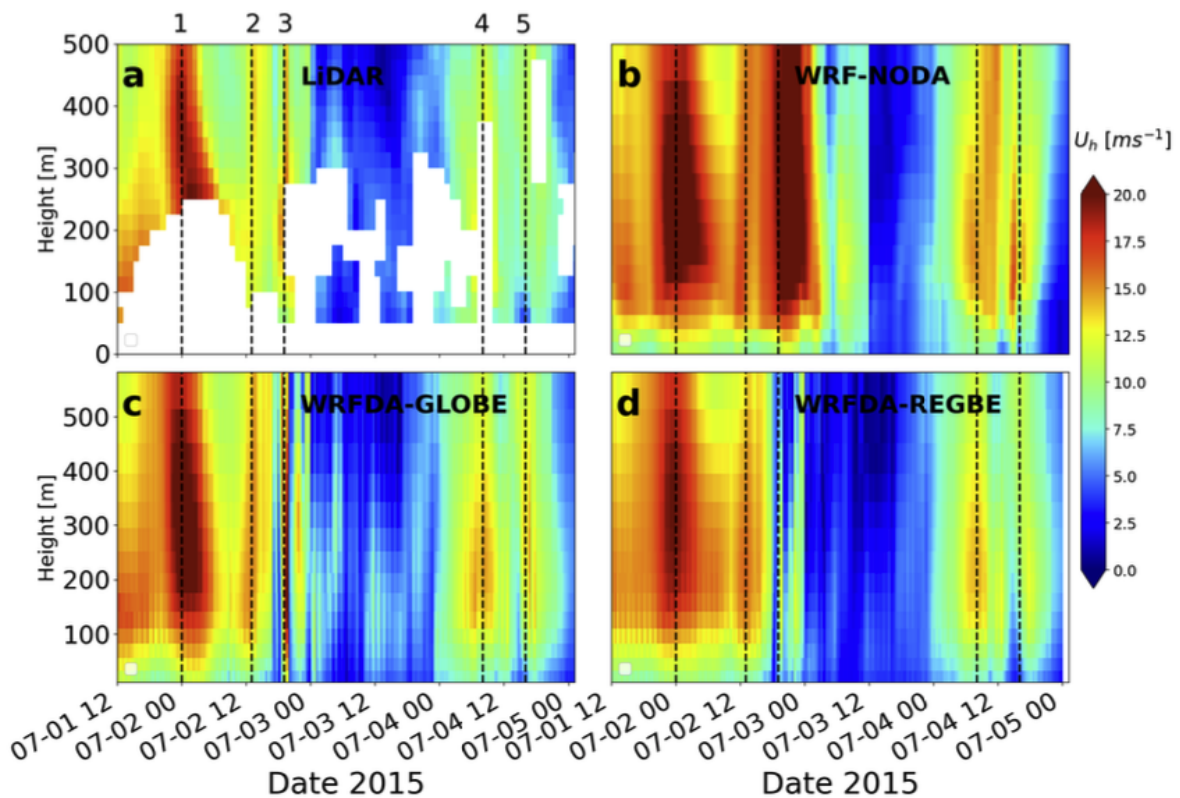


Figure 3.3: Comparison of observed and modeled horizontal wind speeds at FINO1 from July 1 to 5, 2015: (a) shows LiDAR measurements, with vertical dashed lines marking the first three Low-Level Jet (LLJ) events. White gaps in the LiDAR plot represent data filtered out due to poor quality or unavailability; (b) presents WRF simulation results without Data Assimilation (DA); (c) displays WRF simulation with DA using the regional Background Error (BE) matrix (WRFDA-REGBE); and (d) shows WRF simulation with DA employing the global BE matrix (WRFDA-GLOBE). Source [Bakhoday-Paskyabi and Flügge \(2021\)](#).

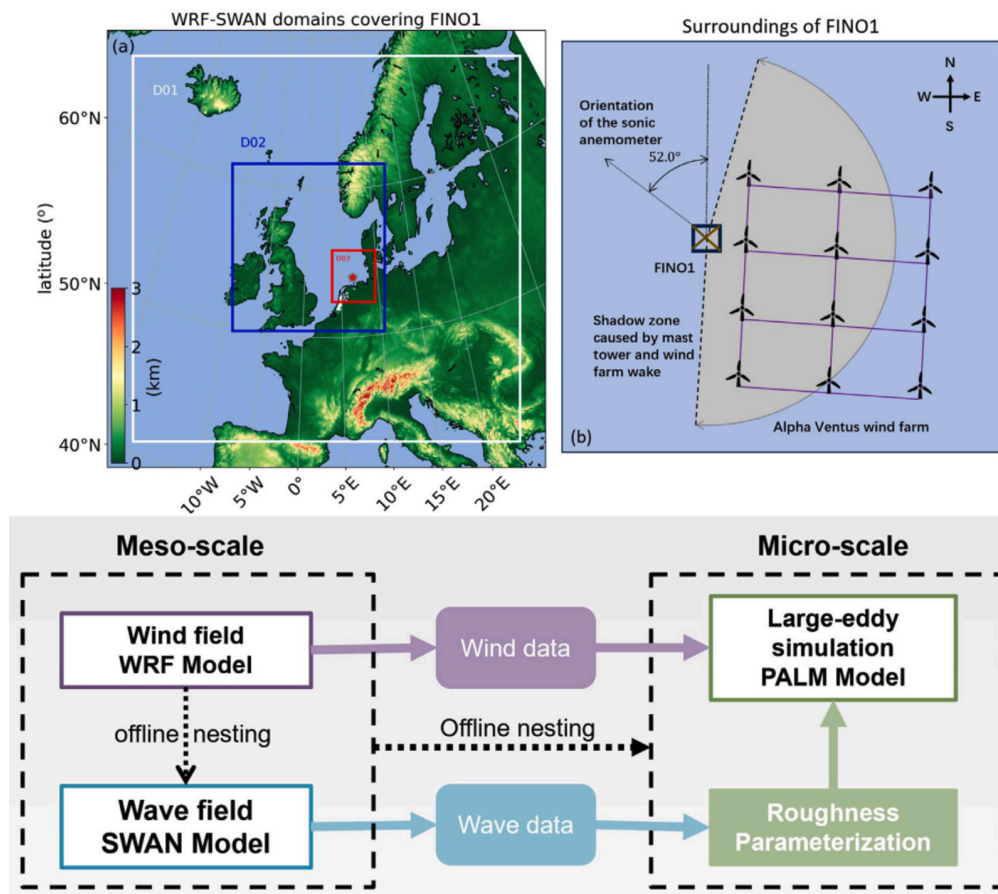


Figure 3.4: (Top) Topographic height and WRF model domains are shown on the left, with the geographical locations of FINO1 and Alpha Ventus displayed on the right; and (Bottom) The model chain for the multi-scale wind-wave coupled simulation is illustrated (Ning and Bakhoday-Paskyabi, 2023).

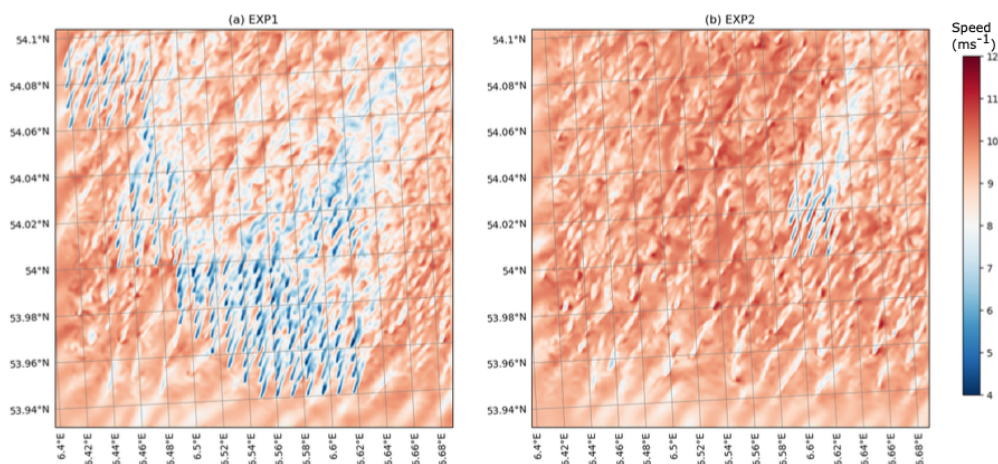


Figure 3.5: Comparison of Instantaneous Wind Speed at 90 Meters Above Ground Level in the 40-Meter Domain (D05) at 08:00 UTC on September 24, 2016, Between Two Experiments, see more in (Bui et al., 2024).

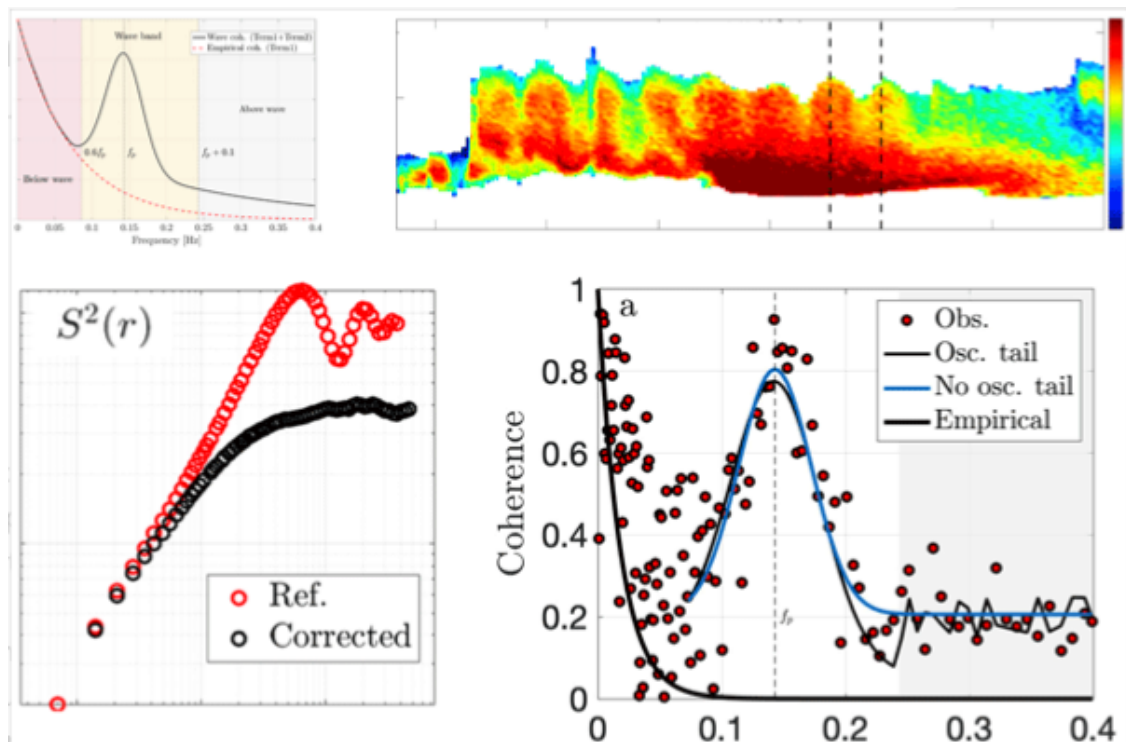


Figure 3.6: (Top-left) Comparison of vertical wind turbulence coherence between the Davenport empirical model (Term1) and wind-wave coherence. (Top-right) Time series of the wave-affected frequency spectrum measured by the sonic anemometer. (Bottom-left) Second-order structure function estimated from both measured and wave-filtered sonic data. (Bottom-right) Measured coherence spectrum from the sonic anemometer compared to the reconstructed coherence using the developed theoretical coherence function (Bakhoday-Paskyabi, 2024).

3.4 Wave model uncertainty

This section derives from deliverable D2.2 (Benoit et al., 2023).

3.4.1 Engineering state of the art and research models used in WP2

In design-oriented models the wave field is generally represented as irregular, using a linear model (Airy Waves) (Molin, 2023). Linear waves are fast to compute and thus, produce an efficient way to model the wave induced forces on bottom fixed or floating foundations. However the Airy model relies on strong hypothesis, making it unable to compute kinematics in large wave conditions or to capture the free surface elevation asymmetries. The objective of task 2.4 was to quantify the uncertainties associated to the Airy model by comparing to higher fidelity models, under wave conditions relevant for the HIPERWIND project.

In total, three families of wave models have been considered in this work:

- Linear potential models (Calhypso), consisting in using the Airy model along with multiple variations of the free surface stretching models (Wheeler, 1969). Stretching models are empirical correction used to derive wave kinematics in the crest of irregular Airy waves, commonly used in any design-oriented codes.
- High order spectral (HOS) methods ((Dommermuth and Yue, 1987) (West et al., 1987) (Seiffert et al., 2017)), suitable for highly efficient nonlinear simulation of waves in rectangular period domains with constant water depth. Two different numerical implementations of the method were used: denoted HOSM (developed by DNV), and Cosmhos (developed by EDF).
- A Boussinesq-like multilayer model (Popinet, 2020), suitable for simulation of waves in more complex domains with variable complex bathymetry (developed by DNV).

The existing DNV HOSM code as well as the EDF Cosmhos code have been extended with a wave-breaking model, providing improved description of steep sea states in which wave breaking plays a role (see (Seiffert and Ducrozet, 2017)). Extensive validation of HOSM with the newly implemented breaking model has been carried out through comparison with model-test data for long- and short-crested irregular sea states, and through direct comparison of wave crests and wave kinematics from full CFD simulations. EDF Cosmhos has been compared to long-crested focused breaking waves experimental data ((Seiffert et al., 2017), (Barthelemy et al., 2018)).

3.4.2 Wave conditions

The wave conditions used for the uncertainties evaluations have been taken from the 2 base cases identified in the WP1 : Teesside shallow waters and South-Brittany deep waters. A severity index both for fatigue and ultimate response of the foundations have been computed and a focus was made on the most critical conditions, given on Fig. 3.7.

3.4.3 Wave crest distribution

A well-known deviation due to the linear assumption is the underestimation of the crest heights. Crest heights plays a significant role in the nonlinearity of the overturning moment applied by waves on monopiles for instance, thus are a relevant parameter to focus on. A comparison

	H_s [m]	T_p [s]	γ [-]	h [m]	λ_p [m]	$k_p h$ [-]	H_s/h [-]	$H_s k_p/2$ [-]
Brittany Fatigue (BF)	2.5	6.5	3.00	150	66.0	14.29	0.017	0.119
Brittany Severe (BS)	12.5	16.5	1.46	150	416.0	2.27	0.083	0.094
Teesside Fatigue (TF)	2.0	6.0	3.00	17	54.1	1.97	0.118	0.116
Teesside Severe (TS)	10.0	15.0	1.34	17	183.9	0.58	0.588	0.171

Figure 3.7: Parameters of the sea states considered in this study. Here gamma refers to the peak-enhancement parameter of the JONSWAP spectrum, and λ_p and κ_p are calculated from the peak period T_p using the linear dispersion relation

has been made using the HOSM DNV code, both for long crested waves (Fig. 3.8) and for short crested waves (Fig. 3.9) showing the method capability to capture the wave asymmetries, where the linear models fails at predicting the highest crests. Differences were quantified and a sensitivity to the breaking wave threshold was made by DNV.

3.4.4 Wave kinematics distribution

Kinematics are the direct drivers of the waves loads. The Morison equation, often used for bottom fixed foundations, uses directly the kinematics to derive the loads. For large floating foundations the link is not so straight-forward, however the wave acceleration is a good indicator of the wave dynamic pressures applied on the foundations. Therefore, a detailed analysis of the kinematics has been performed within HIPERWIND. Variations obtained using linear models under different assumptions like stretching models (see Fig 3.10) or directional spreading (see Fig 3.12). In addition, the accuracy of the linear theory has been challenged against the HOS method implemented in the EDF code Cosmhos(Fig 3.11). The level of uncertainties introduced by the limitations of the numerical models and the choice in the modelling parameters depending on various sea conditions have been discussed.

3.4.5 Drag parameters distribution

DNV has put a specific effort on the characterization of horizontal velocities in the water column and in the crest of irregular waves. The quantity $I_{u^{**2}}$ defined as the integral of the horizontal velocity squared in the crest has been computed by the HOS method (DVN code HOSM) and a full Navier-Stokes resolution of the problem using the comflow solver. The comparison, presented on Fig 3.13, showed that the agreement is quite good in the least steep sea states, but the deterministic agreement is relatively poor in steep sea states. This may be expected since the HOSM is not able to describe the actual breaking process of the waves correctly. It is interesting to note, however, that HOSM results are conservative in the steeper sea states.

3.4.6 Conclusions

After a validation of several nonlinear wave models based on the High Order Spectral method (HOS), a quantification of uncertainties due to the modelling assumptions made in design-oriented codes have been proposed. While the range of validity of the linear theory is often considered as being $H_s/\lambda_p \in [0\%, 1\%]$, valuable information is also obtained at higher relative wave height,

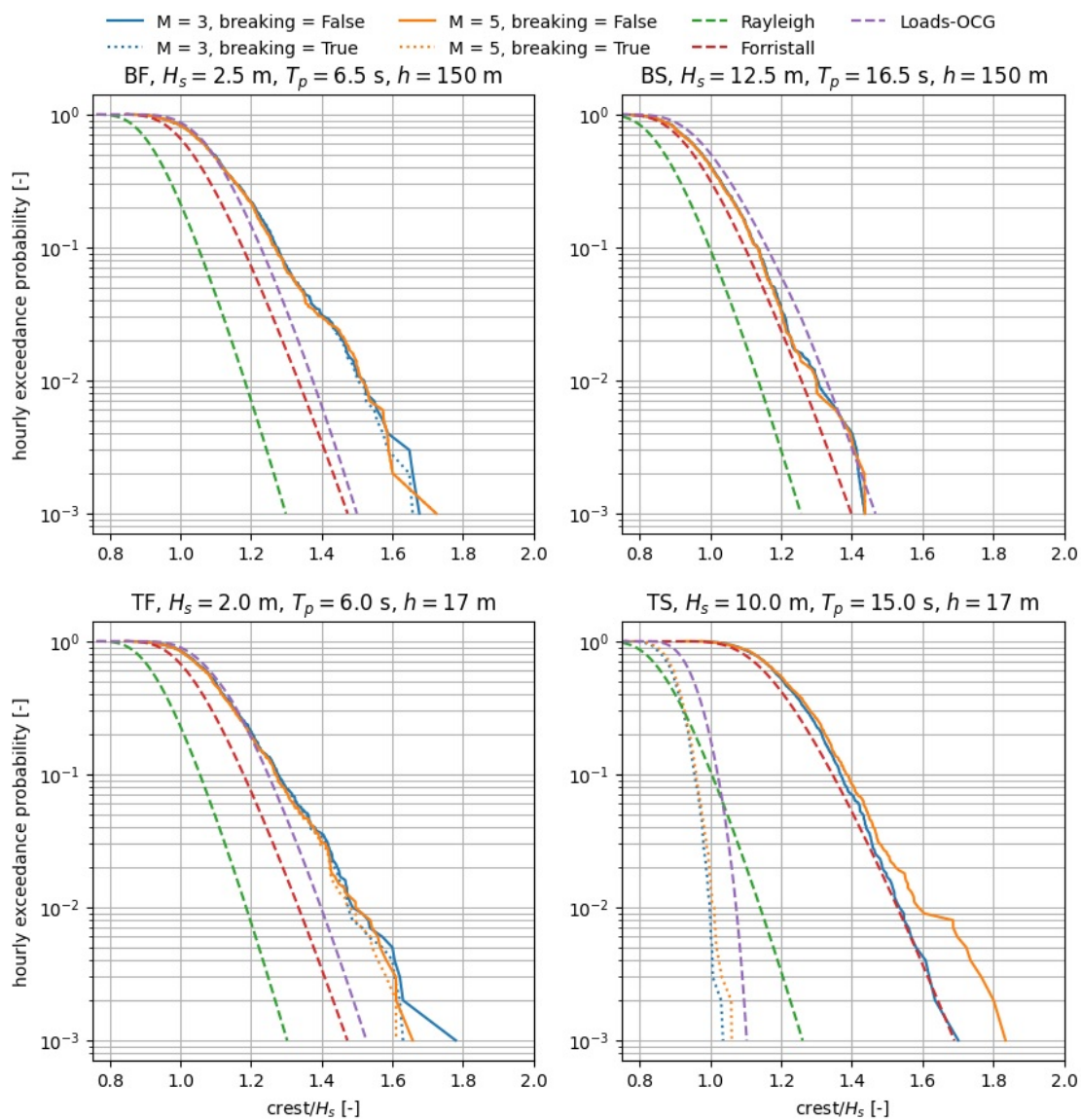


Figure 3.8: Estimated distributions of hourly maximum crest heights from long-crested HOSM simulations, compared to relevant reference distributions

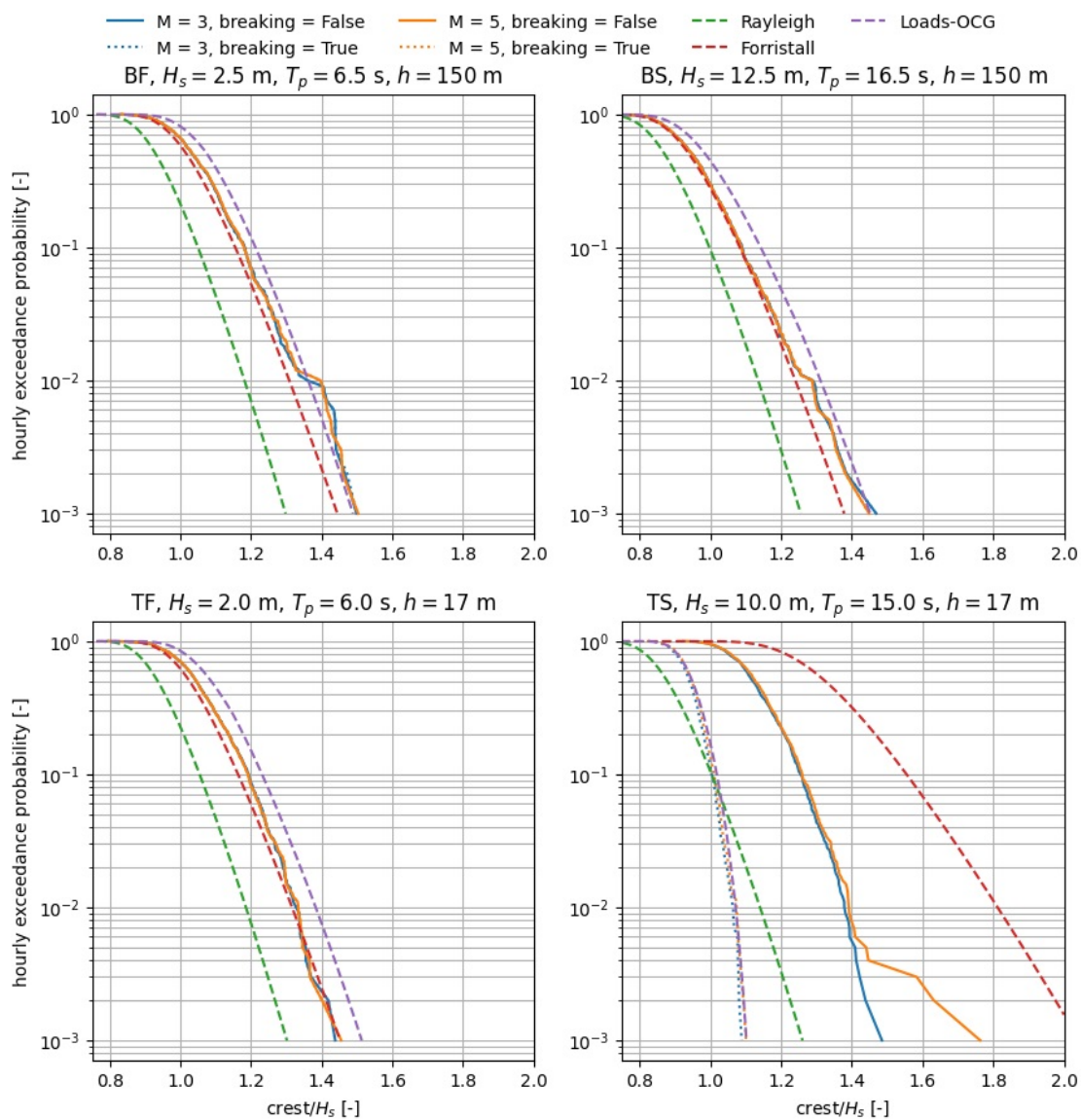


Figure 3.9: Estimated distributions of hourly maximum crest heights from short-crested HOSM simulations, compared to relevant reference distributions

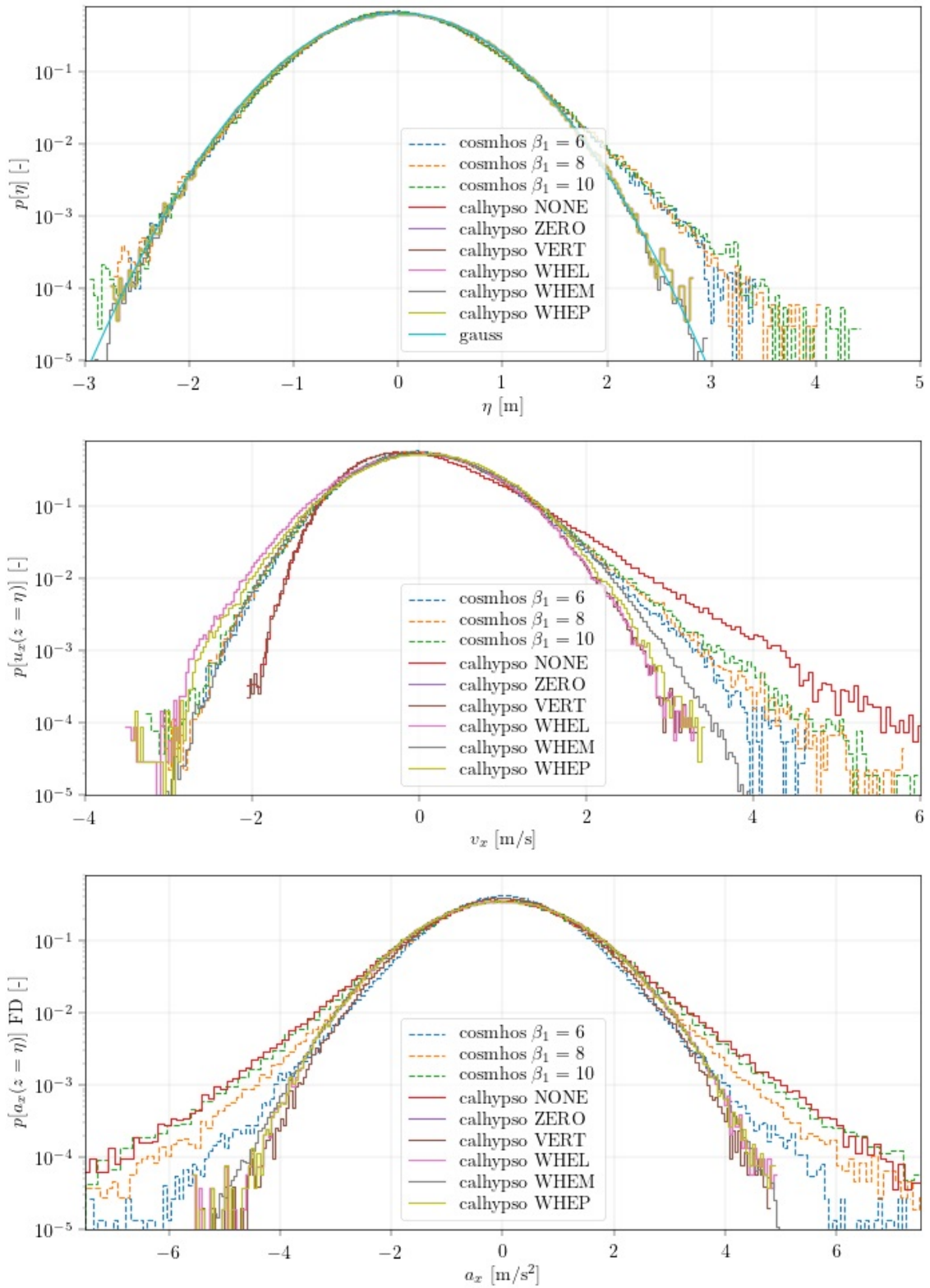


Figure 3.10: -

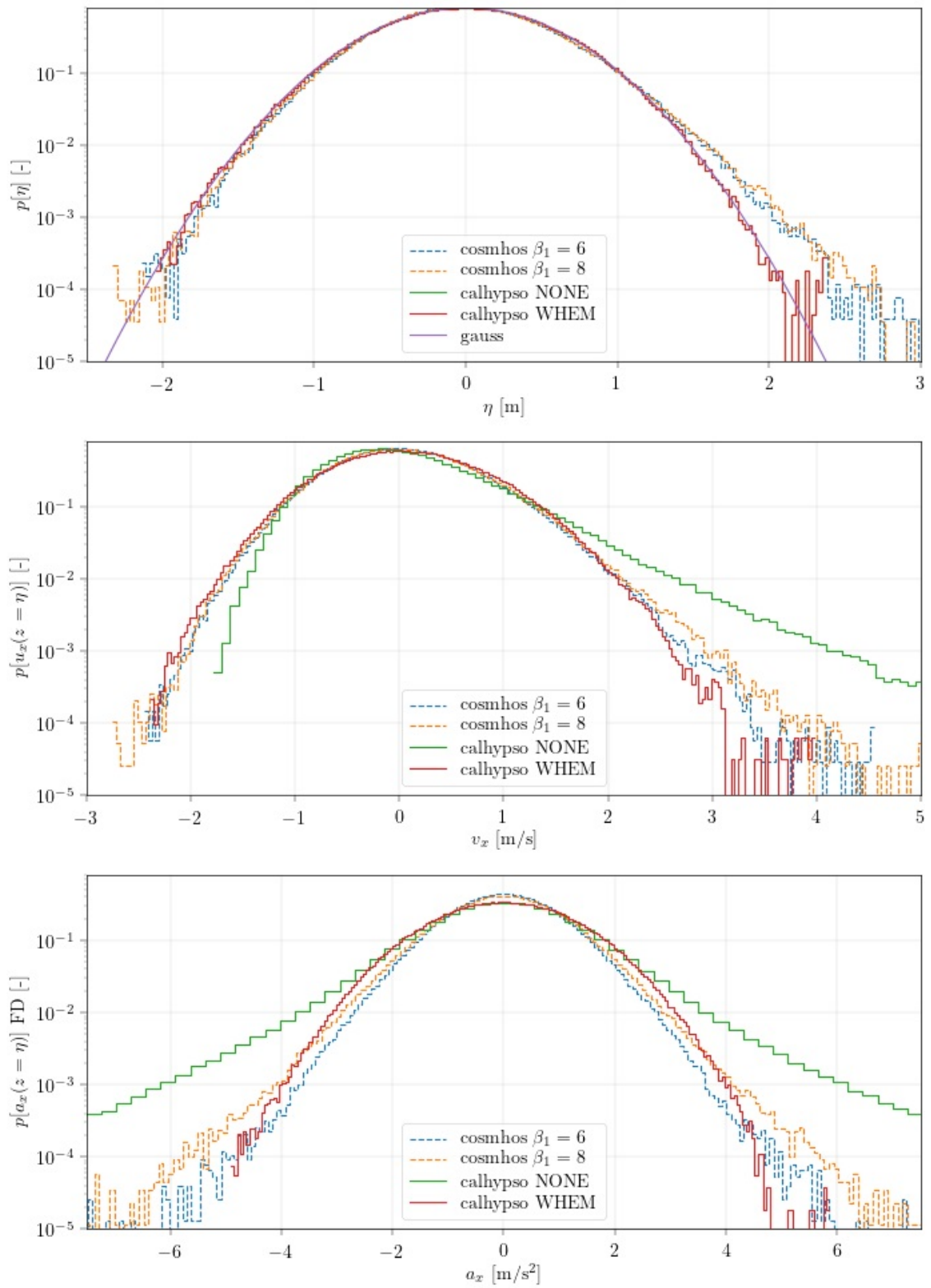


Figure 3.11: -

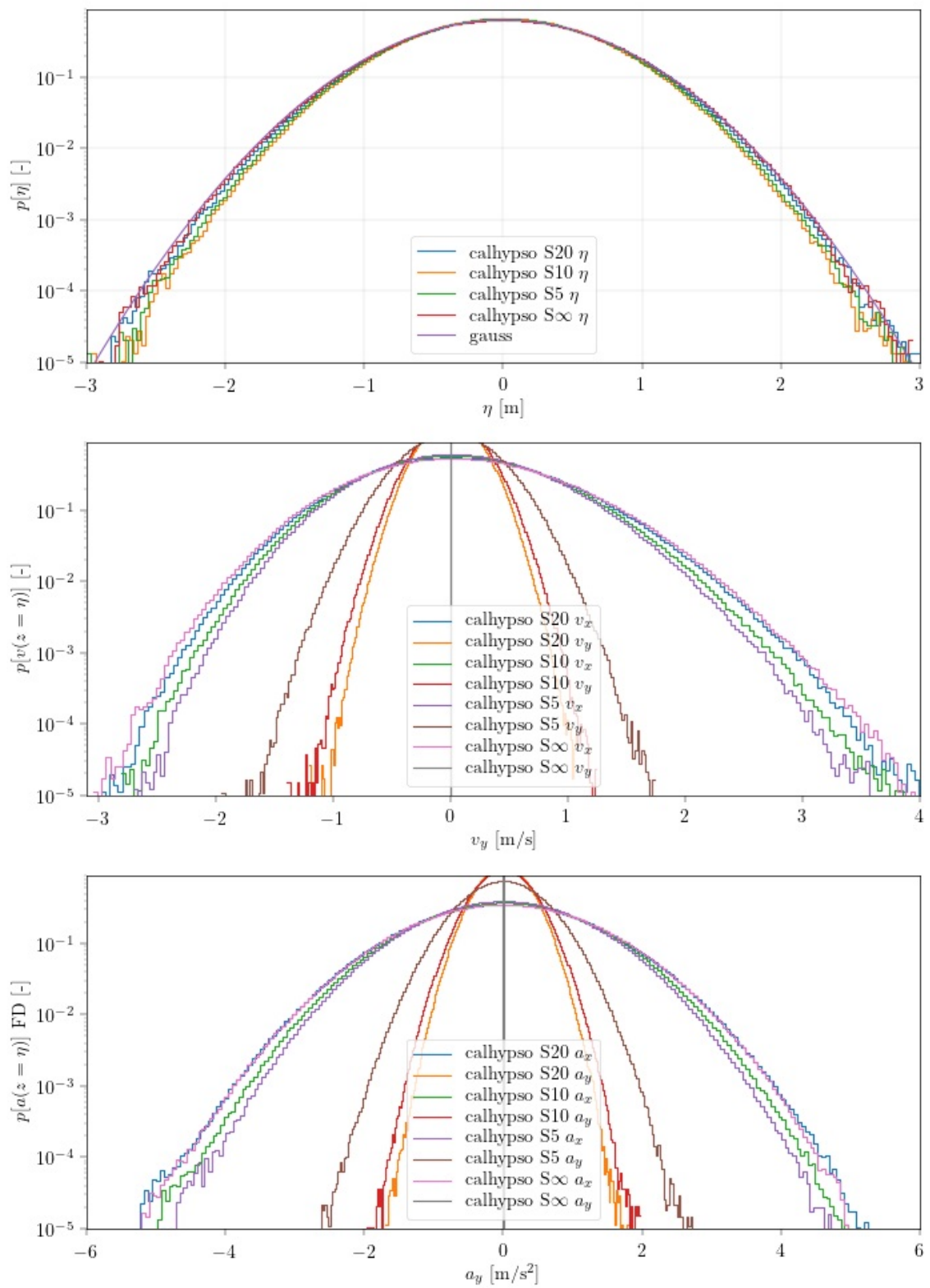


Figure 3.12: -

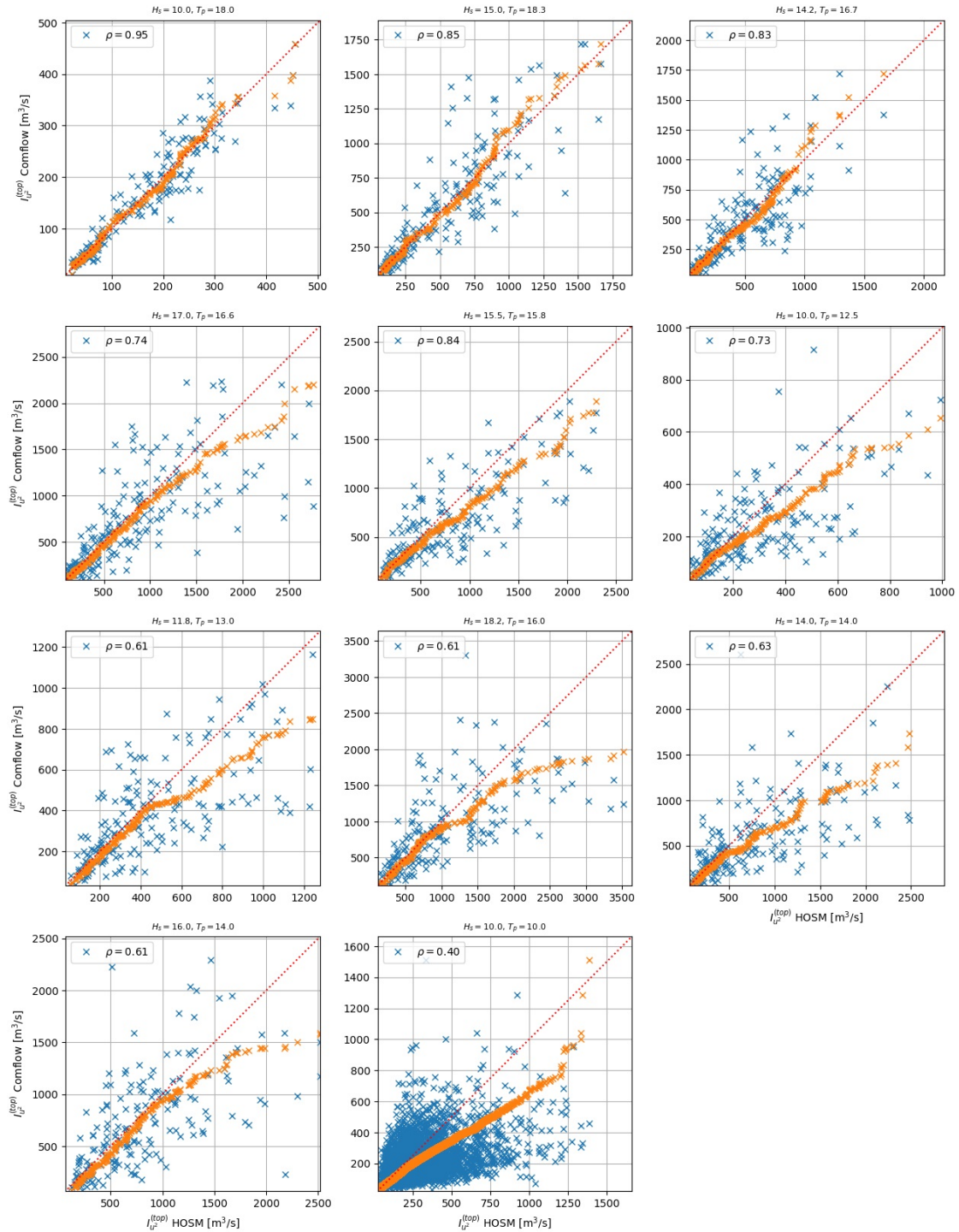


Figure 3.13: -

though an underprediction of about 10 to 15% in wave height and velocity can be expected in the crest. Giving a quantification for the acceleration is more difficult, knowing the instability at the required number of modes to accurately capture the second derivatives with the nonlinear models, but at least 15% of underprediction might be expected. Using deterministic amplitude when selecting the modes from a given spectrum is shown to have no – or at least negligible – impact on the three studied variables. Finally, depending on the directional spreading of the sea state, 5 to 15% of overestimation of the ν_x can be denoted when simplifying by concentrating all the energy along one dimension, compared to a more physical multidirectional spectrum.

The influence of the wave breaking model, both for short crested and long crested waves was quantified. It has been shown that the influence of the angular spreading was limited for most of the conditions studied in the HIPERWIND base cases, but is more significant in the case of Teesside normal sea states, with a large modification of the crest elevation statistics was denoted. In this case, the angular spreading greatly modifies the breaking behavior and therefore, the statistical distribution of crest elevation.

Afterwards, a study on the statistics of the horizontal kinematics, comparing usual engineering models (based on extensions of the linear wave theory) against a HOS model, was conducted. An underprediction of the maximal values was denoted and could be found throughout the four cases. The stretching models do not manage to recover the non-linear predictions, neither in terms of free surface elevation nor in terms of kinematics. This effect is increasing with the sea state steepness H_s/λ_p .

Other influences of different assumptions were also investigated and quantified but shown to be of lower magnitude: the selection of random amplitudes for the wave spectrum is for example shown not to significantly affect the statistics of the kinematics nor free surface elevations.

3.5 Extreme transient events

This section follows from the article by Kelly (2024), currently in press.

A method was developed to identify load-driving events based on filtered flow accelerations, regardless of the event-generating mechanism or specific temporal signature. Low-pass filtering enables calculation of acceleration statistics per characteristic turbine response time; this circumvents the classic problem of small-scale noise dominating the observed accelerations or extremes, while providing a way to deal with different turbines and controllers. Not only is the flow acceleration physically meaningful, but its use also removes the need for de-trending. Through consideration of the 99th percentile of filtered acceleration per each 10-minute period (\dot{s}_{99}) we avoid assumptions about distributions of fluctuations or turbulence, and derive statistics of load-driving \dot{s}_{99} for offshore conditions from ‘fast’ (10 and 20 Hz) measurements spanning more than 15 years. These statistics depend on low-pass filter frequency (f_c) and height.

We find long-term probability distributions of \dot{s}_{99} , which drive loads ranging from fatigue to ultimate; this also includes joint distributions with 10-minute mean (U) and standard deviation (σ_s) of wind speed. The long-term mean and mode of $P(\dot{s}_{99}|\sigma_s)$ and $P(\dot{s}_{99}|U)$ vary monotonically with σ_s and U , corroborating some IEC 61400-1 DLC prescriptions.

We find extreme \dot{s}_{99} to be independent of U , with limited connection to σ_s ; we show that 10-minute statistics cannot be translated into extreme load-driving acceleration statistics. From measurement heights of 100 m and 160 m, events of diverse character were found to arise from numerous mechanisms, ranging from non-turbulent to turbulent flow regimes, depending on f_c . Via fits to the tails of $P(\dot{s}_{99})$, curves of offshore extreme (\dot{s}_{99}) expected for return periods up to 50 years were calculated, for three characteristic turbine response times.

To drive aeroelastic simulations, Mann-model parameters were also calculated from the time-series of the most extreme events, allowing constrained simulations embedding the recorded events. To facilitate this for typical industrial measurements which lack three-dimensional anemometry, a new technique for obtaining Mann-model turbulence parameters was also created; this was employed to find the parameters corresponding to the background flow behind the identified extremes and their timeseries. Further, a method was created to use the extreme acceleration statistics in stochastic simulations for application to loads, including interpretation within the context of the IEC 61400-1 standard. Parallel work (section 4.4) has aeroelastic simulations conducted using the extreme event timeseries identified here (HiperWind D3.1, McWilliam et al., 2022), as well as Monte Carlo simulations based on the extreme statistics and new method for stochastic generation of acceleration events.

3.5.1 Summary of results, interpretation, & conclusions

From all low-pass filtered 10-minute \dot{s}_{99} found for offshore flow over a 17-year period at the coastal Høvsøre site, the largest observed flow accelerations correspond to events having durations longer than the reciprocal of filter scales chosen (f_c^{-1}). These are long enough to significantly affect wind turbine loads for turbines with characteristic controller/response times of f_c^{-1} (or shorter), if the transverse spatial scales of the flow structures are sufficiently large. Larger \dot{s}_{99} tend to correspond to shorter event durations, with larger amplitude \dot{s}_{99} associated with higher f_c ; for typical offshore turbine blade lengths ($>\sim 50$ m) and turbine response times $\sim f_c^{-1} \sim 3$ s, the shortest extremes’ effect on loads could either be mitigated (e.g. via fast controller) or induce larger blade loads (e.g., flap-wise bending moments) due to a single blade being impacted.

Identified events include some associated with the stable capping inversion above shallow ABLs including phenomena such as breaking gravity waves, wave-turbulence, entrainment outbreaks, and ‘top-down’ intrusions; we also noted extremes associated with frontal passages and flow structures not connected with the ABL-top.

Statistically, stronger filtered accelerations were found at 100 m height compared to 160 m, across all wind speeds including the extremes. Most extreme events were not turbulence, but some turbulence was seen for $f_c = 1/3$ Hz, implying the surface may have more impact for faster turbine response times. Though speeds from $\sim 6\text{--}8$ m s^{-1} are moderately common, 10-minute mean wind speeds below 8 m s^{-1} were ignored because transients further from rated speed have less impact on loads (Dimitrov *et al.*, 2018; Kelly *et al.*, 2021), and to avoid the coastal effects in unstable conditions; this is further justified by our finding that extreme accelerations for $U < \sim 11$ m s^{-1} are appreciably smaller than those with $U \gtrsim 11$ m s^{-1} (Fig. 3.14), while mean speeds between $8 \lesssim U \lesssim 11$ m s^{-1} occur more frequently than those above 11 m s^{-1} .

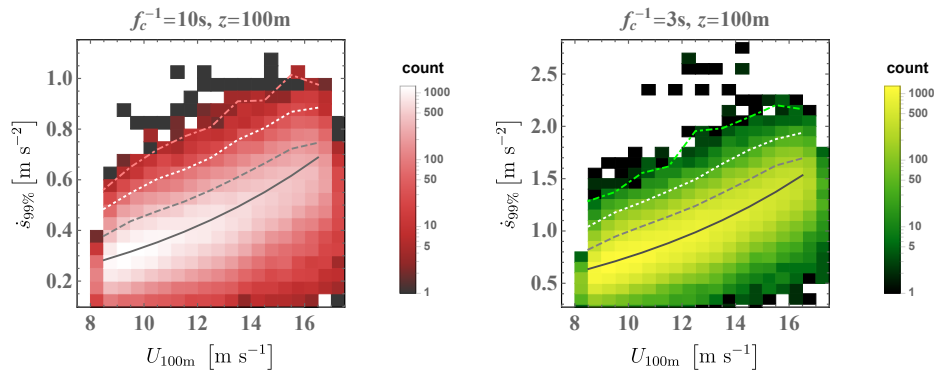


Figure 3.14: Joint distribution of 10-minute $P(\dot{s}_{99}|U)$ at 100 m height, for low-pass filter scales of 0.1 Hz (left) and 1/3 Hz (right). Solid line is exponential fit to $\text{mode}\{\dot{s}_{99}|U\}$, gray dashed is 90th percentile, white dotted is 99th percentile, and color dash-dotted is 99.9th percentile of $P(\dot{s}_{99}|U)$.

If we included lower speeds and a dependence of extreme \dot{s}_{99} decreasing at smaller U , then use of the marginal extreme distribution and associated statistical extrapolation (Fig. 3.15) would give lower predictions of extreme acceleration at mean wind speeds below ~ 11 m s^{-1} .

No U -dependence was found for extremes approaching the high end of speeds analyzed (18 m s^{-1} , again from Figure 3.14), where less impact is expected from the transient accelerations due to being above rated speed; although shut-down cases could be considered for comparison with the IEC 61400-1, much more data would be needed to investigate these due to the relative rarity of speeds crossing above cut-out (around 25 m s^{-1}).

We have assumed that the (westerly) conditions analyzed are representative for all directions offshore, but one could conceive that the significant south-easterly winds which sometimes occur in the spring at Høvsøre (Peña *et al.*, 2016) could be different enough to have a small impact on the statistics; however, such wind directions are even less common offshore in the North Sea and North Atlantic wind climates characterized by the measurements (e.g., Hahmann *et al.*, 2022). We can further get a sense of the limited potential impact on 50-year extreme accelerations, considering the ‘error’ lines in Figure 3.15, which represent neglect of the fraction of speeds not considered, and fraction of winds coming from offshore, respectively.

This work has produced statistics for dominant flow accelerations detected using three different

low-pass filter frequencies f_c (as proxies for characteristic turbine response times), but yet more utility could be obtained by characterizing the systematic effect of low-pass filtering on extreme acceleration statistics; i.e., to find an explicit dependence of the extreme \dot{s}_{99} distribution on f_c . Attempts were made to this end, but not included because no simple relation was found to fit the data. This is not surprising: the filtered extreme events are not inertial-range turbulence or any single phenomenon, though more extreme turbulence is observed at 100 m than 160 m. The relative rates of occurrence and relative variation in the strength of the phenomena causing extreme load-driving accelerations is seen to depend not only on f_c , but also on distance to both the ground and to the capping inversion, as well as the capping inversion strength (Pedersen et al., 2014; Kelly et al., 2019).

For use in Monte-Carlo aeroelastic simulations, a method was developed (Kelly, 2024) to employ the extreme distributions of offshore filtered acceleration derived above. Practical stochastic expressions are given to relate the magnitude and duration (gust rise time) of filtered flow acceleration including rise time distributions, applicable within the emerging IEC 61400-9 or as a probabilistic supplement (replacement) for the EOG prescription found in the IEC 61400-1; we note these practical expressions followed from earlier wind speed ramp acceleration studies, and the exact constants and forms may be improved with further investigation and analysis. Additionally considering the IEC 61400-1, its EOG prescription has an implicit rise time of almost 3 s, and for contemporary wind turbines in the highest turbulence subclass (A+), around rated speed it implies characteristic event acceleration magnitudes that are similar to the 50-year values obtained from measurements at 100–160 m heights with $f_c = 1/3$ Hz. For higher V_{hub} the IEC EOG prescription gives larger accelerations than 50-year \dot{s}_{99} found here from 100–160 m observations with $f_c = 1/3$ Hz (even for different turbulence subclasses), and \dot{s}_{EOG} are generally larger than 50-year \dot{s}_{99} from measurements with $f_c = 0.1$ Hz or $1/30$ Hz; the lowest turbulence subclass ($I_u = 12\%$) gives weaker accelerations than 50-year $\dot{s}_{99}|_{f_c=1/3\text{Hz}}$ for speeds below rated (Kelly, 2024). We note that the IEC 61400-1 standard — due to its original basis onshore and with z_{hub} closer to the surface — prescribes its EOG in terms of turbulence intensity, which is not realistic for offshore turbines with typical hub heights beyond 100 m; as we have seen, load-driving flow accelerations do not follow 10-minute standard deviations of wind speed or velocity.

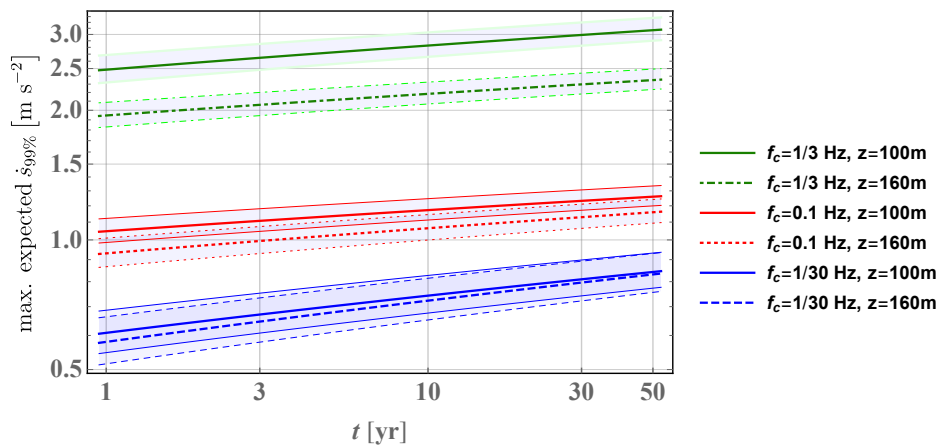


Figure 3.15: Expected \dot{s}_{99} per return period t , for the three different filter scales considered and two heights analyzed. Thick lines correspond to $T_{base} \simeq 39$ minutes; thin lines bounding shaded area for each correspond T_{base} spanning 10–119 minutes, to indicate uncertainty.

From the acceleration statistics found here, an offshore probabilistic gust prescription towards an IEC 61400-9 standard was also derived (Kelly, 2024). More explicit systematic quantification of the durations associated with extreme flow accelerations, with rise time statistics conditioned on wind speed and amplitude (like that for ramps by Kelly et al., 2021), is ongoing beyond HiperWind; this includes relationships between \dot{s}_{99} and gust duration. Following ramp studies and preliminary analysis here we have taken extreme events to have $t_d \propto 1/\dot{s}_{99}$ in a statistical sense with $\Delta s \propto \dot{s}_{99} t_d$. More investigation is needed to explicitly determine the joint behavior of extreme \dot{s}_{99} and the associated $\{t_d, \Delta s\}$.

We found here that extreme acceleration events have $\dot{s}_{99} \simeq \dot{u}_{99}$ independent of σ_s and speed, while for the most commonly-occurring conditions $\dot{s}_{99} \propto \sigma_s$, as seen in Fig. 3.16. The behavior of commonly-occurring \dot{s}_{99} may not be markedly different than that of σ_u in terms of its effect on fatigue loads, which is what Figure 3.16 may imply; although this remains to be shown directly from observations, we expect \dot{s}_{99} to be more important for extremes.

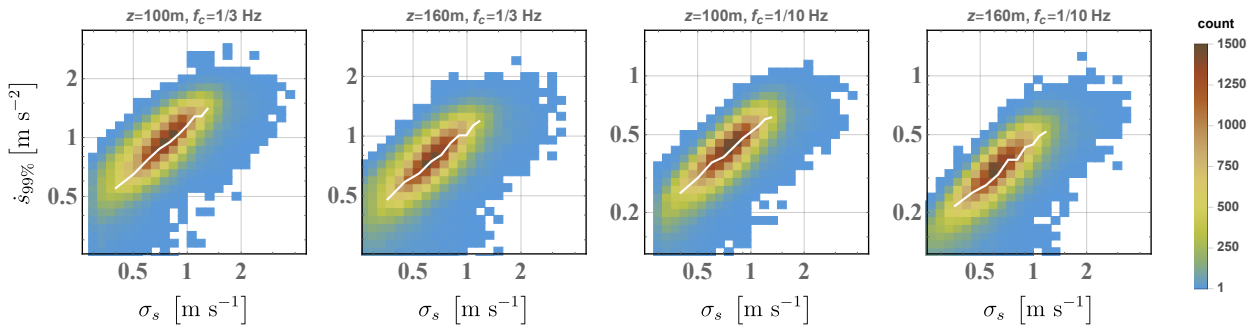


Figure 3.16: Joint PDFs $P(\dot{s}_{99}, \sigma_s)$ of all 10-minute $\{\dot{s}_{99}, \sigma_s\}$ at both heights analyzed, for low-pass $f_c = \{1/10, 1/3\}$ Hz. White lines show $\text{mode}\{\dot{s}_{99}|\sigma_s\}$.

It is possible that more representative filters (e.g., band-pass) can be made to find acceleration statistics based on common control strategies near rated power; parameters such as pitch angle might also be considered. The analysis presented here also needs to be expanded to include speeds across the *full* range of wind turbine operation (beyond 8–18 m s^{-1}), to heights above 160 m, and at multiple sites. Lastly, a mean speed dependence has not yet been found or incorporated into the extreme flow acceleration statistics, but with more measurements this could be done.

3.6 Joint distributions of environmental conditions

A probabilistic description of the environmental conditions is important for the design of offshore wind turbines, and this is typically obtained by way of joint distribution models. In HIPERWIND, joint distribution models for selected wind and wave variables were established for two particular locations, i.e. South of Brittany and Teeside. The environmental variables considered were

- Wind direction (θ)
- mean wind speed (U)
- Turbulence (σ_S)
- Significant wave height (H_S)
- Wave direction (α)
- Peak wave period (T_P).

The fitted model for one of the locations is presented in [Kelly and Vanem \(2022\)](#) and the model for the other location is presented in [Vanem et al. \(2023a\)](#), with an extended discussion on uncertainties associated with it in [Vanem et al. \(2024a\)](#). Note that omnidirectional models were fitted to data from both locations, and additional models for specific wind directions were established for one of the locations. A brief summary of these models will be given in the following.

In both cases, a hierarchical conditional model on the form of the product of a marginal model and several conditional models was fitted to data:

$$f_{U,\sigma_U,H_S,T_P,\beta}(u, \sigma, h, t, \beta) = f_U(u)f_{\sigma_U|U}(\sigma|u)f_{H_S|U}(h|u)f_{T_P|H_S}(t|h)f_{\beta|U}(\beta|u). \quad (3.1)$$

This is a simplified model that includes several assumptions on conditional independence. Different models are explored for the different marginal and conditional models and the following distribution families were selected:

- A hybrid model consisting of a Weibull distribution for the body and a Generalized Pareto distribution for the tail for the marginal distribution of wind speed.
- A log-normal model for the conditional distribution of turbulence, given wind speed, with a power-law relationship between the model parameters and wind speed.
- A 3-parameter Weibull distribution for significant wave height given wind speed. For one of the locations, with limited water depth, a truncated version of the Weibull distribution was assumed ([Vanem and Fazeres-Ferradosa, 2022](#)). Different parametric functions were explored to model the dependence to wind speed.
- A log-normal model for the conditional distribution of spectral peak period given significant wave height, with power-law and exponential relationships between location and scale parameters, respectively, to significant wave height.
- A two-component mixture of von Mises distributions for the directional variables. Note that for one of the locations, only the wind-wave misalignment was modeled, whereas for the other both wind and wave directions were modeled directly.

For further details on the selected models, including estimated model parameters, see [Kelly and Vanem \(2022\)](#); [Vanem et al. \(2024a\)](#).

The established parametric distribution models were used further in structural reliability assessment and design of the offshore wind turbines in subsequent work packages of HIPERWIND,

see e.g. [Wang et al. \(2024\)](#).

In addition to the parametric joint distribution presented above, the usefulness of non-parametric approaches to joint modeling was also explored, as presented in [Vanem et al. \(2024b\)](#). In particular, the non-parametric Bernstein copula was introduced to model multivariate dependencies. Results from these investigations suggest that non-parametric work well in fitting arbitrary dependence structures in the data, but that care should be taken if the interest is in the extremes. Non-parametric models in general may not generalize and extrapolate well.

4 Probabilistic load assessment (WP3 outcomes)

4.1 Challenges addressed in WP3

Despite the growing interest to introduce explicit uncertainty propagation in the prediction of loads on offshore wind turbine components, the current workflow used by design engineers still remains largely deterministic. One reason for this is due to the complex modeling workflow with both multiphysics : aerodynamics and hydrodynamics, and multiscales : wake analysis at the wind farm scale and dynamics at the turbine scale. On top of it, such simulations are facing a limit in computational cost feasibility, because of the need to sample the joint probability of wind and wave occurrences during the service life, and of the time needed to simulate one stationary phase of aero-servo-hydro-elastic dynamic response of the structure. Because of such constraints, the engineers need to use well known approaches with simplifying assumptions, like the Blade Element Momentum approach for aerodynamics, or the Morison formula for the hydrodynamics around thin solid elements.

In this WP, we studied different ways to make progress in this situation. First, we suggest different approaches to reduce the computational cost:

- with surrogate models based on a parameterization of the wake deficit shapes or directly of the wind farm layout, dedicated for quasi-static or dynamic wake simulations,
- with a clustering analysis of the wind deficit and turbulence conditions over the different turbines in a wind farm, in order to reduce the number of unique (and costly) reliability analyses of individual turbines.

Then, we provide quantification on the approximation of simplified engineering modeling of aerodynamics and hydrodynamics, when compared to high fidelity modeling. This information is computed in the wind and wave parameter space by means of interpolating Gaussian processes which are iteratively built to reduce the uncertainty on the difference.

4.2 Wind farm wake and layout parameterization

Estimating the loads and power output of individual wind turbines within a wind farm is an important part of almost any wind farm design and optimization study. Engineering wake models such as those implemented in the PyWake tool ([Pedersen et al., 2023](#)) can provide an efficient estimation of the power output. However, load estimations will typically require aeroelastic load simulations, which are significantly more expensive. A popular way of reducing the computational expenses is by mapping the advanced (aeroelastic) model behavior to a simpler function (typically a regression model) called a surrogate model. For wind farm related surrogates, the influence of neighboring turbines needs to be encoded in terms of a fixed set of quantities that serve as surrogate model inputs. We refer to this process as wind farm layout parameterization. A specific challenge is that the layout will vary from wind farm to wind farm, which makes it difficult to generalize the parameterization so that the surrogate models can be used on arbitrary wind farms. The Hiperwind project developed two procedures for wind farm wake effect parameterization and subsequent surrogate model training as part of Deliverable 3.1 ([McWilliam et al., 2022](#)). The two approaches are outlined in the following sections.

4.2.1 Wind farm wake effect parameterization using surrogates for local wind estimates

This first approach is derived for the most frequent case of quasi-static engineering wake models. Such models are computing the time-averaged wind speed deficit and added turbulence within the wind farm for a given duration, generally 10 min, for which the turbulent wind process is assumed stationary. The model chain is represented on Figure 4.1. When considering the computational cost distribution among the different steps of this model chain, the part composed of the turbulence box generation plus the aero-servo-hydro-elastic simulator which are surrounded by a red rectangle in this figure are clearly dominating the quasi-static wake model. In this study, the wake simulator used is from FarmShadowTM library of IFPEN, with a super Gaussian deficit Blondel and Cathelain (2020), the Qian-Ishihara wake-added turbulence model Blondel and Cathelain (2018) and a linear superposition in case of wake interactions.

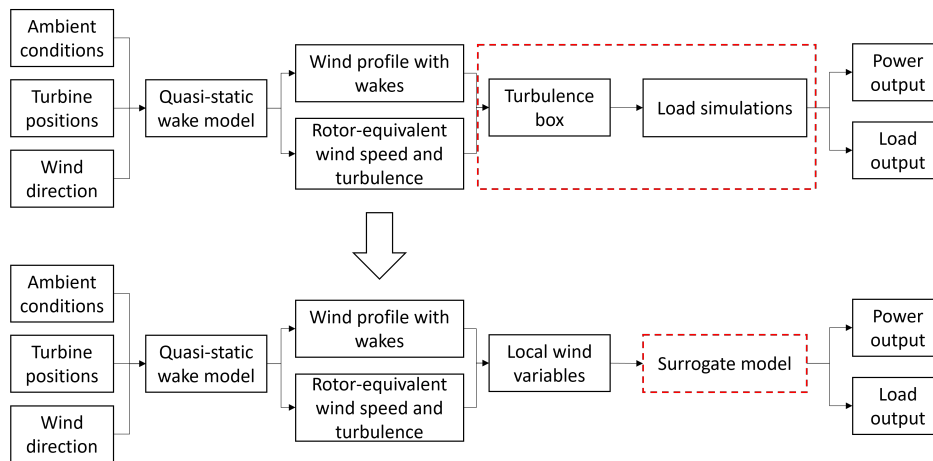


Figure 4.1: Sketch of a wind farm wake effect parameterization workflow using surrogates for local wind estimates. Diagram reproduced from McWilliam et al. (2022).

Based on this consideration, this first strategy aims at reducing the computational cost predicting the power and load on the different wind turbines of a farm, by replacing this costly part by a surrogate model. To do so, it is required to compress the information given by the quasi-static simulator in a reduced list of parameters which will drive the dimension of the surrogate. Indeed, when defining a surrogate, one needs to make a Design of Experiments (series of simulations) to train it, and it is well known that the computational cost increases a lot with the number of dimensions to maintain a good model performance.

A starting point of important parameters given by the quasi-static wake simulator for a given turbine is the time-averaged wind speed and its corresponding standard deviation measuring the turbulence, both averaged on the rotor surface (alternatively, one may choose to keep the value at the hub only). To enrich the information while limiting the surrogate dimension, we choose to add parameters representing only the deficit anisotropy on the vertical plane crossing the rotor. We used in this study the TurbSim generator of NREL that is based on the Kaimal wind spectrum. At any given point of the turbulence box, the wind speed can be decomposed into a mean value and a zero-mean stochastic process. Our idea was to replace the mean part by the wake deficit computed by the wake simulator and reconstruct a wake-modified turbulence box. This modification is represented for a vertical plane in Figure 4.2, with the turbulence part on

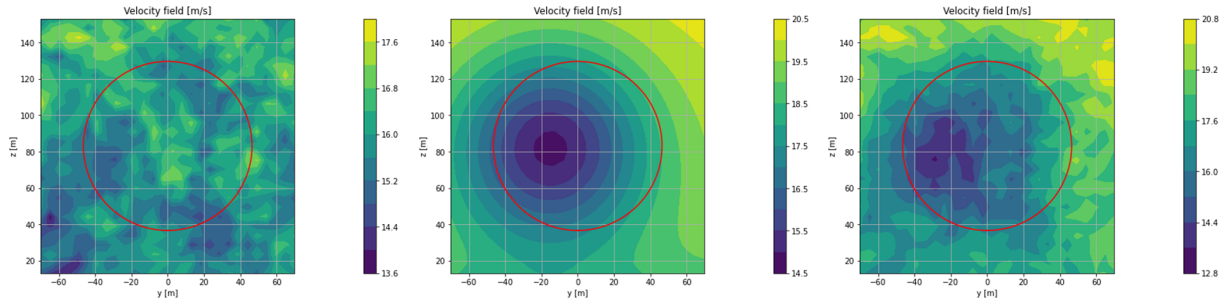


Figure 4.2: Illustration of turbulence field being modified by a single wake. Plots reproduced from [McWilliam et al. \(2022\)](#).

the left, a wake deficit on the middle and the final result on the right.

The parameterization then consists to select parameters representing the wake deficits seen on a vertical plane at the rotor location, from the result of FarmShadowTM simulator. We choose a test function from Porté-Agel Gaussian wake model [Bastankhah and Porté-Agel \(2014\)](#) which is composed of the ambient term including a power-law vertical shear with 2 parameters, and a term for each wake deficit seen by the considered rotor with 3 parameters for width, height and intensity of the deficit.

For each given FarmShadowTM simulation and each vertical planes at rotors (Figure 4.2), a least square fitting is performed to associate a parameterized deficit with variable number of superimposed deficits. For Teesside wind farm a maximum of 2 deficits is found suitable for the cross-wind direction, as illustrated in Figure 4.3.

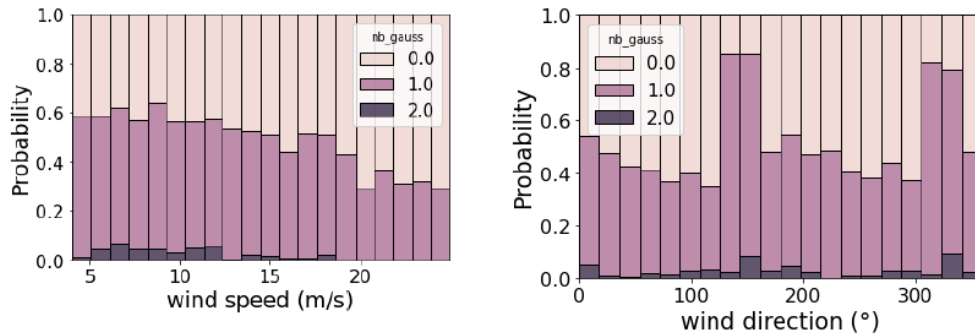


Figure 4.3: Proportion of number of wakes required to fit the vertical plane deficits for Teesside wind farm. Plot reproduced from [McWilliam et al. \(2022\)](#).

It is then possible to replace aero-servo-hydro-elastics simulations performed with DeeplinesWindTM by a Kriging surrogate to relate the local deficit parameters to a given load on the wind turbine structure. The result is illustrated in Figure 4.4 with a good reproduction of the flapwise DEL predictions for a turbine at the centre of the wind farm.

4.2.2 Wind farm wake effect parameterization using layout encoding

A number of previous studies use wind farm layout parameterizations to characterize wake interactions: [Yan et al. \(2019\)](#); [Dimitrov \(2019\)](#); [Dimitrov and Natarajan \(2021\)](#); [Sun et al. \(2020\)](#);

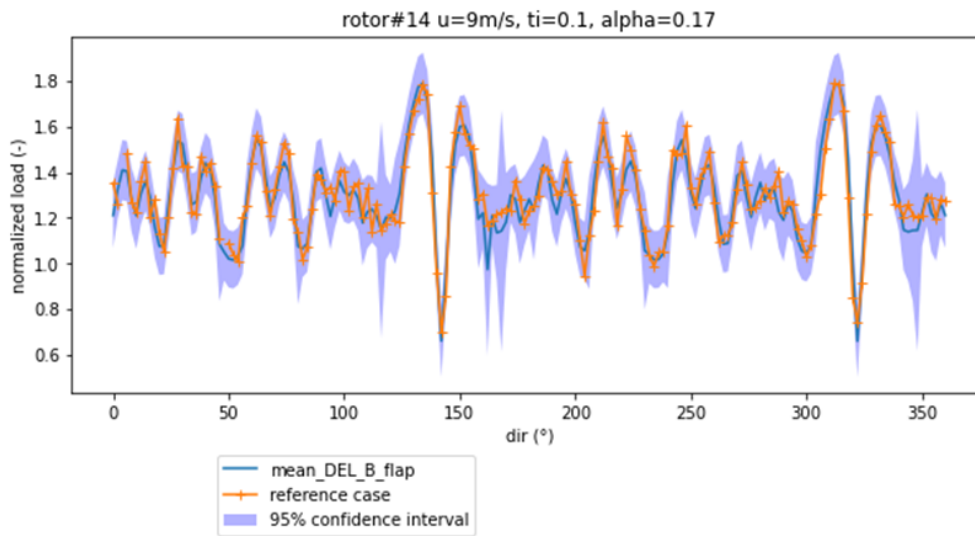


Figure 4.4: Comparison of blade flapwise DEL predictions with the surrogate model vs. reference simulations. Plot reproduced from [McWilliam et al. \(2022\)](#).

[Bleeg \(2020\)](#). Most of these approaches have challenges with generalizing the model to arbitrary wind farms, either because the parameterization is based on just a few variables which are not sufficient to describe all possible layouts ([Yan et al., 2019](#); [Dimitrov, 2019](#)), or because the number of variables grows proportionally to the number of turbines in the farm ([Dimitrov and Natarajan, 2021](#)). With the present study, we seek to alleviate this issue by introducing an additional autoencoder model which translates layout-derived features into a few latent variables. With this approach, it is feasible to encode the layout of an arbitrary wind farm by two features per each turbine, which are then reduced by the autoencoder to a small number of latent variables (3-6) that are suitable as inputs for load and power surrogate model training. The entire modelling setup (Figure 4.6) includes environmental conditions and wind farm layout features as inputs, and predicts individual wind turbine response (loads and power). The autoencoder part is trained on PyWake simulations of a large number of wind farms with arbitrary layouts, while the load prediction surrogate is trained using aeroelastic simulations with Hawc2 where dynamic wake effects are introduced with the dynamic wake meandering (DWM) model ([Larsen et al., 2008](#)). Further details on the autoencoder training part are available in [Dou and Dimitrov \(2022\)](#).

Virtual load monitoring using wind farm load surrogates

The load prediction surrogate described above was integrated in a procedure for recovering accumulated fatigue load history by feeding operational SCADA data. In the absence of actual load measurements in most existing wind farms, this approach provides a model-based approximation of the fatigue accumulation. The SCADA data are used to determine the actual site-specific environmental conditions as well as the operating patterns of the turbines (e.g., normal operation periods, number of startups/shutdowns, curtailment, idling) ([Dimitrov and Natarajan, 2019](#)). For the periods of time under normal operation, the wind direction and the farm layout are fed as inputs to the autoencoder model, which outputs a set of latent variables per turbine that describe wake interaction. These variables, together with the ambient wind speed, are fed to a load prediction model which estimates the accumulated DEL (Damage-Equivalent Loads) per turbine in the wind farm. Further, DEL increments for the periods with transient events (startups

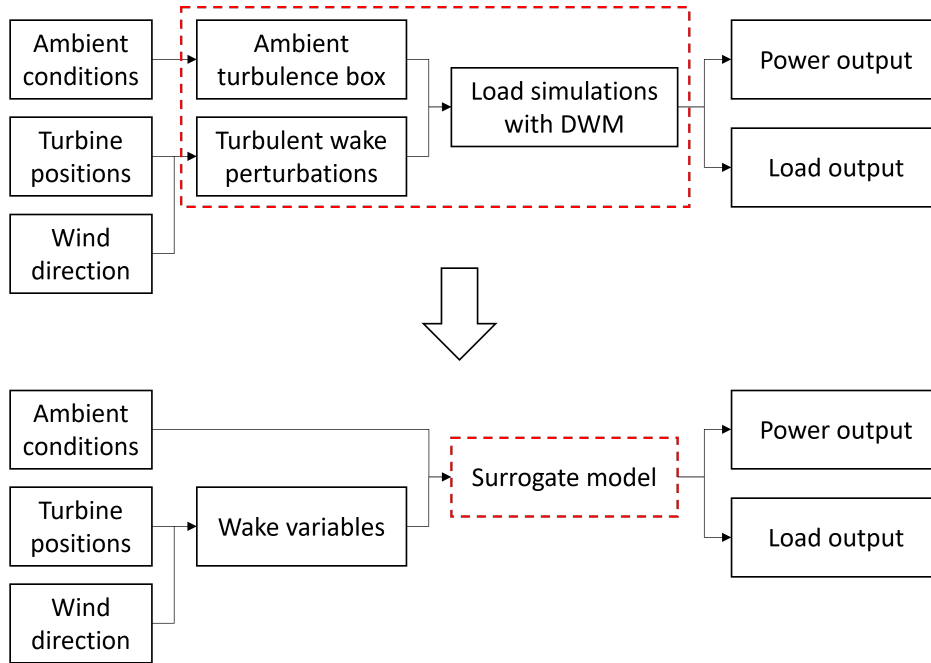


Figure 4.5: Sketch of a wind farm wake effect parameterization workflow using layout encoding. Diagram reproduced from [McWilliam et al. \(2022\)](#).

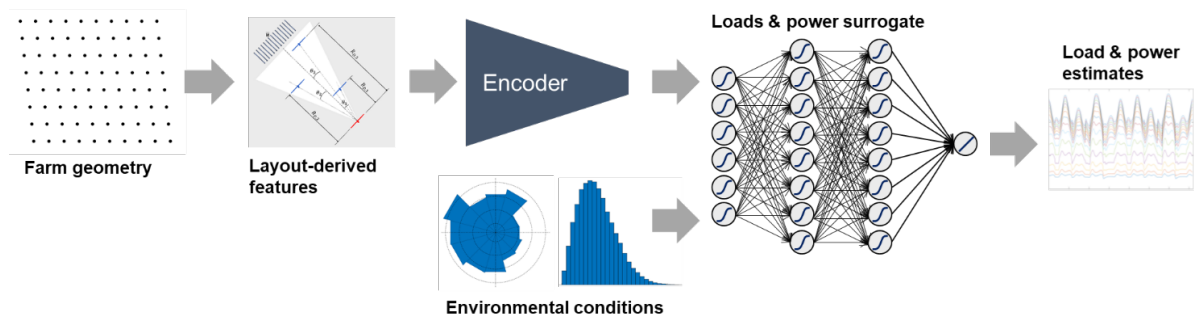


Figure 4.6: Sketch of load modelling workflow using wind farm layout encoding as surrogate model inputs. Diagram reproduced from [McWilliam et al. \(2022\)](#).

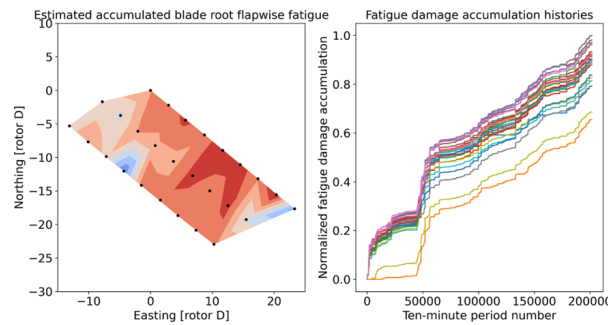


Figure 4.7: Normalized blade damage-equivalent load accumulation history for turbines at Teesside. Figure reproduced from [McWilliam et al. \(2022\)](#).

and shutdowns) are estimated by table look-ups as it is expected the wake effects do not play a significant role in these cases and a simpler estimation is sufficient. These steps result in a model-based estimate of the fatigue load history in the farm, as illustrated in Figure 4.7 for the Teesside wind farm.

4.2.3 Turbine clustering

Reliability-based design of an offshore wind turbine requires a huge number of calls to the aero-servo-hydro-elastic simulator because of the very small annual failure probability of $1E-04$ to $1E-05$ that is targeted after international design standards [IEC \(2019a\)](#), depending on the component redundancy. When considering the large computational cost of such simulations, design engineers are facing challenges to get such information in a pragmatic and time-efficient way consistent with industrial project constraints. To reduce this difficulty in a pragmatic way, we investigated a clustering method which groups the turbulent wind conditions seen by the different wind farm turbines in few groups seeing similar conditions.

The starting step consists in propagating the uncertainty from ambient wind conditions to wake-modified ones, using engineering wake simulations. We used here the quasi-static wake model already introduced in section 4.2.1 and to reduce the dimension while keeping the most important information for loading, we considered only 2 scalars representing the mean speed and its associated variance. Initially, the idea was to take into account the wake model uncertainty, estimated from the difference between several engineering models and from their difference with higher fidelity models. However, this option was dismissed because some differences, specifically in case of strong wake interactions, need further investigation to be fully clarified and validated. Given the short computational time of quasi-static wake analysis, a simple Monte-Carlo procedure was applied and provided the joint distribution of the 2 scalars, as illustrated in Figure 4.8. As expected with wakes, the mean speed margin probability is shifted to the left from the ambient curve, indicating the deficit, while the turbulence intensity marginal probability is shifted to the right from the ambient curve, indicating the added turbulence.

To perform clustering on probabilistic distributions, it is first required to choose a metric measuring the distance between two distributions. We chose here the Maximum Mean Discrepancy (MMD) defined in [Sriperumbudur et al. \(2010\)](#). Several clustering methods were compared and it was found that only few groups were necessary to represent the turbulent wind conditions over the whole wind farm of South Brittany which is composed of a 5x5 layout, Figure 4.9.

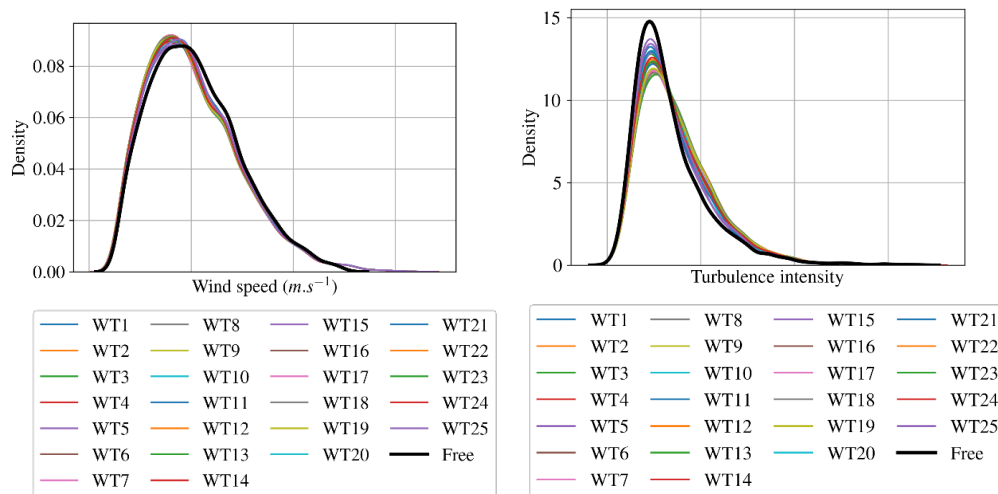


Figure 4.8: Marginal distribution for mean speed (left) and turbulence intensity (right) on floating turbines of a theoretical wind farm in South Brittany, France. Figure reproduced from [Ardillon et al. \(2022\)](#).

N α	Ward α		Complete α		k-medoids α		Spectral α	
	U α	TI α	U α	TI α	U α	TI α	U α	TI α
2 α	1.53 α	1.01 α	1.53 α	1.01 α	1.43 α	0.96 α	1.50 α	1.08 α
3 α	1.31 α	0.88 α	1.31 α	0.88 α	1.15 α	0.78 α	1.21 α	0.89 α
4 α	0.95 α	0.62 α	0.95 α	0.62 α	0.89 α	0.56 α	0.92 α	0.60 α
5 α	0.84 α	0.53 α	0.84 α	0.54 α	0.70 α	0.43 α	0.84 α	0.54 α
6 α	0.73 α	0.46 α	0.76 α	0.50 α	0.6 α	0.32 α	0.88 α	0.62 α
7 α	0.83 α	0.37 α	0.64 α	0.41 α	0.52 α	0.27 α	0.71 α	0.47 α
8 α	0.57 α	0.35 α	0.57 α	0.35 α	0.46 α	0.23 α	0.80 α	0.56 α

Figure 4.9: Mean absolute MMD errors (in percent) in wind speed and turbulence intensity over the full domain for every clustering solution for the South Brittany wind farm. Figure reproduced from [Ardillon et al. \(2022\)](#).

Let us underline that this clustering is only valid for Fatigue Limit States, as it is based on the MMD between full probabilistic distributions. For Ultimate Limit State, designers are looking for the worst case over the wind farm.

4.3 Wake model uncertainty

Wake phenomenon is a critical part in the design of offshore wind farms as it strongly decreases the production. Several models have been developed to simulate this process. High fidelity models of the turbulent wind flow dynamics like the Large Eddy Simulations (LES) are too long for being used in engineering context, e.g. in the layout optimization at the early stages of a wind farm design. For this reason, several models, hereafter called "engineering wake models", have been developed and used with simplifying assumption in stationary conditions. They are based on assumption of the wake geometries in transverse and downstream directions, and mass plus momentum balance principles, see e.g. [Blondel and Cathelain \(2020\)](#) for more details on such models.

The first objective of the study on wake model uncertainty was to analyze the approximation introduced by engineering stationary wake models in specific conditions, for which their empirical assumptions may be questioned: strong wake interactions in the case of small inter-turbine distance that is occurring in crosswind direction, atmospheric boundary layer state deviating from the neutral condition for which empirical fitting of the models have been validated. Indeed, the atmospheric stability has a well known influence on the wake with with an increase of recovery length when the stability increases. To achieve this goal, several LES simulations were performed with PALM [Maronga et al. \(2020\)](#); [Steinfeld et al. \(2015\)](#) and Meso-NH [Joulin et al. \(2020\)](#); [Jézéquel et al. \(2021\)](#) software in wich the turbines are modeled by means of Actuator Disc for PALM and Actuator Lines for Meso-NH. As the possibility to have different stability conditions than neutral for the atmosphere is correlated with lower wind speeds, the scenarii are run for below-rated wind speeds. Also, to investigate the wake interaction influence, both mainwind and crosswind directions have been studied. The case of neutral, Figure 4.10 and stable, Figure 4.11 were successfully simulated with these LES tools, however the unstable simulations are not exploitable as the convection cell size should have required a much larger domain.

As a result, wake profile at difference distance downstream of a rotor have been compared to that of a stationary engineering wake model from FarmShadowTM IFPEN library. In neutral conditions, the difference remains small, confirming the validation of engineering fitting for these conditions, Figure 4.12. However a larger discrepancy is observed for stable conditions with an overprediction of the wake deficit and turbulence for the engineering model, Figure 4.13 and for strong wake interactions for crosswind directions, indicating a need of future investigations in the engineering model assumptions for these specific wind and farm conditions.

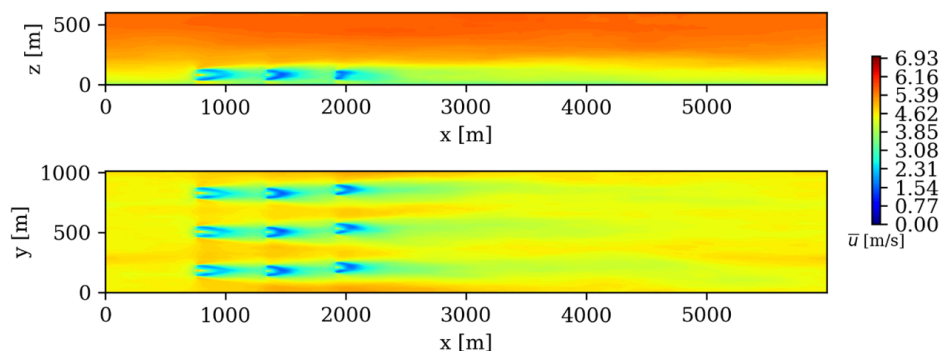


Figure 4.10: Figure reproduced from [Ardillon et al. \(2022\)](#).

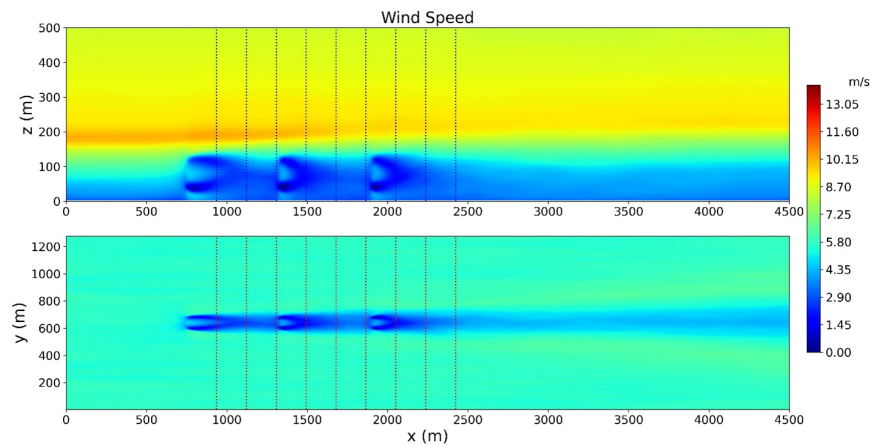


Figure 4.11: Figure reproduced from [Ardillon et al. \(2022\)](#).

The second objective was to provide a quantitative estimate of the engineering model approximation by comparing it to a less time consuming but still more physical wake model with the DWM-HAWC2 implementation of DTU of the Dynamic Wake Meandering phenomenon [Reinwardt et al. \(2021\)](#). A substantial DoE with 5460 simulations for the two models was computed in the 3D wind parameter space (mean speed, turbulence and direction), Figure 4.14. The larger differences are also observed for the case of strong wake interactions in crosswind direction, for which the inter-turbine distance is the smallest. The difference is interpolated in the full parametric space by means of GP fitting which are represented according to the wind direction in Figure 4.15. Again, the large differences are seen at crosswind at 308° . For most of the other scenarios, the difference in normalized deficit is less than 2% while FarmShadowTM often overpredicts the turbulence when compared to DWM-HAWC2. Based on this study results, future investigations should be devoted to the validation of both models in case of strong wake interactions, to check the assumptions derived from previous site data [Larsen et al. \(2015\)](#).

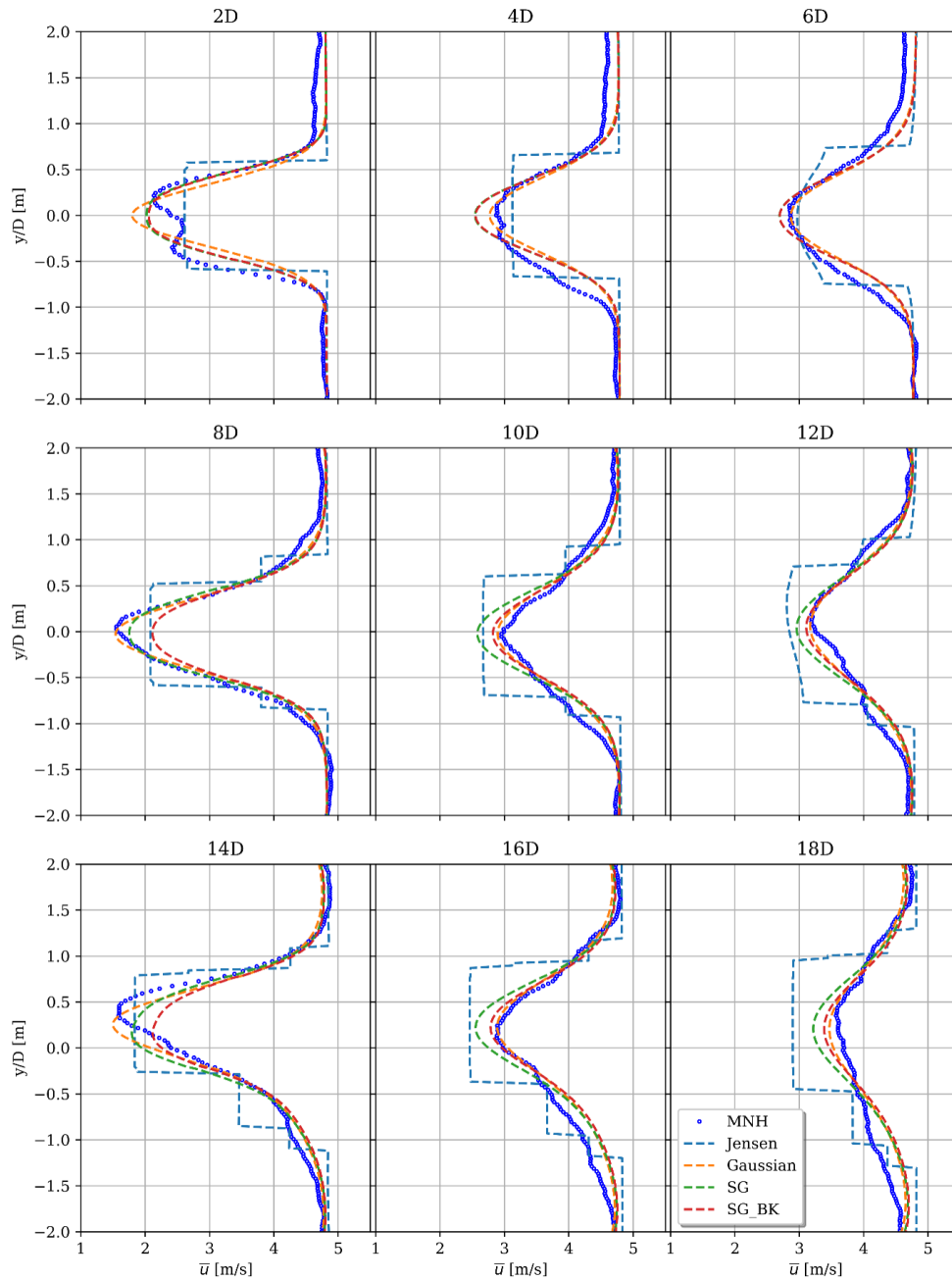


Figure 4.12: Neutral atmosphere: vertical and horizontal cuts of mean wind speed at the middle row position and at hub height, respectively. Figure reproduced from [Ardillon et al. \(2022\)](#).

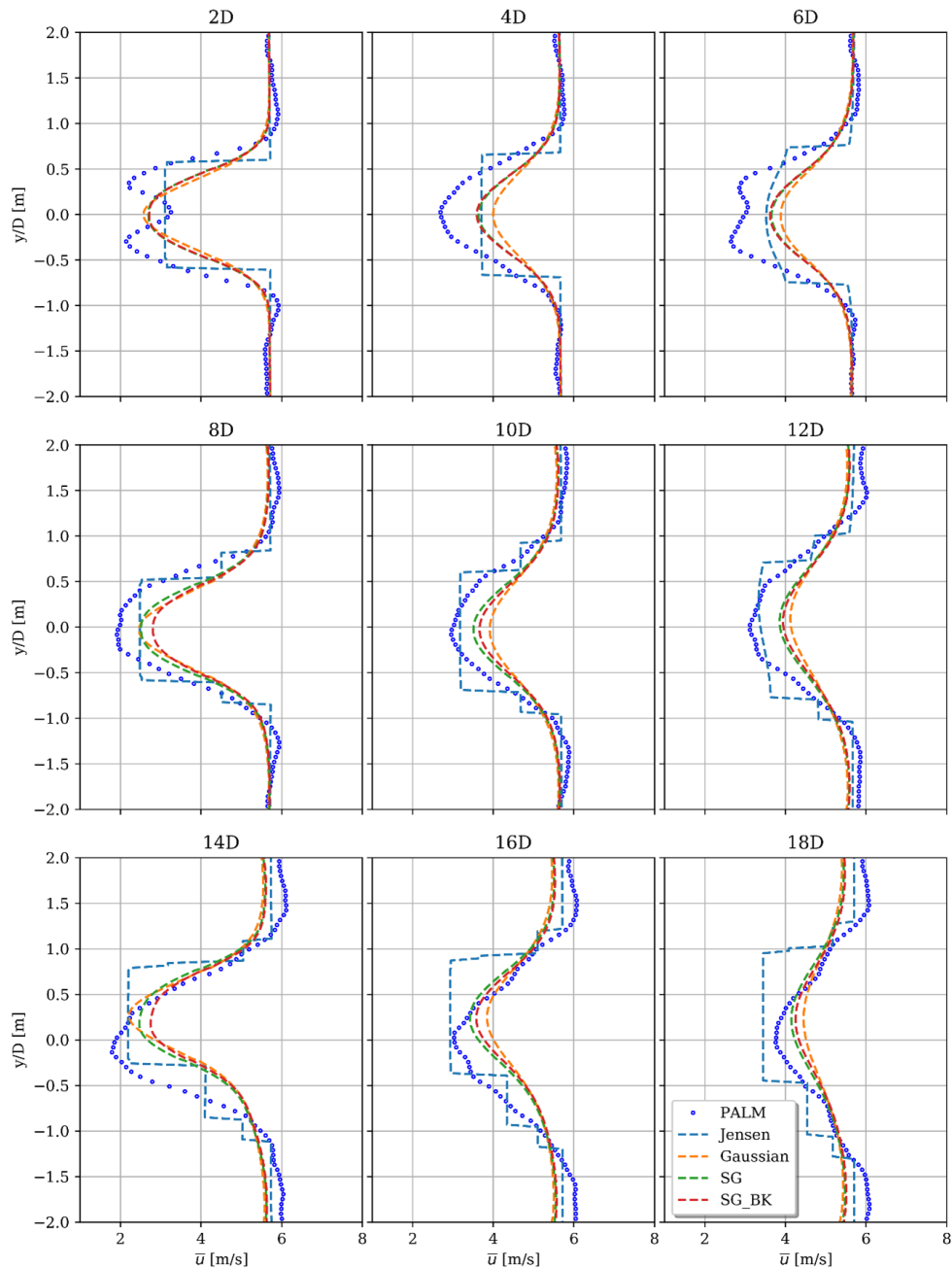


Figure 4.13: Stable atmosphere: vertical (up) and horizontal (down) cuts of mean wind speed at the middle row position and hub height, respectively. The vertical lines show selected positions to extract vertical and horizontal profiles downstream of the first turbine. Figure reproduced from [Ardillon et al. \(2022\)](#).

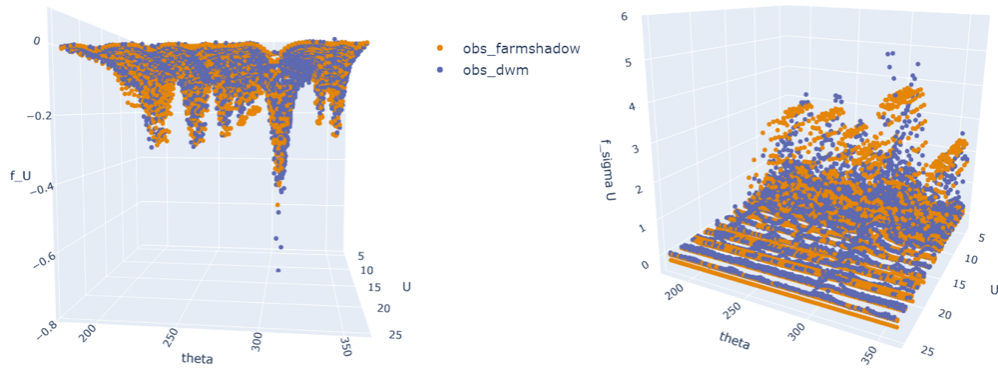


Figure 4.14: Teesside: FarmShadowTM and DWM-HAWC2 model results: normalized mean speed difference on the left, and normalized turbulence difference on the right. Figure reproduced from [Ardillon et al. \(2022\)](#).

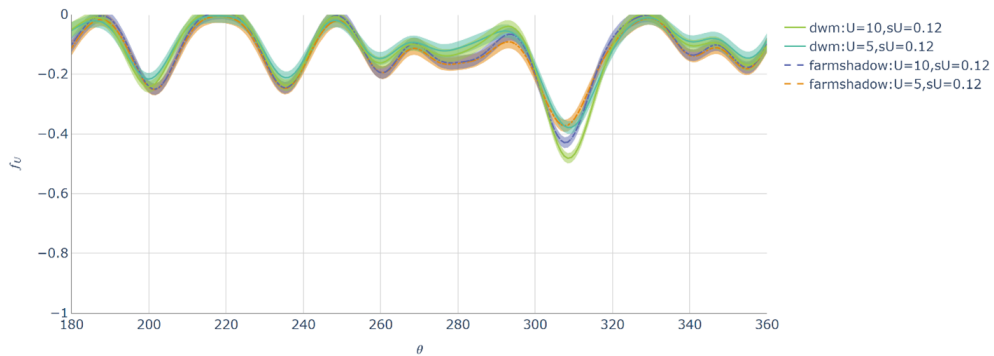


Figure 4.15: Figure reproduced from [Ardillon et al. \(2022\)](#).

4.4 Simulation of special turbulence cases

Simulation of wind turbine response under extreme transient events (extreme gusts, direction changes, wind shear) is a key part of the IEC61400-1 load design basis. The simulations under such events, especially when combined with mechanical or electrical faults, can often become design drivers. The extreme transient events in IEC61400-1 are defined in terms of synthetic functions (such as e.g. gusts following a bell-shaped curve), and the event magnitudes are a deterministic function of the wind speed and turbulence class.

Following the methodology for gust detection from operational data presented in Hiperwind D2.3 (Kelly and Vanem, 2022), it becomes relevant to embed realistic transient event histories in load simulations, and compare their effect on loads to the synthetic events prescribed by the IEC standards.

4.4.1 Turbulence box generation with the Hipersim tool

As part of Hiperwind D3.1 (McWilliam et al., 2022), a new Python-based turbulence box generation tool was developed, which also has the capability to embed arbitrary time series in the load simulations, or the so-called constrained turbulence simulations (Dimitrov and Natarajan, 2017). The turbulence box generation tool is named Hipersim, and it is an open-access, open-source tool distributed under a MIT license and available to install as a Python library at pypi.org. A more detailed overview of its capabilities is provided in (Dimitrov et al., 2024b). Figure 4.16 shows a verification of the Hipersim turbulence outputs to the theoretical Mann spectrum. Further, Figure 4.17 illustrates how the application of constraints affects the properties of the turbulent wind field. The top plot in the Figure shows the wind speed along the x -axis (which is equivalent to the time dimension as the turbulence box represents a so-called "frozen turbulence" field) at a single point in the $y-z$ plane at height $z = 10m$. The blue curve shows the wind speed for a randomly generated, unconstrained turbulence box. A number of constraints are imposed (black curve), which results in wind speed following the red curve. The center and the lower plot in Figure 4.17 show a vertical cross-section of the turbulence box along the line where constraints are applied - with the middle plot showing the unconstrained field, and the lowest plot the constrained field respectively.

The constraint application capability of Hipersim was used to embed measured extreme transient event time series into turbulence boxes which were then used as inputs to aeroelastic load simulations. This study is further detailed below in Section 4.4.3.

4.4.2 Generation of non-Gaussian turbulence boxes

This subsection is based on Dimitrov et al. (2024b).

As a post-processing step, the statistics of the wind fields can be modified to obtain non-Gaussian properties while maintaining the target spectra and coherence of the Mann model. The algorithm is proposed by Rosales and Meneveau (2006) and prescribes a deformation of the original Gaussian field with a Lagrangian evolution. The method has a single adjustable parameter that influences the evolution of the field and thereby the non-Gaussian increment statistics.

Figure 4.19 shows histograms of velocity increments found for three different separations. The full lines show the increments of the non-Gaussian turbulence fields, while the dashed lines show a Gaussian fit to the distribution.

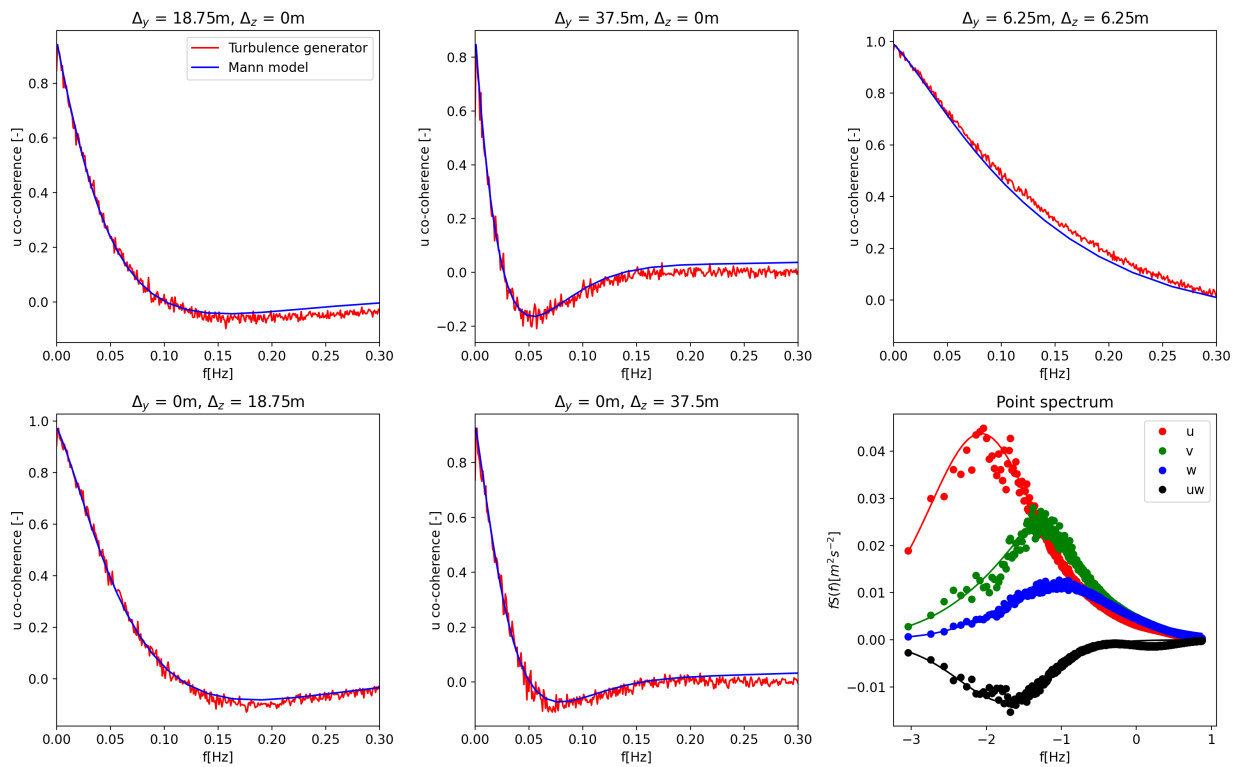


Figure 4.16: Coherence and spectra of turbulent fields generated with the Python-based tool Hipersim, compared to analytical targets. Figure is reprinted from [Dimitrov et al. \(2024b\)](#)

The impact of non-Gaussian turbulence on turbine loads was investigated by simulating the turbine under normal operations over a range of wind speeds. Overall non-Gaussian turbulence had a small impact on the loads, below we show the most extreme case where the skewness was set to -1 and the kurtosis was 6. The non-Gaussian effect amplifies large negative fluctuations in the turbulence. For above rated conditions, this creates more situations where the rotor is operated near rated conditions, where the loads are the greatest (see Figure 4.21). The results did show a more significant impact on tower top yaw moments over all wind speeds, suggesting that there is an asymmetric effect (see Figure 4.22).

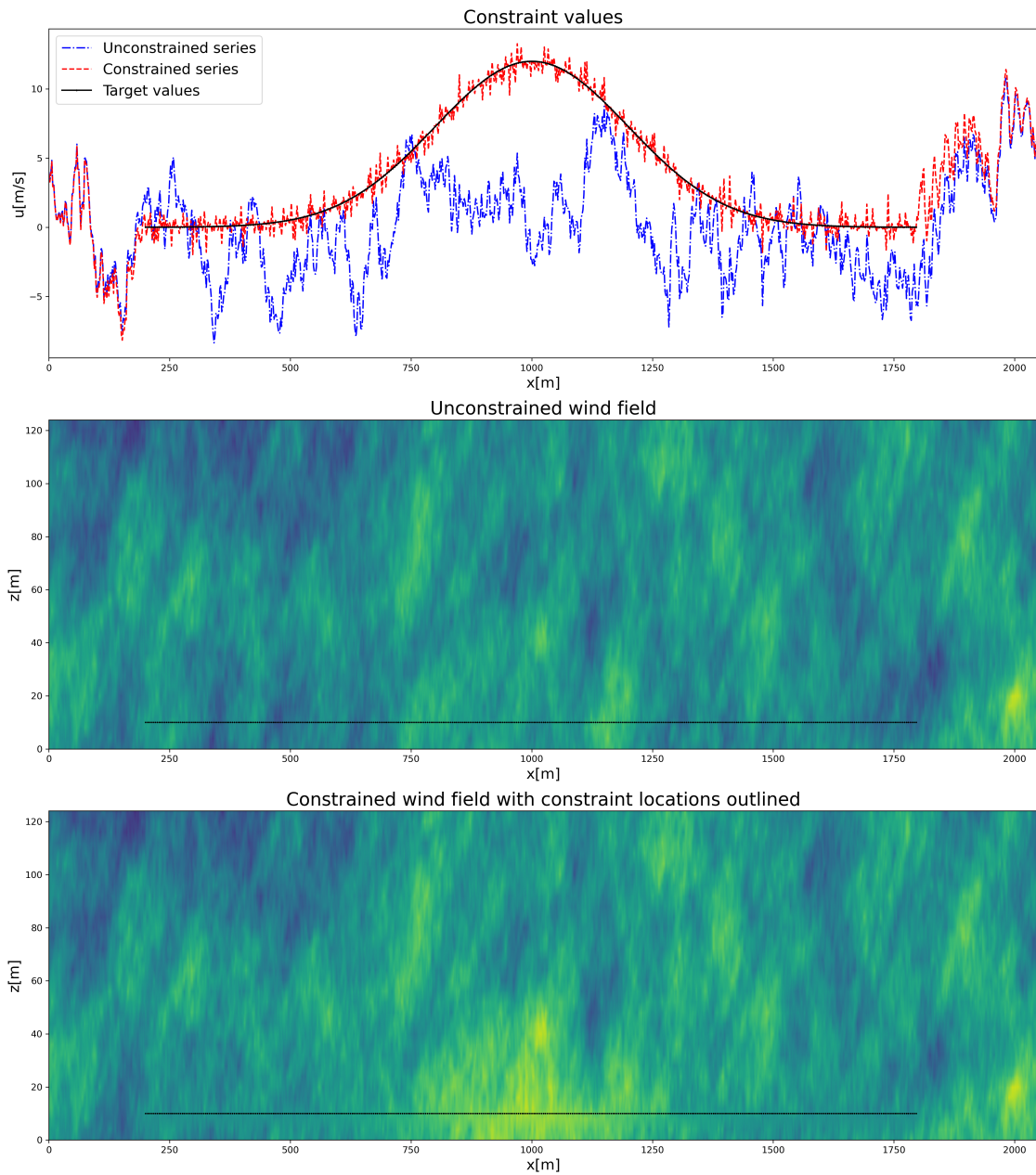


Figure 4.17: Illustration of the application of constraints in Hipersim. Figure is reprinted from [Dimitrov et al. \(2024b\)](#)

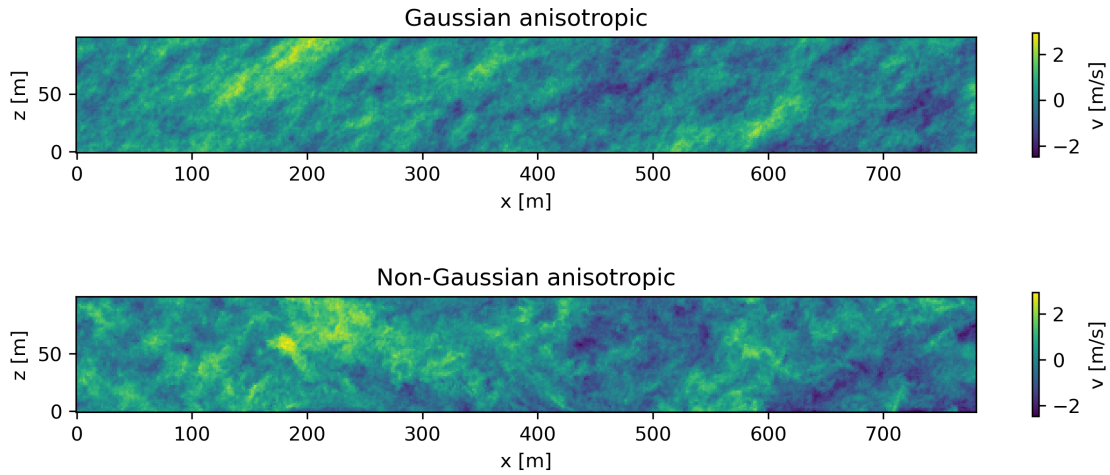


Figure 4.18: Gaussian and non-Gaussian turbulence fields of the transverse velocity component.

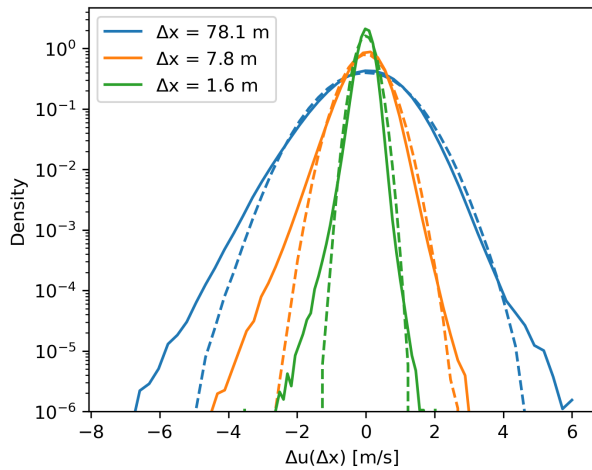


Figure 4.19: Histograms of non-Gaussian velocity increments (full lines) and Gaussian fits (dashed lines) for three different separations (Δx).

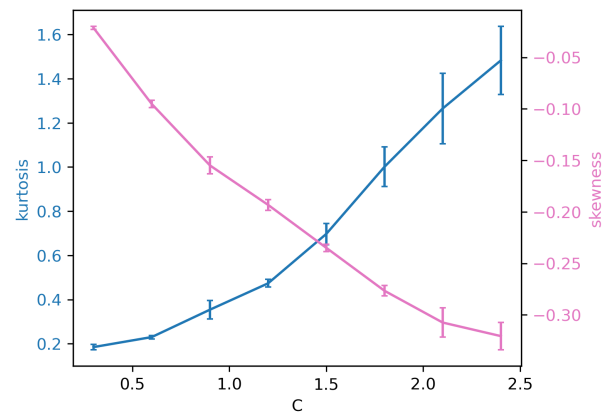


Figure 4.20: Mean skewness (pink) and mean kurtosis (blue) as function of the C parameter for 4 turbulence simulations of different seeds. Error bars show the standard deviation.

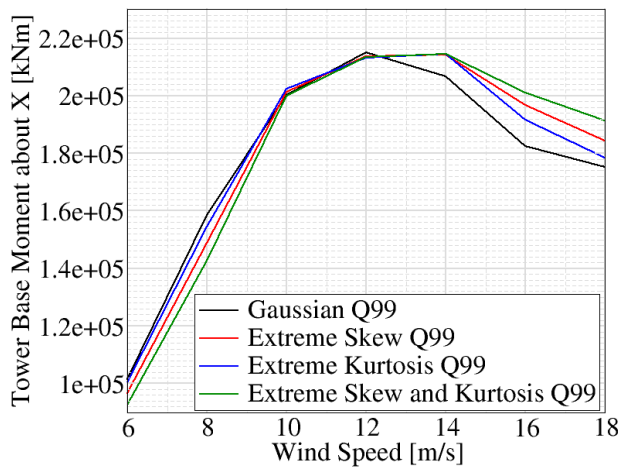


Figure 4.21: Maximum Tower Bottom Bending Moment For-Aft due to non-Gaussian turbulence

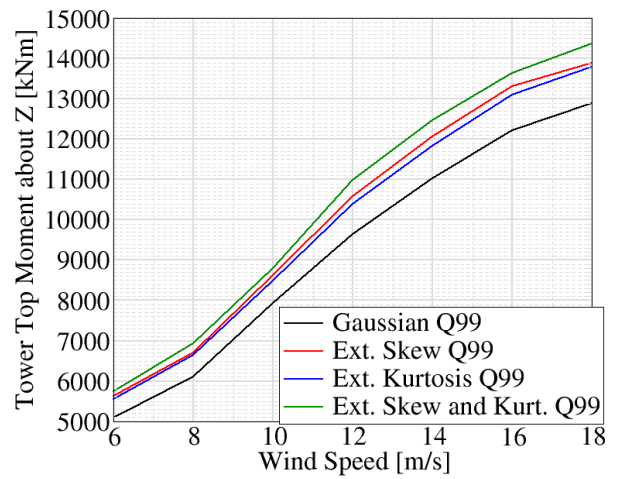


Figure 4.22: Maximum Tower Top Bending Moment For-Aft due to non-Gaussian turbulence

4.4.3 Impact of transient event profiles on wind turbine loads

The most extreme gust events identified from the work described in section 3.5 were used to investigate the impact on loads. Wind velocity time series derived from measurements were reproduced using HIPERSIM. An example of one of these events is shown in figures 4.23 and 4.24, which correspond to a significant stream-wise acceleration and change in direction respectively.

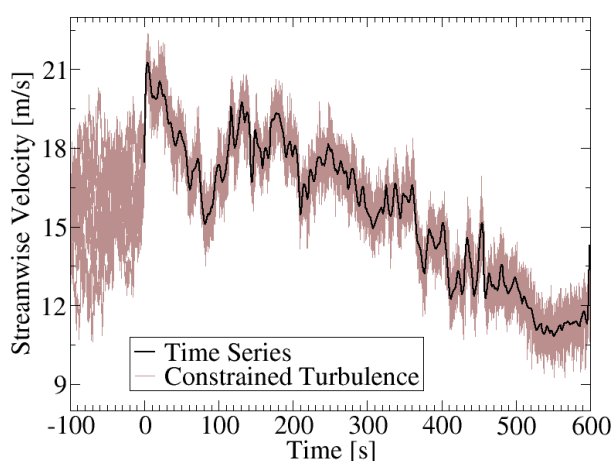


Figure 4.23: The largest filtered streamwise acceleration compared to the corresponding turbulence box generated with HIPERSIM

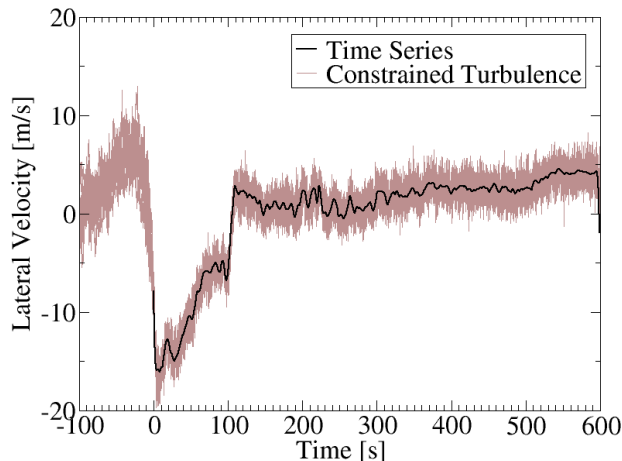


Figure 4.24: The largest filtered transverse acceleration compared to the corresponding turbulence box generated with HIPERSIM

The data only gives the velocity at a pair of points in space (100m and 160m altitude). However, the generated turbulence covers the whole simulation domain, so multiple time series placements were investigated (see Figure 4.25 below). Overall, it was found that configurations that created large coherent gust structures (i.e. the same gust applied to 4 locations on the rotor) generated the larger loads, however the difference were not significant.

HAWC2 simulations were used to compare the loads from these transient events to similar transient events defined within the IEC 41600 standards (i.e. EOG and EDC). Overall, the IEC defined events produced larger loads than the transient events (see figures 4.26 and 4.27). However, in many cases the transient event loads would exceed the IEC loads below rated. Furthermore, the IEC events are meant to represent 50-year return loads, while the significant acceleration events were taken from a 16 year data set, that was further down sampled (according to wind speed and direction) to approximately 1.3 years.

To isolate the effect of the significant acceleration events, a series of identical simulations without the event were generated. The differences in the loads are plotted in time, along with with the streamwise and transverse acceleration of the event. Figures 4.28 and 4.29 show the impact of streamwise and transverse accelerations on tower bottom over-turning moments respectively. In both cases, multiple turbulence seeds were considered. The plots show a clear correlation between the streamwise acceleration and elevated loads. However, transverse accelerations do not appear to show significant differences.

This work was the subject of a conference talk [McWilliam et al. \(2023b\)](#), and the associated data was also published as a data set [McWilliam et al. \(2023a\)](#). Two academic publications are being prepared based on this work, [McWilliam et al. \(2025b\)](#) and [McWilliam et al. \(2025a\)](#).

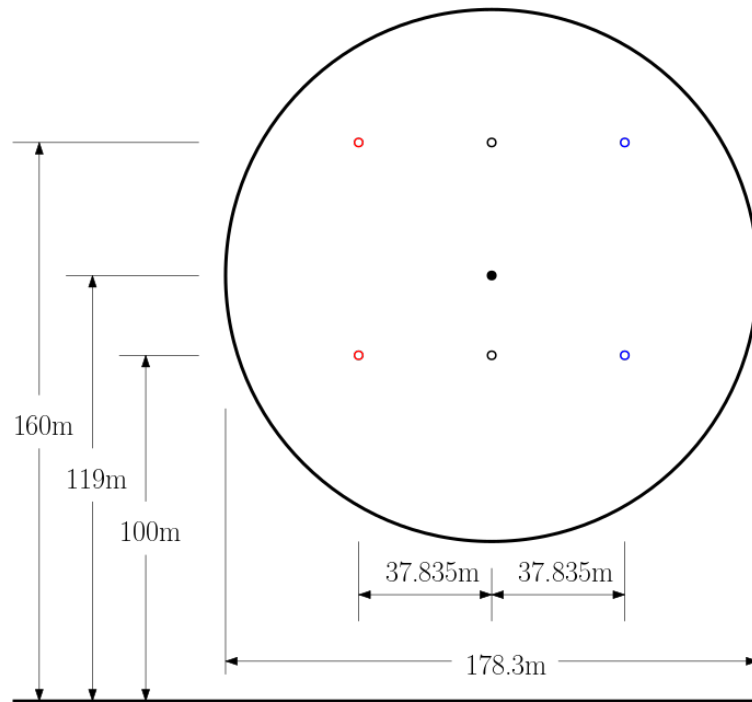


Figure 4.25: The different locations for placing the time series

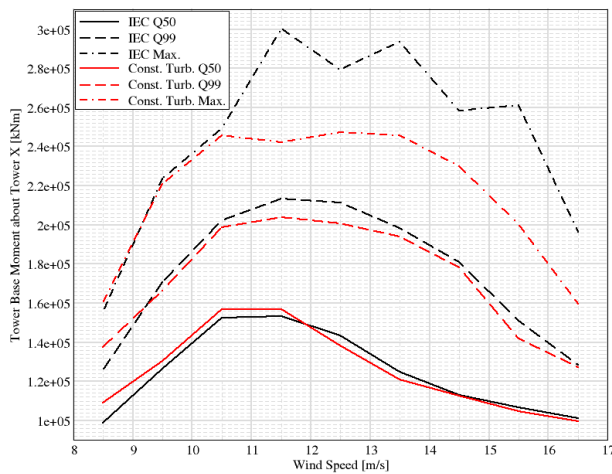


Figure 4.26: Tower bottom over-turning moment statistics, due to significant stream-wise acceleration events at 100m

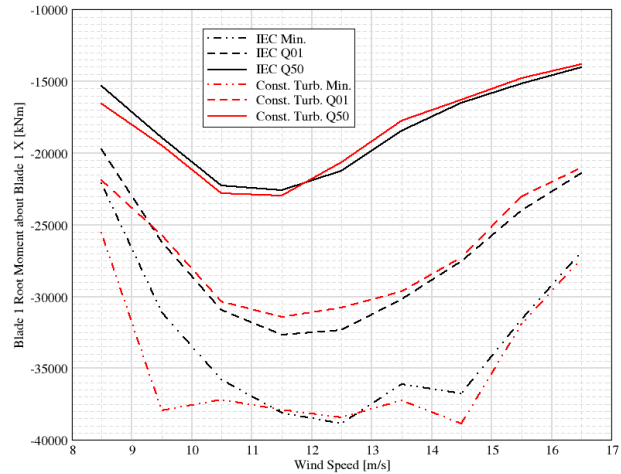


Figure 4.27: Root flapwise bending moment statistics, due to significant stream-wise acceleration events at 100m

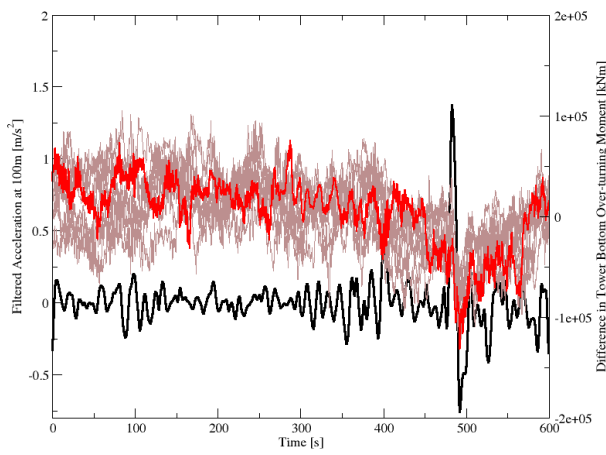


Figure 4.28: Comparison of tower bottom over-turning moment time series, due to significant stream-wise acceleration events at 100m

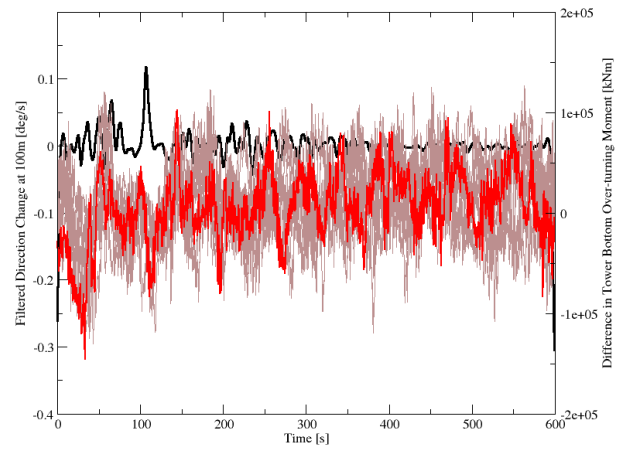


Figure 4.29: Comparison of tower bottom over-turning moment time series, due to significant direction changes

4.5 Hydrodynamics model uncertainties

This subsection and the remainder of the text in Section 4 are primarily based on Hiperwind Deliverable D3.3 (Peyrard et al., 2022).

4.5.1 Approximations of MacCamy-Fuchs approach for monopiles

Design optimization of monopile foundations requires accurate simulations of the hydrodynamics. With the increasing size of monopile diameters, the usual Morison formula is not an accurate approximation anymore. This has been mitigated by replacing the Morison formula with the less conservative MacCamy-Fuchs (MCF) solution derived from analytical solution of diffracted waves around a vertical cylinder MacCamy and Fuchs (1954). Despite this improvement, the MCF approach which is used in some engineering software like Bladed of DNV still introduces some approximation by :

- assuming the immersed foundation to be of constant radius which is not valid in particular when the Transition Piece (TP) is also partly immersed,
- not accounting properly for the full second-order wave loads, as opposed to a diffraction problem solved with Quadratic Transfer Functions,
- assume a specific stretching model for wave propagation in water depth.

A parametric study was conducted to compare MCF solutions with higher fidelity solutions of potential flow theory, to investigate the influence of each approximation listed above.

When the radius of TP is large when compared to that of a monopile, MCF can produce both overestimations (when TP crossing water surface is large) and underestimations of fatigue (when immersed TP is thin).

For the wave load order, an overestimation of the MCF model is found for short periods to the contrary of an underestimation for the long periods, Figure 4.31.

Similar conclusions are found when considering different stretching models (Wheeler and Wheeler+ Sutherland (1992) models), with up to 10% of difference in Damage Equivalent Load.

4.5.2 Uncertainty in fitting drag coefficient for floating wind turbine

The dynamics of Floating Wind Turbine is largely ruled by the floater hydrodynamics. Many floater technologies have been developed for which a detailed list goes well beyond the scope of this project. We selected here the well studied UMaine generic semi-submersible floater developed by Univ. of Maine Allen et al. (2020). It is composed of vertical cylinders piercing the water surface and immersed pontoons of rectangular sections, Figure 4.32 which may trigger complex flow patterns including vortices, leading to quadratic damping on the floater motion. Such behaviour is represented in engineering aero-servo-hydro-elastic simulators by a drag term in Morison formula which can be fitted after experimental basin tests Venugopal et al. (2006) or numerical CFD Clément et al. (2022).

Two solvers were compared in this study. The first solver employs the OpenFoam® open source software with Volume Of Fluid approach Hirt and Nichols (1975) for the air/water multi-phases modeling and Fluid-Structure Interaction (FSI). Appropriate relaxation is used at both inlet and inlet to generate waves and avoid boundary reflection in the numerical wave tank. The second solver is neptune_cfd 3D multi-field solver developed in the NEPTUNE project of EDF,

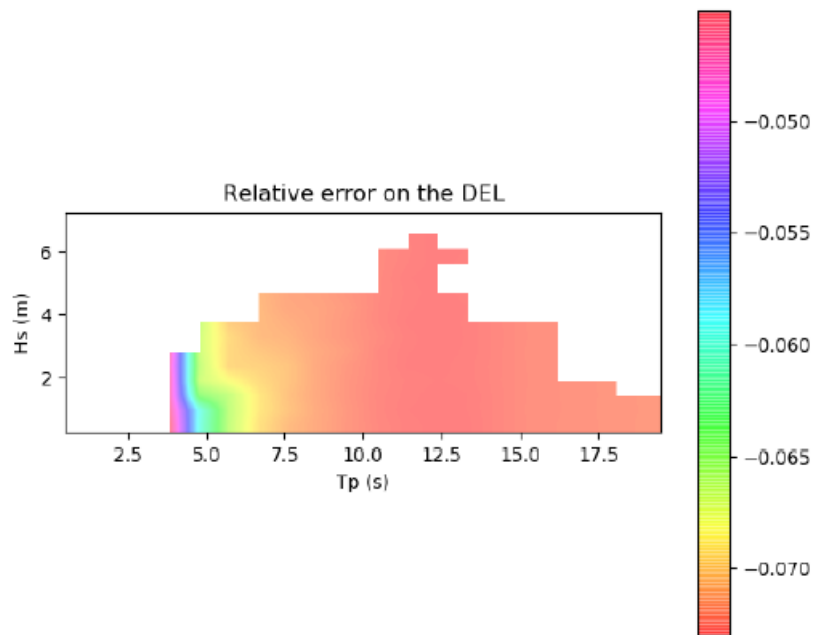


Figure 4.30: Relative DEL error between MCF and linear Potential Flow theory (positive value means MCF produces higher DEL), for a large water depth and large TP diameter modified from Teesside case study. Figure is reprinted from [Peyrard et al. \(2022\)](#).

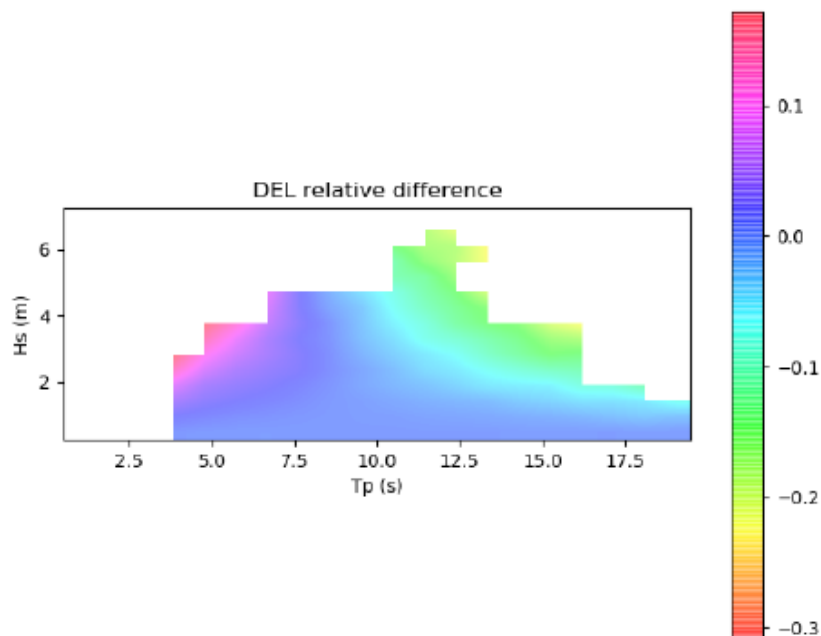


Figure 4.31: Relative DEL error between MCF and second-order Potential Flow theory (positive value means MCF produces higher DEL), for a large water depth and TP diameter of Teesside case study. Figure is reprinted from [Peyrard et al. \(2022\)](#).

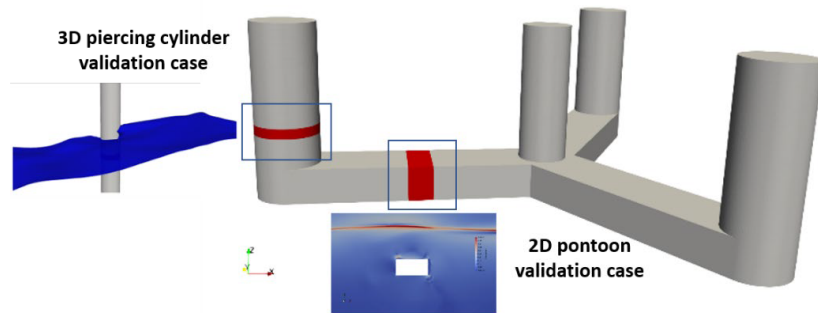


Figure 4.32: UMaine floater sketch with components modelled by CFD in red. Figure is reprinted from [Peyrard et al. \(2022\)](#).

CEA, Framatome and IRSN. It is based on a two-fluid approach with a single pressure [Mimouni et al. \(2010\)](#), a porosity FSI approach [Ishii \(1975\)](#), and Large Interface Model of [Hirt and Nichols \(1975\)](#) for air/sea interface. A relaxation with the addition of source terms is used for generation and absorption of waves at inlet and outlet.

The Morison formula is written as follows :

$$F_{mx} = \rho V C_{mx} \dot{u}_x + \frac{1}{2} S_x C_d u_x |u_x|, \quad (4.1)$$

where x is the direction of the load, u the relative velocity of the object, ρ the fluid density, V the volume of the solid, and S_x the projected surface of the solid on a plane normal to the x -axis.

Two methods of extraction of drag coefficients from CFD loads on the structure were tested. The first method is the commonly used least square one, called L_2 in the following. As this method may be sensitive to a phase shift error in the hydrodynamic force time series, a second method called "order 3" was defined in [Arai \(1993\)](#), approximating the force with a Fourier decomposition at order 3. However this method relies on a small term of the time series which may also produce error.

The results for an immersed pontoon are shown on [Figure 4.33](#) with good reproduction of experiments for both methods over a large range of wave conditions measured by the Keulegan-Carpenter (KC) number. An uncertainty is however observed, depending on the turbulence model (difference between the two neptune_cfd results), the FSI and multiphase assumptions (difference between the 2 solvers), and the theoretical particle velocity method (difference between the two OpenFoam® results).

A similar validation was conducted for a vertical cylinder piercing the sea level. Finally, the fitting was performed with the whole model of the UMaine floater, considering the forces on different zones represented on [Figure 4.34](#). As illustrated in [Figure 4.35](#), the fitted drag value is largely varying, depending on the fitting method, with some possible large error like the strong overprediction of the L_2 method for small KC with pitch forced motion.

This study underlines the need to consider not only a constant value for the drag coefficient of a floater component in engineering hydrodynamic simulation using Morison approach, but consider instead an uncertainty in this coefficient ruling the floater damping and then may have

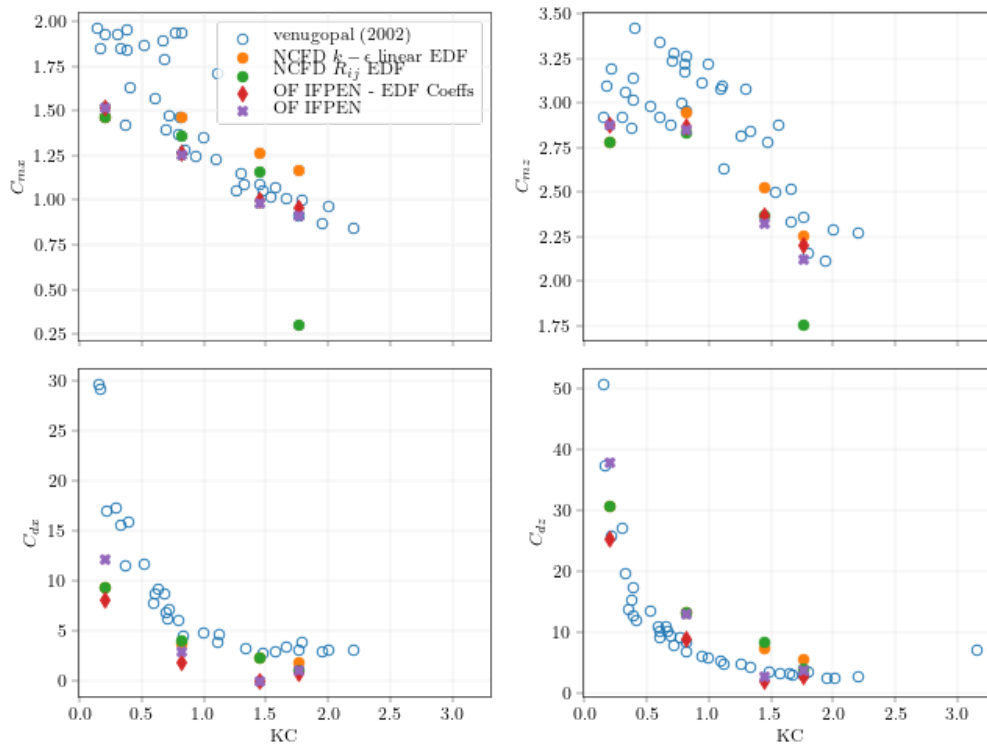


Figure 4.33: Neptune_cfd (colored dots), OpenFOAM® (cross and diamonds) results of L_2 fitting, compared to experiments of Venugopal (2002). Figure is reprinted from Peyrard et al. (2022).

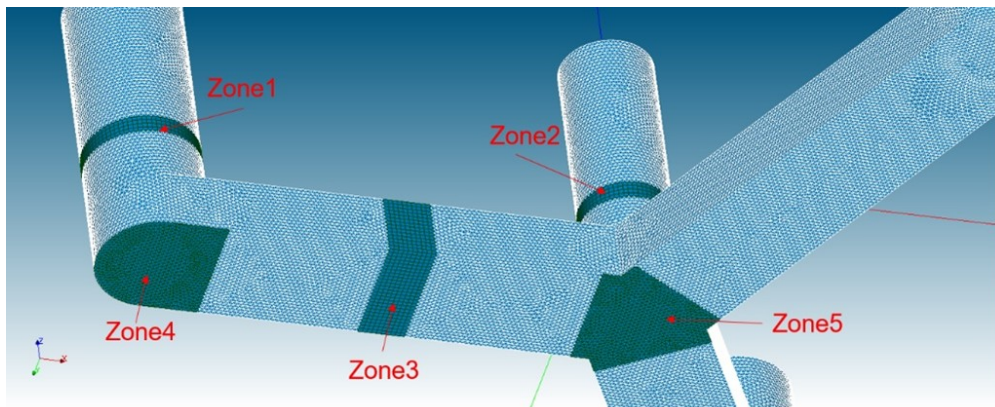


Figure 4.34: Zones used to extract the Morison coefficients. Figure is reprinted from Peyrard et al. (2022).

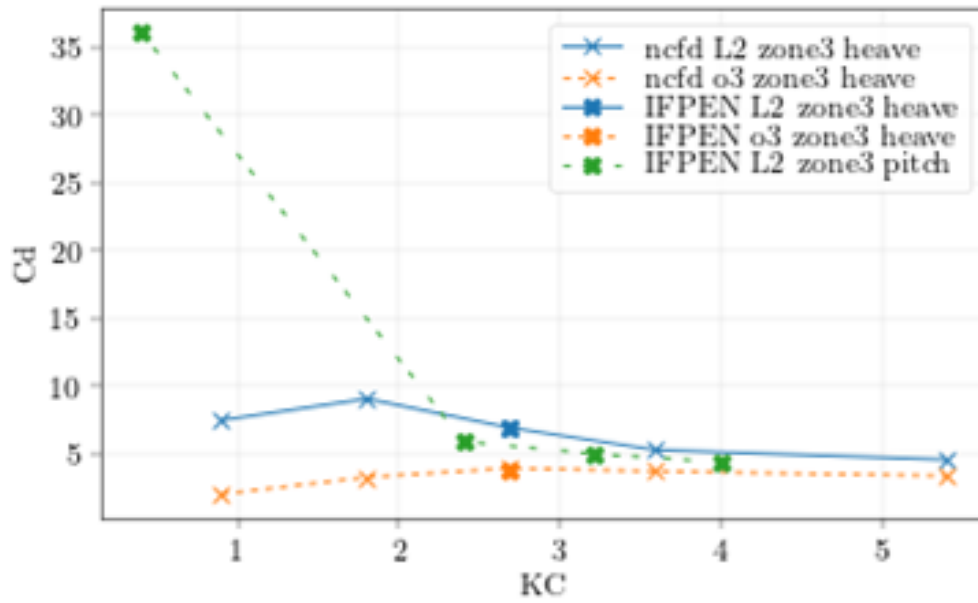


Figure 4.35: Drag coefficient for zone 3, with two different extraction methods. Heave and pitch imposed motions. KC varying. Figure is reprinted from [Peyrard et al. \(2022\)](#).

consequence on the fatigue life of the structure. Also, additional work should be paid on the fitting procedure itself, to get a robust prediction.

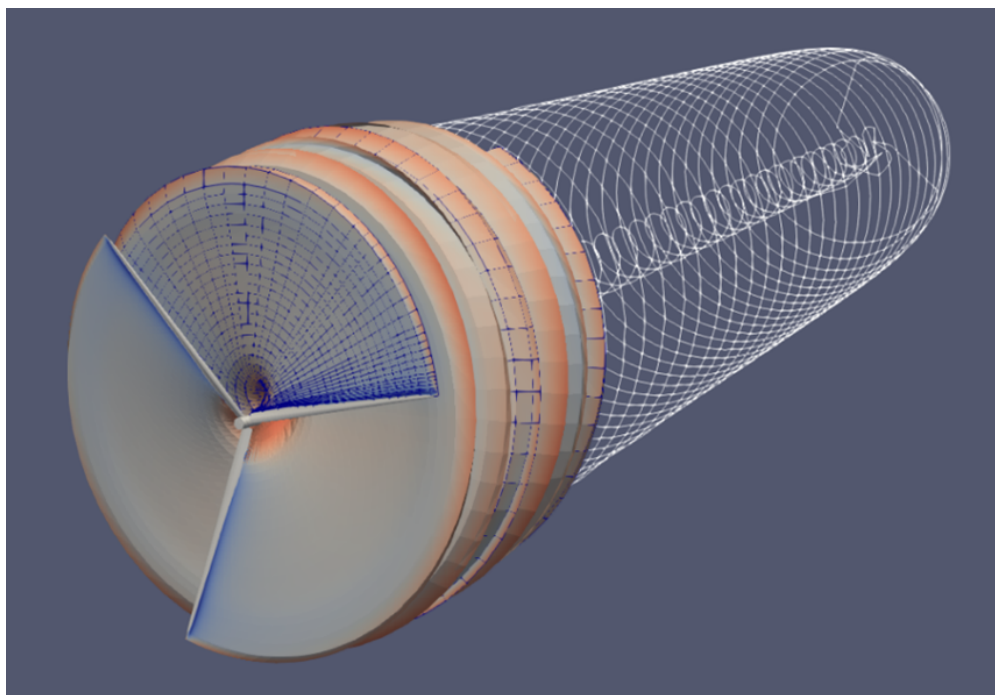


Figure 4.36: 3D illustration of a of wake accommodation technique with the CASTOR library [Blondel et al. \(2024\)](#). In the near wake, the size of the filaments (vortex elements) increases progressively (“shed merging” technique). After a transition, only the tip vortices remain to model the far wake. For this illustration, the wake has been frozen. Figure is reprinted from [Peyrard et al. \(2022\)](#).

4.6 Aerodynamics model uncertainties

The usual aerodynamics approach in fully coupled multiphysics is the Blade Element Momentum (BEM) approach [Glauert \(1935\)](#) which allows to reduce the computational time to accessible levels. This approach may however introduce strong approximations, in particular for complex 3D and dynamic flow patterns with large highly flexible wind turbines recently developed [Shaler et al. \(2023\)](#).

In this study, we took advantage of the higher fidelity model CASTOR of IFPEN which is based on lifting line theory with vortex filaments for both blade and wake discretization. We will use the term “Vortex simulations” for it in the following. It includes the viscous flow along the blade as it uses aerodynamic polars. The model was first optimized with a reducing strategy combining shed merging (filaments representing the time variation with blade rotation), and a transition to tip vortices only at downwind distance from the rotor, see Figure 4.36.

To interpolate the information in the space of stationary wind parameters (mean speed, turbulence, direction), we choose to use a Gaussian Process (GP) regression which has the advantage to provide naturally an information on the uncertainty of this interpolation with its standard deviation. It is then possible to use it to define iteratively new points of computations for reducing this uncertainty. For example, Figure 4.37 represents the GP of the time-averaged power on a cloud of points defined by a Latin Hypercube Sampling (LHS), computed from few simulations with Vortex simulations (black points). Similar GP were built for other quantity of interest: the flapwise and edgewise Damage Equivalent Loads (DEL) of blades, and the time-averaged aero-

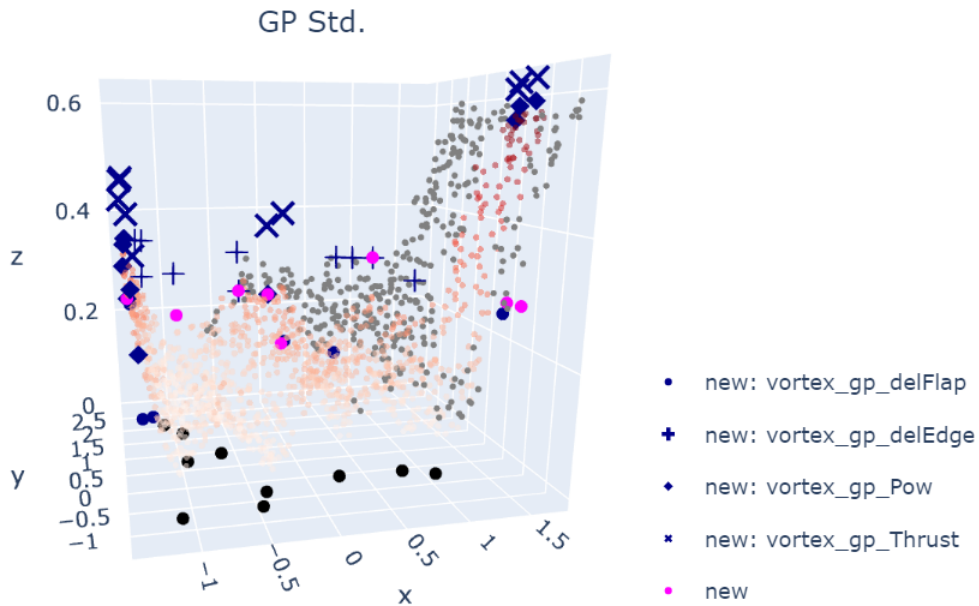


Figure 4.37: GP std of the time averaged power from Vortex simulations, with candidates and new points selected for the second iteration of the DoE. Figure is reprinted from [Peyrard et al. \(2022\)](#).

dynamic thrust. For each of them candidate to compute new simulations are chosen to reduce the uncertainty. Finally, the magenta represent the new set of points that are manually selected among these candidates with a minimum distance between them to avoid redundancy.

The accessible computational cost of BEM allows to make substantial DoE. We performed 300 simulations for the Teesside case study with fixed foundation distributed in the 3D space of wind parameters. By contrast the Vortex simulations are much longer to compute, so that the iterative procedure was done to get a good distribution of 30 of them.

For the second case study of a floating wind turbine in South Brittany, it was required to extend the parameter space to 6D for including wave parameters. DoE of 700 BEM points and 60 Vortex points were computed with similar procedures.

The approximations of BEM when compared to higher fidelity Vortex simulation, can be quantified over the whole parameter space with the difference of the GPs based on BEM and on vortex simulations. Figure 4.38 shows this difference according to the mean speed, for the time-averaged thrust. It can be seen that this difference is small for the fixed case (about 2% for the thrust between the means), while a larger discrepancy is noticed at the rated wind speed for the floating case. The latter may be explained by the fact that the blade pitch and torque ROSCO controller of the IEA-15 MW wind turbine was tuned according to BEM simulations and thus is not consistent with the Vortex simulation.

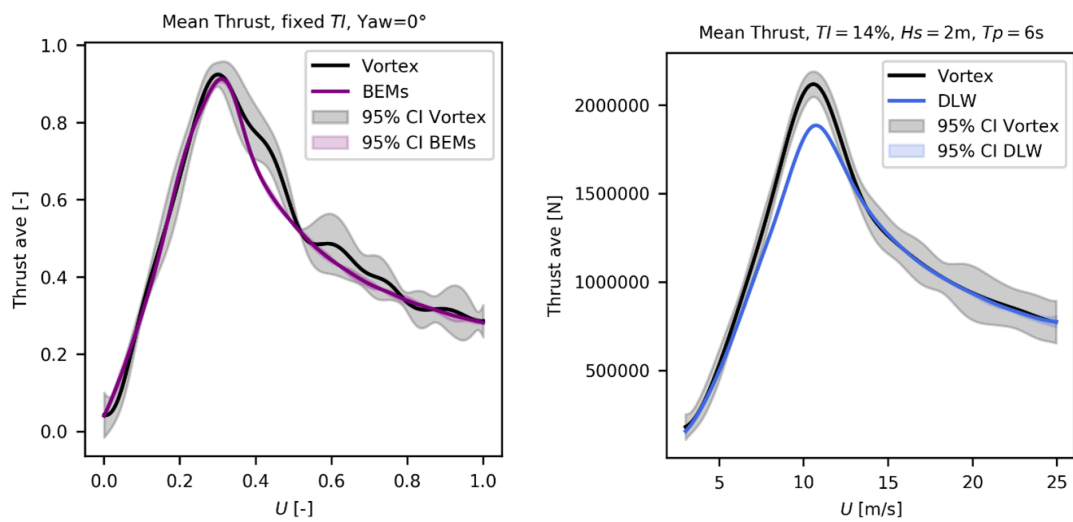


Figure 4.38: Mean and standard deviation of GP for the time-averaged aerodynamic thrust from BEM and Vortex simulations. Teesside case study (left), South Brittany case study (right). Figure is reprinted from [Peyrard et al. \(2022\)](#).

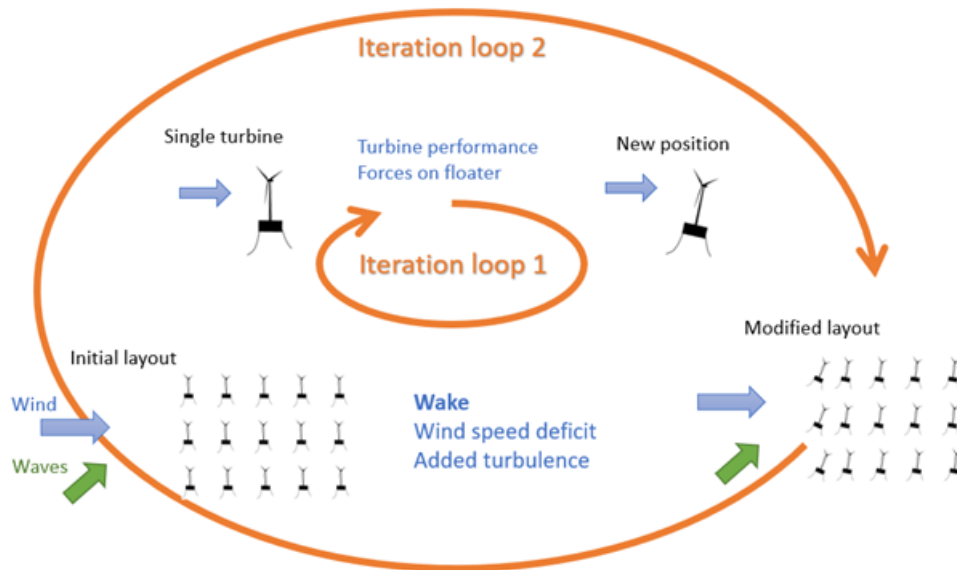


Figure 4.39: Representation of the two nested iterative loops solving the wind field in the farm. Figure is reprinted from [Ardillon et al. \(2022\)](#).

4.7 Wake analysis for floating wind turbines

An additional complication for the future floating wind farm design is that floater motion should influence the power production and the fatigue life of the structures, [Doubrawa et al. \(2021\)](#); [Johlas et al. \(2021\)](#). Actually, the main influence is double, first due to the rotor inclination which rules the power production, and second due to an uplift of the wake generated by the floater. This study of HIPERWIND project has developed a new software which takes into account the time-averaged floater motion, its influence on the wake, i.e. wind speed deficit and added turbulence for downwind turbines, and the feedback of the time-averaged aerodynamic thrust on the floater motion. This process is implemented by means of a double loop, as illustrated in Figure 4.39.

The new model was applied on the theoretical floating wind farm at South Brittany considered as a case study in Hiperwind. Its layout is composed of 5 per 5 IEA 15MW turbines on UMaine semi-submersible floaters with 7D (resp. 5D) inter-turbine distance along main wind (resp. crosswind) directions. It was found that the displacement components of the time-averaged motion of the floater have negligible consequence on the layout geometry and on the production or structure loads. By contrast, the pitch inclination of the floater has a noticeable influence, first on the wake uplift which can be seen on Figure 4.40.

This effect should be profitable for the production and is maximum at rated wind speed for which the aerodynamic thrust reaches a maximum. However, as represented in Figure 4.41, its effect partially cancels out with the rotor inclination direct negative effect on the production. This pioneering study motivates future investigations with less approximations and other case studies to confirm or not the balance of the counteracting effects. In particular a more accurate computation of the rotor performance curves C_p , C_t for production and thrust should be considered taking into account the difference of the mooring system stiffness according to the wind direction. Also, the consequence of the floater inclination was modeled here similarly to the yaw correction, e.g. for wake steering in wind farm control. Hence, a more physical modeling may include interactions between the wakes and the vertical shear of the wind flow or with Dynamic Wake Meandering.

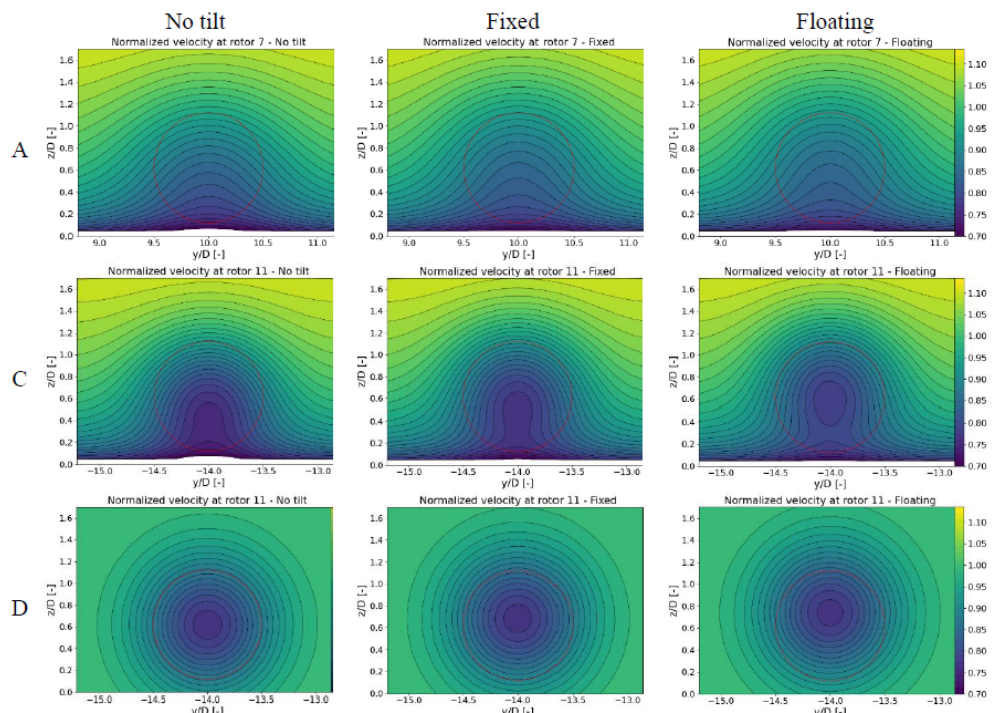


Figure 4.40: Axial velocity profile ahead of the second rotor in the middle row depending on the wind direction. Case A (top): 8m/s, head-wind with vertical shear. Case C (middle): 11m/s, crosswind with vertical shear, Case D (bottom): 11 m/s crosswind, no vertical shear. The rotor is represented as a red dashed line. Figure is reprinted from [Ardillon et al. \(2022\)](#).

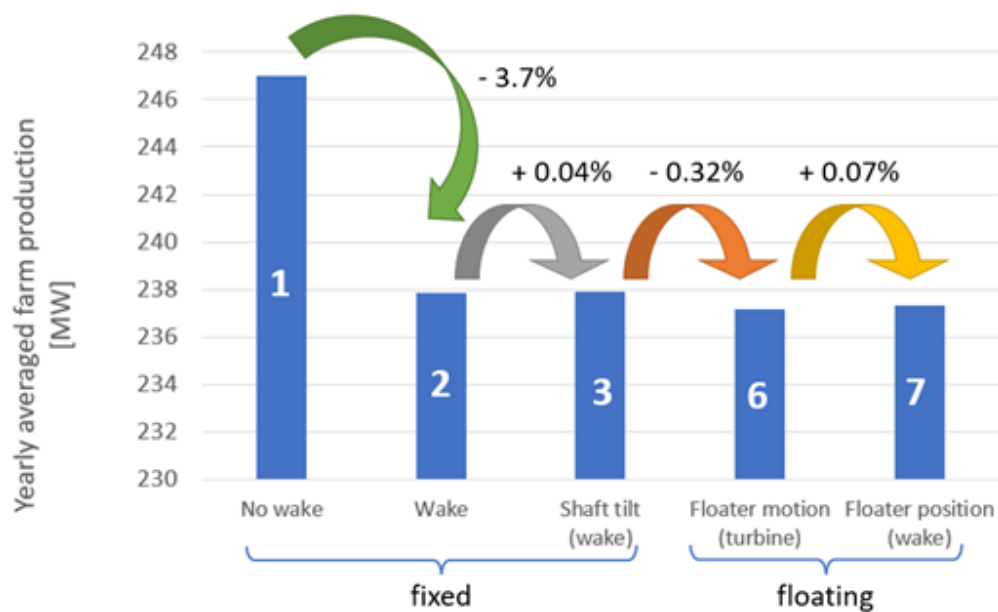


Figure 4.41: Yearly averaged farm production taking different effects into account. Figure is reprinted from [Ardillon et al. \(2022\)](#).

5 Advanced uncertainty propagation and structural reliability assessment methodologies (WP4 outcomes)

5.1 Surrogate Modelling of High-Dimensional Input/Output Time-Series

5.1.1 Introduction

Surrogate modeling is crucial in reducing the computational burden of aero-servo-elastic (ASE) simulations for wind turbine reliability assessment. These models offer a computationally efficient alternative to full simulations, enabling extensive design exploration and uncertainty quantification. The focus of this section is on the development of a sequence of surrogate models capable of predicting time-series outputs from high-dimensional input time-series, specifically in the context of wind turbine dynamics. This Section is based on the HIPERWIND report D4.1 [Dimitrov et al. \(2022\)](#), as well as on the follow-up journal paper [Schär et al. \(2024\)](#).

5.1.2 Problem Statement

The behavior of a wind turbine under varying environmental conditions can be abstracted as a deterministic function:

$$y(t) = \mathcal{M}(\mathbf{x}(\mathcal{T} \leq t)). \quad (5.1)$$

where $\mathbf{y}(t)$ represents the time-dependent output quantity of interest (QoI) such as rotor speed, blade pitch, and power output, and $\mathbf{x}(t)$ is a set of input time-series such as wind speeds and the turbine's state variables. The objective is to approximate the deterministic model \mathcal{M} with a surrogate model $\hat{\mathcal{M}}$ that is computationally inexpensive to evaluate:

$$y(t) = \mathcal{M}(\mathbf{x}(\mathcal{T} \leq t), \beta) \approx \hat{\mathcal{M}}(\mathbf{x}(\mathcal{T} \leq t), \hat{\beta}). \quad (5.2)$$

while ensuring that the approximation error remains within acceptable limits.

5.1.3 Computational Model and Validation

The surrogate models are trained and validated using simulations of the NREL 5MW reference wind turbine ([Jonkman et al., 2009](#)), implemented in the OpenFAST ASE simulator ([NREL, 2021](#)). The validation is conducted against a large dataset comprising approximately 2,000 simulations, representing different wind scenarios, including a normal turbulence model (NTM), extreme turbulence model (ETM), and extreme operating gusts (EOG) as defined by the IEC standard [IEC \(2019b\)](#).

Turbulent wind fields are generated using the TurbSim software ([Jonkman, 2009](#)), which produces 3D wind speed matrices for the longitudinal, transverse, and vertical wind components. These matrices are discretized both spatially and temporally.

The accuracy of the surrogate models is evaluated using error metrics such as root-mean-square error (RMSE) for time-series predictions, and statistical measures like Damage Equivalent Load (DEL) for fatigue analysis.

5.1.4 mNARX autoregressive modelling

Aero-servo-elastic simulators are characterized by a high input dimensionality (the entire turbulence boxes), strong non-linearities, and active control systems. This complexity cannot be handled with classical surrogate modelling techniques, which led us to the development of the novel mNARX (manifold Nonlinear Auto-Regressive model with eXogenous inputs, ([Schär et al., 2024](#))) surrogate model. This method leverages both the spatial coherence of wind fields and the temporal dependence of QoIs, and is schematically represented in [Figure 5.1](#).

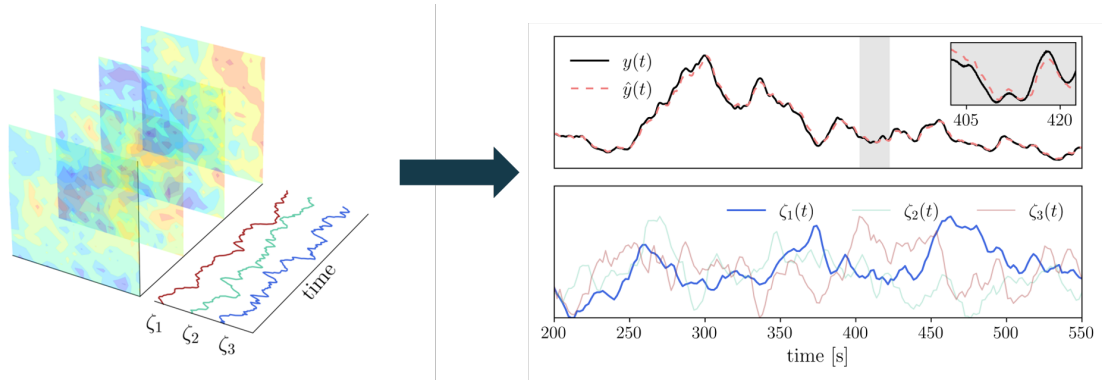


Figure 5.1: Graphical representation of the mNARX surrogate modelling strategy

Leveraging spatial coherence: dimensionality reduction To manage the high dimensionality of the input wind fields, the spatial dimensions of the turbulence box $\mathbf{V}(t)$ are reduced to a small set of spatial modes $\boldsymbol{\xi}(t)$ using the Discrete Cosine Transform (DCT), focusing on the low-frequency modes that have the most significant impact on the turbine response. An example of the effects of this compression is given in Figure 5.2.

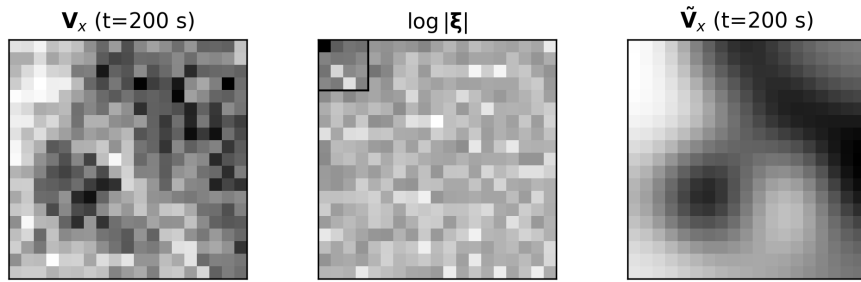


Figure 5.2: Original vs. reconstructed wind field after truncating its spectral representation to the first 16 DCT modes. Left: original 2D turbulence box slice. Middle: 2D DCT coefficients. Right: reconstructed turbulence box slice after truncation.

Construction of an input manifold Once the dimensionality of the exogenous input is reduced via the DCT, additional input features $\mathbf{z}(t)$ can be added to an input manifold $\boldsymbol{\zeta}(t) = \{\boldsymbol{\xi}(t), \mathbf{z}(t)\}$. The set of features $\mathbf{z}(t)$ can comprise both additional exogenous inputs/features, or auxiliary quantities that can be needed to properly predict the dynamics of the system response. For a wind turbine, typical examples include: blade pitch, rotor angular speed, rotor azimuth, etc..

Final NARX model Once the full input manifold $\boldsymbol{\zeta}(t)$ has been constructed, a classical NARX model can be used to predict the time evolution of a desired QoI $y_i(t)$ as a function of the input manifold:

$$\hat{y}_i(t + \delta t) = \tilde{\mathcal{M}}\left(\hat{y}_i(t), \hat{y}_i(t - \ell_1^y), \dots, \hat{y}_i(t - \ell_{n_y}^y), \boldsymbol{\zeta}(t + \delta t), \boldsymbol{\zeta}(t), \boldsymbol{\zeta}(t - \ell_1^\zeta), \dots, \boldsymbol{\zeta}(t - \ell_{n_\zeta}^\zeta)\right), \quad (5.3)$$

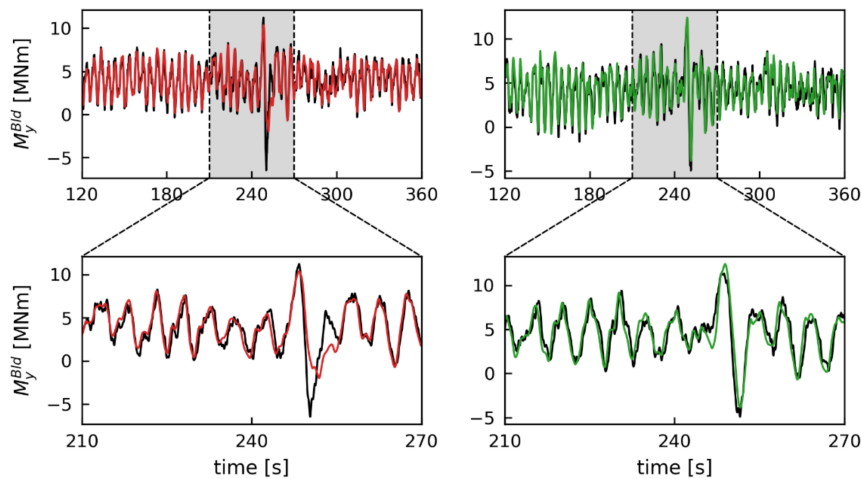


Figure 5.3: Graphical representation of the performance of the mNARX surrogate for the blade root moment for a realization in the extreme operating gust out-of-sample validation set. Left: prediction (red) with high relative error with respect to the true response (black); Right: prediction (green) with low relative error with respect to the simulator output (black).

where the ℓ_{\bullet} indicate the total number of lags considered for each manifold and autoregressive input. For more details on the choice of lags, as well as the construction of the input manifold, the reader is directed to [Schär et al. \(2024\)](#).

5.1.5 Surrogate performance

The performance of the mNARX surrogate model is assessed across different wind regimes and for different QoIs. Overall, it achieves high accuracy, particularly in extreme wind conditions, with a slight reduction in the intermediate wind speed regimes. A summary of its performance is given here:

- The surrogate demonstrates overall high stability and satisfactory accuracy across the various wind regimes;
- This holds both for instantaneous responses (e.g. instant power output or bending moments), and for integrated quantities (e.g. maximum 10-minutes loads, fatigue loads or total energy produced);
- Computational training costs are relatively low, with satisfactory performance reached with as few as 100 training simulations.

An example of the performance of the surrogate on a realization of the extreme operating gust out-of-sample validation set [Schär et al., 2024](#) is shown in Figure 5.3.

5.1.6 Conclusions

The mNARX surrogate models offer significant computational efficiency, reducing simulation time by orders of magnitude while maintaining acceptable accuracy. Its novelty, flexibility and computational efficiency have been published in a number of follow-up works: [Schär et al. \(2023a,b\)](#); [Wang et al. \(2024\)](#); [Schär et al. \(2023c\)](#).

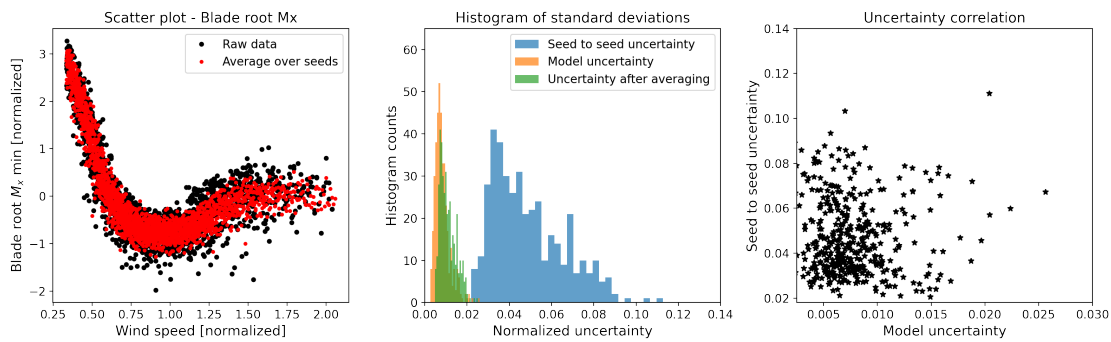


Figure 5.4: Comparison of epistemic (model) uncertainty and aleatory (realization-to-realization) uncertainty effects for extreme blade root flapwise bending moments. Left: scatter plots raw data including aleatory uncertainty and averages over multiple seeds (realizations) at each sample point; Center: histograms of the model uncertainty compared to the realization-to-realization uncertainty; Right: correlation between the model uncertainty and the realization-to-realization uncertainty.

5.2 Probabilistic surrogate models using Bayesian Neural Networks

This section follows the work described in Hiperwind D4.1 (Dimitrov et al., 2022).

Regression models based on Feedforward Neural Networks (FNN) (Goodfellow, et al., 2016) are a popular surrogate modelling approach (Dimitrov, 2019), (Schröder, et al., 2018) that has some well-known advantages. However, the standard FNN-based surrogate models provide a deterministic prediction, and the uncertainty is not a direct output of the models. The so-called Bayesian Neural Networks (BNNs) (Blundell, et al., 2015) are a modification of FNNs where the deterministic model parameters are replaced with probabilistic ones, resulting in a model that can give uncertainty estimates. As part of Hiperwind D4.1, we applied BNNs for training probabilistic load assessment surrogates. The work focused on answering the following research questions:

1. How can we use BNNs to build accurate wind turbine load and power output surrogates that also represent the uncertainties in an adequate way?
2. How adequate are BNN models for specific probabilistic design applications such as a) predicting the tail distribution of load extremes and b) modelling the full probability distribution of aggregate quantities (such as fatigue loads) including uncertainties?
3. What is the performance of BNNs in comparison of other alternatives such as running an ensemble of deterministic models?

This study demonstrated how Bayesian Neural Networks (BNNs) can be used as probabilistic surrogate models for wind turbine load and power prediction. Their performance was evaluated with the aeroelastic model of the Teesside wind turbine, and compared against the performance of an alternative probabilistic surrogate based on an ensemble of deterministic Feedforward Neural Networks (FNNs). The models were trained on aeroelastic simulations over 2000 different experimental samples with varying environmental conditions in a 4D experimental space (wind speed, turbulence, wind shear and air density). Twenty different turbulence realisations were generated for each sample, leading to 40000 aeroelastic simulations in total used for model training and testing.

Figure 5.4 compares the effect of two types of uncertainty present in the simulations and models

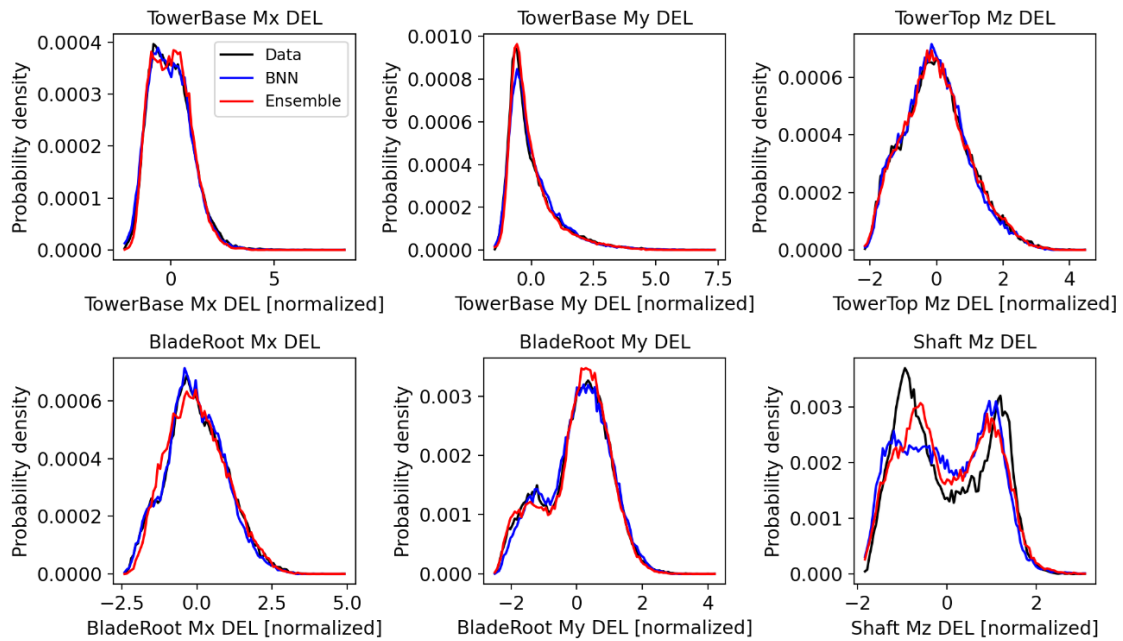


Figure 5.5: Comparison of the probability densities of fatigue damage-equivalent load predictions from a BNN model and an ensemble of deterministic models, for six wind turbine load signals.

trained on them: 1) the realization-to-realization uncertainty, and 2) the statistical uncertainty for a model trained on a finite amount of data, estimated by training multiple models and evaluating ensemble statistics. As visible from Figure 5.4, the realization-to-realization uncertainty is dominating and has bigger variance than the statistical model uncertainty. Averaging over 20 seeds (realization) brings this uncertainty down to a level comparable to the statistical uncertainty for a model trained on approximately 2000 samples. The BNN trained on the same data was able to capture both types of uncertainty and adequately represent the probability density functions of several load channels, as shown in Figure 5.5. In contrast, the predictions of the BNN for load extremes (tails of the distributions) showed some discrepancies for some load channels, as shown in Figure 5.6. Our explanation is that the tail behavior of the BNN model is driven by the choice of parametric distribution to describe the joint distribution of model parameters. As we are using a Gaussian distribution, the tail also behaves as approximately Gaussian, which is not necessarily representative for all types of load channels. Such a problem may be alleviated by choosing other distribution types.

The main conclusions of the study are summarized below:

- BNNs are a viable option for building a probabilistic surrogate model that can both take epistemic and aleatory uncertainties into account;
- Compared to an ensemble FNN model, the BNN were shown to have equal or superior performance in modelling the probability distribution of load and power outputs – while being computationally more efficient. This shows the potential of BNNs as surrogates for fatigue load and power prediction;
- The way the tail behavior is modelled is driven by the choice of the posterior distribution functions – using a joint Gaussian prescribes a Gaussian-like tail. As a result, the tail probability predictions are very similar to those from an ensemble model where the aleatory

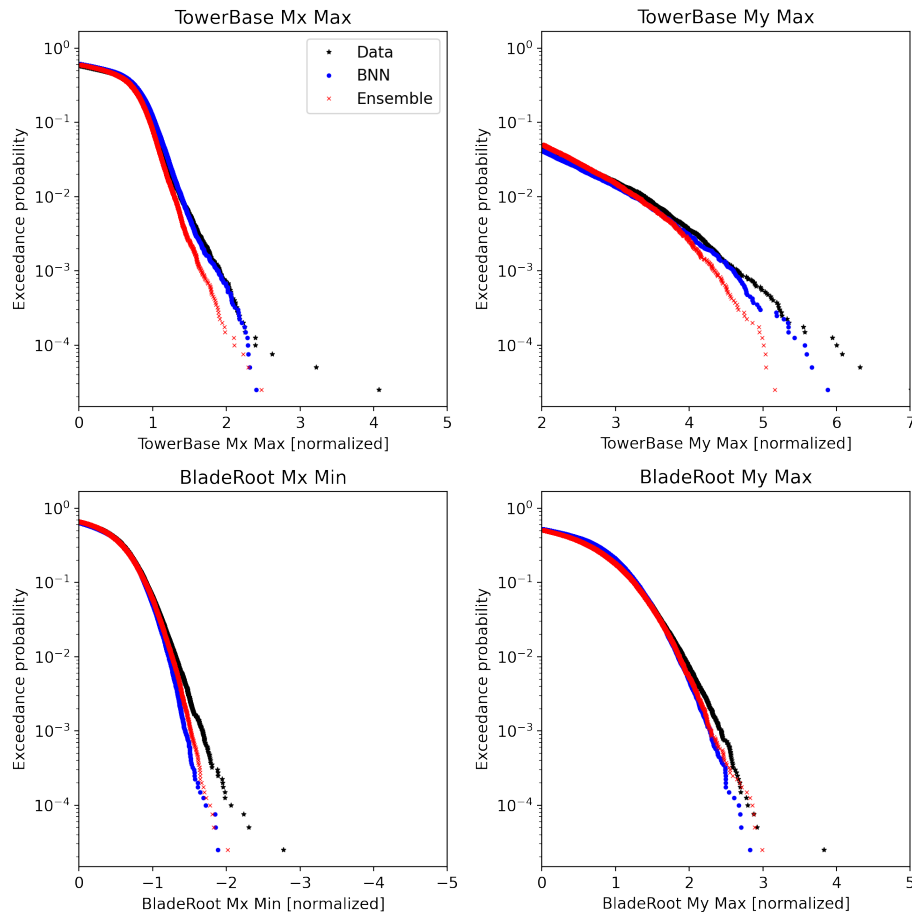


Figure 5.6: Comparison of the tail probability distribution predictions by a BNN model and an ensemble of deterministic models, for four load channels.

uncertainty is modelled as a Gaussian distribution too.

- The realization-to-realization uncertainty in the load simulations seems to be non-Gaussian, hence a more complex model with a non-Gaussian posterior may be required (but not guaranteed) to improve the tail prediction capabilities. For the type of problems presently discussed, BNNs may be an efficient alternative to Gaussian models as they show high computational performance and uncertainty prediction capabilities, while lacking the limitations of the Gaussian models in terms of deteriorating computational efficiency for large sample sizes.

5.3 Data-driven model validation and updating

This section summarizes the findings of Hiperwind task 4.5. The work is documented in Hiperwind Deliverable 4.5 (Gräfe et al., 2024).

Wind turbine loads are critical for both the design and operational phases of turbines, particularly for assessing fatigue and extreme load estimations during development. These are usually derived from numerical simulations, but for existing assets without continuous load measurement histories, estimations rely on simulations combined with environmental and operational data. Simulation tools such as Hawc2, Diego, or DeeplinesWind™ are validated for accuracy, but uncertainties remain due to factors like input measurement errors or imperfect model parameterization. To mitigate these, simpler surrogate models, often regression-based, are used to approximate aeroelastic models, though they introduce additional uncertainty. Training surrogate models directly on real-world measurements can reduce some uncertainties, though this may lead to statistical uncertainty and limited generalization. This report aims to evaluate surrogate modeling approaches in predicting real turbine loads, explore model updating to reduce uncertainty and investigate data pre-processing techniques for improved model alignment.

The load prediction models in this task are based on simulated and measured turbine load data. The field data originates from a field measurement campaign at the Teesside offshore wind farm in the North Sea near the UK. This farm consists of 27 Siemens 2.3 MW turbines, with data from Turbine 13 collected over one month (November 2020). The dataset includes SCADA and load signals used for model training and testing. Sensors, including strain, acceleration, and inclination sensors, were placed around the turbine's transition piece to capture relevant measurements. To align field measurements with simulation outputs, the strain measurements from the field campaign were converted into tower bending moments using the tower's geometry and material properties. Since the calibration factors for the strain gauges were unknown, the offsets for each strain sensor pair were manually adjusted by aligning strain measurements with wind direction and assuming minimal bending at low wind speeds. After correcting the strain data, they were converted into bending stresses using the tower's Young's modulus, and then into fore-aft and side-side bending moments. Figure 5.7 shows the simulated and measured fore-aft and side-side bending moments after the conversion.

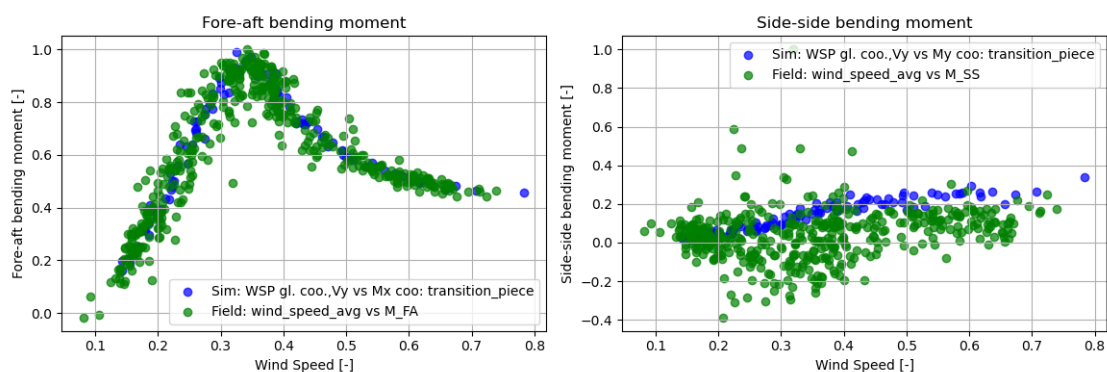


Figure 5.7: Simulation vs. field measurements. Fore-aft (left) and side-side (right) bending moment.

Figure 5.8 shows a 600-second time series prediction for field data and simulation-based data, along with the power spectral density comparison. The simulation-based model closely matches

the reference signal, accurately capturing frequencies up to 2 Hz. In contrast, the field-based model correctly predicts low-frequency variations but struggles with higher-frequency fluctuations, only capturing frequencies up to 1 Hz.

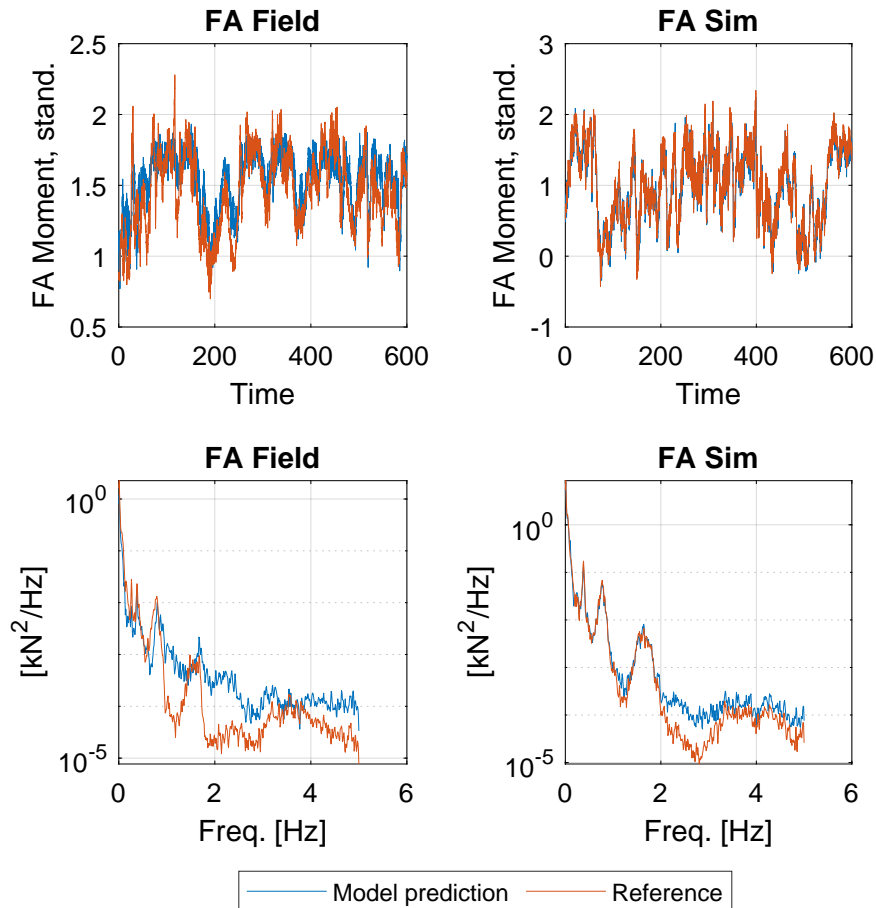


Figure 5.8: Example of time series prediction from field and simulation model, case A

Besides the individual evaluation of model performance, the transferability of simulation-based models to field conditions was studied. Here the models trained on simulated data were applied on field input data and tested on field load signals. Figure 5.9 shows a times series example of model predictions and references for different modeling cases. (A: Inclination and acceleration input, B: Inclination input, C: Acceleration input). While no correlation between prediction and reference is visible for cases A and B, the predictions of case C follow the low-frequency fluctuations of the reference signal. This indicates the potential for the transfer of simulation-based models to field conditions. In the second step, the models trained on simulation data are updated using the field measurements. This is done by retraining the simulation models using different quantities of measurement data. The prediction accuracy is then tested on unseen data from the field measurements. Here, it was observed that updating the prediction models with field measurements can improve the prediction accuracy, especially in cases where only a limited amount of field data is available for training.

In conclusion, the results suggest that combining simulation and field measurement data for model training shows promise but requires further refinement. The prediction accuracy of

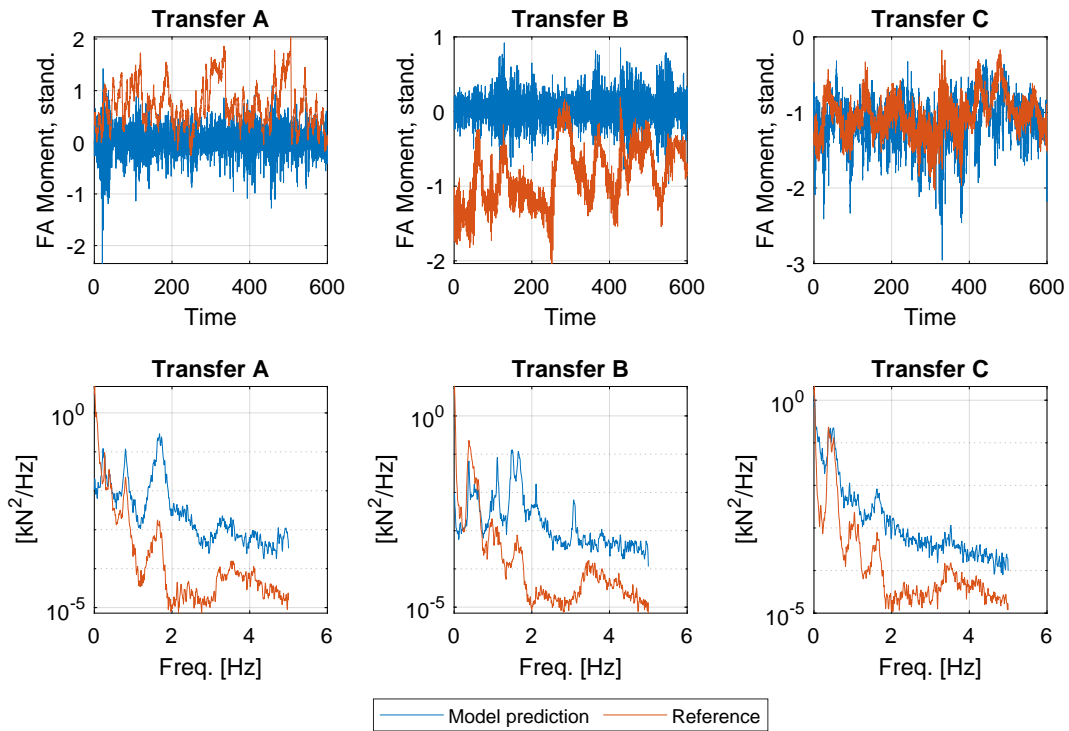


Figure 5.9: Prediction RMSEN of simulation data-based model, tested on field measurements.

transferred models is limited, likely due to differences in correlation patterns between input and output data in simulations versus field data. This issue could be addressed by improving the representation of the turbine and measurement setup in simulations to better align with measured signals. Additionally, enhanced data pre-processing techniques, such as filtering and cleaning field measurements, should be explored. While the approach shows potential, further investigation is needed to improve data preparation and model performance.

5.4 Floating wind turbine design procedure including SLS

Floating wind turbines (FWTs) can be an alternative to bottom fixed turbines, which have limitations in terms of water depth and space. The flexibility of the FWTs installation ensures access to greater wind resource. Currently, FWTs have higher costs compared to bottom fixed turbines. One reason for the higher cost is the challenging environment, but another contributing factor is the lack of well established design practices and lack of understanding of the critical design challenges. This section presents a procedure for semi-automated FWT design feasibility assessment and sensitivity analysis, which provides means of computing fatigue, ultimate and serviceability limit states (FLS, ULS and SLS). The work presented in this section is based on the HIPERWIND deliverable D4.4 (Yildirim and Dimitrov, 2024) and the article (Yildirim et al., 2024).

5.4.1 Sensitivity analysis using an automated design evaluation framework

The automated design framework includes a Python wrapper code which calls several modules responsible for computing different steps in the design evaluation process. The workflow is illustrated in Figure 5.10. We use the UMaine VoltturnUS semisubmersible floater concept (Allen et al., 2020) as a demonstration example. The first step is to parameterize the floater dimensions into several design variables that can be used as inputs for design sensitivity studies. The design variables selected for this study are: 1) the outer diameter of the tower base column, 2) the outer diameter of the buoyancy column, 3) the floater radius, 4) the draft and 5) mooring line length. The design variables can be seen in Figure 5.11.

5.4.2 System Response: Time and Frequency Domain

System responses are computed with two approaches: using either time- or frequency-domain models. We use the Hawc2 aeroelastic tool (Larsen and Hansen, 2023) for the time domain simulations. The model features flexible tower and blades, a dynamic mooring line model, and a potential flow solution for hydrodynamic loads. For the frequency domain computations, a linear model, Quick Load Analysis of Floating Wind Turbines (QuLAF) developed by DTU (Pegalajar-Jurado et al., 2018) is used. More information about the theory and implementation of this model can be found in (Pegalajar-Jurado et al., 2018; Madsen et al., 2019).

The design evaluation space limits are defined based on the site-specific conditions and operation limits of the selected turbine. A Design of Experiment (DOE) is created within these limits in order to explore the design sensitivity to the individual input variables. The DOE space is thus constrained by the surge and pitch motion limits, natural frequencies, and additional constraints. The limits for the pitch and surge motion are defined from Mahfouz et al. (2020) and Dou et al. (2020). The constraints for the natural frequencies are defined considering the wind, wave spectrum, and blade 1P and 3P frequencies (Allen et al., 2020).

5.4.3 Global Sensitivity Analysis

The effects of design variables on the system response and characteristics are investigated with global variance-based sensitivity analysis. Sobol indices are computed using a polynomial chaos expansion with the UQLab tool (Marelli and Sudret, 2014). See Sudret (2008) for the details of global sensitivity analysis using a polynomial chaos expansion.

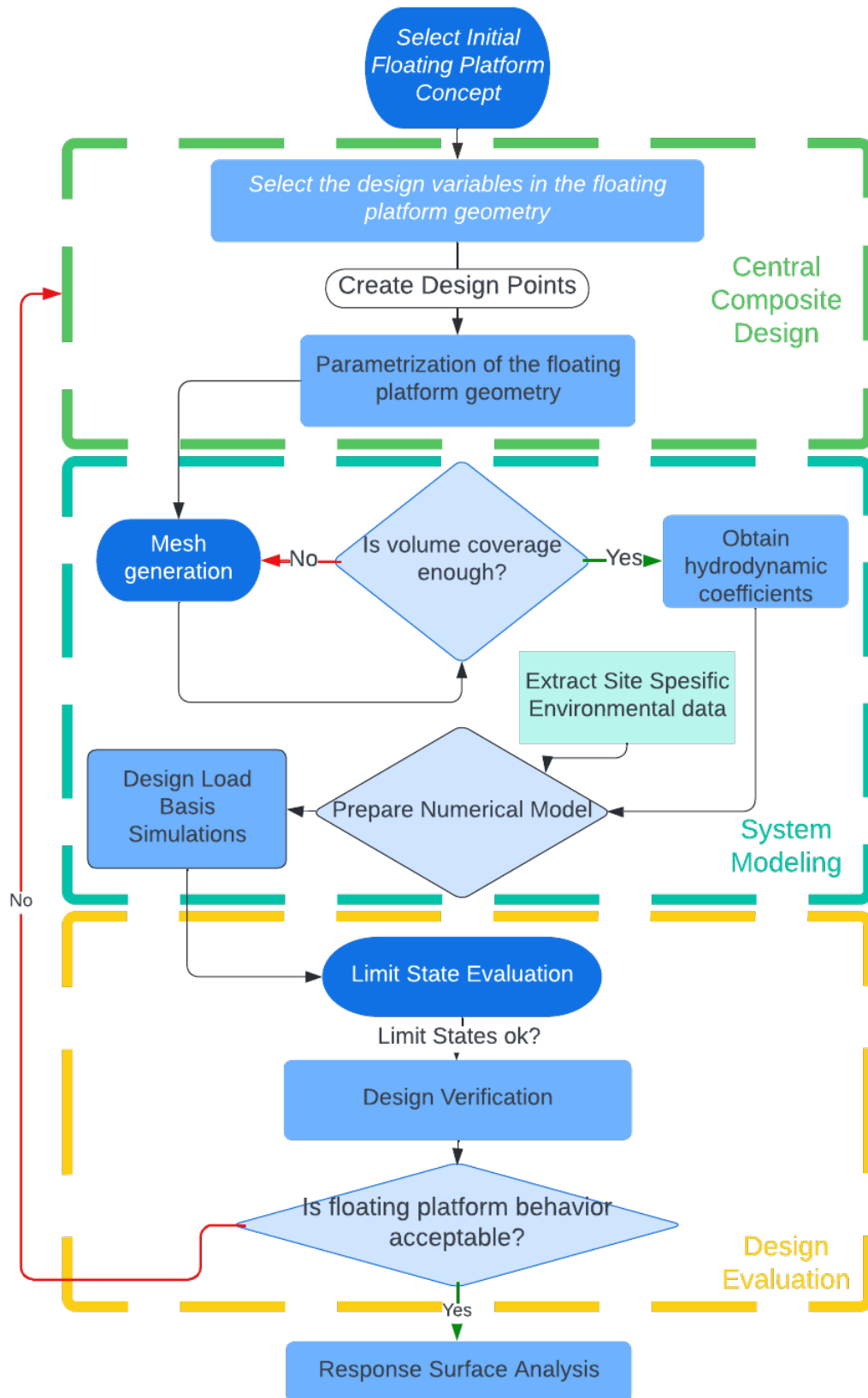


Figure 5.10: Flow diagram with overview of the FWT design evaluation framework

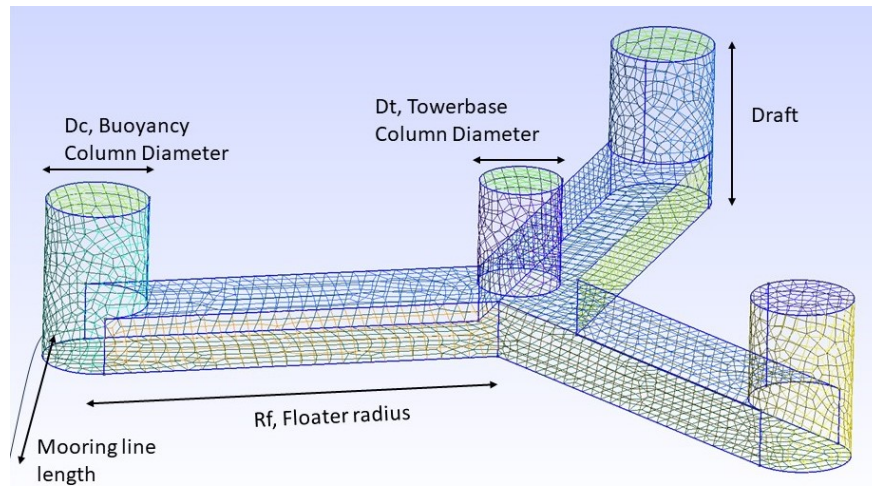


Figure 5.11: Overview of floater geometry and design variables considered in the evaluation framework

5.4.4 Serviceability Limit State Assessment

Evaluation of the serviceability limit states was carried out with Hawc2 time-domain simulations only, following a full IEC61400-1/IEC61400-3 design load basis. The design load basis consists of operational, non-operational, and fault design load cases (DLCs). The simulated time series from all DLCs were statistically post-processed to compute SLS values as well as damage equivalent loads (DELs). The SLS and DEL results were analyzed for tower base bending moments and mooring line tension loads.

5.4.5 SLS evaluation

The SLS criteria for FWTs were reviewed from literature. Blade clearance is one of the more obvious candidates. The minimum value of allowed blade-water clearance is defined according to local regulations of the offshore wind farm area. Marine spatial planning might significantly influence this. Tower blade clearance is also important for the operational safety of the turbine, and tower top acceleration is important in terms of system stability and power production.

5.4.6 FWT design evaluation: summary and conclusions

Hiperwind Deliverable 4.4 (Yildirim and Dimitrov, 2024) presented the implementation and use of a Python-based floating wind turbine (FWT) design evaluation framework. The tool was used to carry out global variance-based design sensitivity analysis on a semisubmersible floater, to explore the effects of design variables on the system response and characteristics. The key findings of the sensitivity analysis present that the buoyancy column diameter has the highest effect on the pitch response, steady-state pitch, and tower fore-aft natural frequencies. The floater radius also has a significant effect on the wave response of the structure in the surge, pitch motion, steady-state pitch, and tower fore-aft natural frequencies.

A second study with the same toolset presented a method for SLS identification and computation where blade tip - water clearance, blade tip - tower clearance, and tower top fore-aft and side-side accelerations are selected, and related load cases are identified. The critical DLCs for

SLS are defined as DLC 1.6 for blade tip - water clearance, DLC 1.3 for the blade tip - tower clearance, and DLC 1.3 and 2.1 for the tower top acceleration. The selected site conditions and the floater configuration can have an effect on defining the critical DLCs.

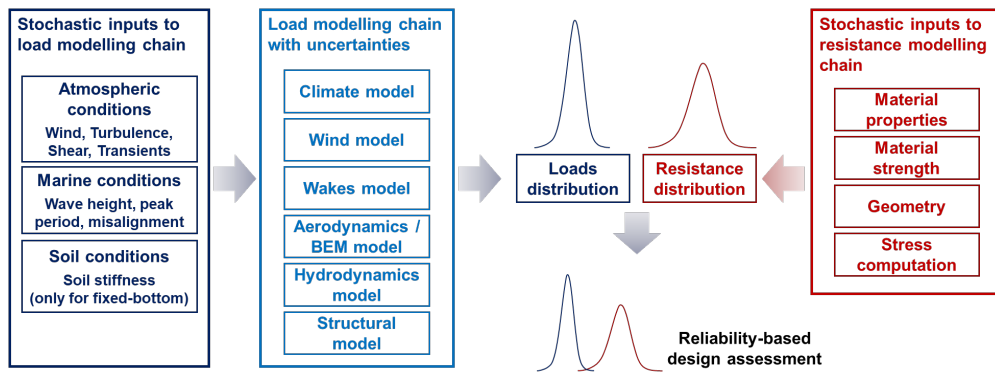


Figure 5.12: Overview of the random variables and uncertainties considered for reliability assessment. Figure reproduced from [Dimitrov et al. \(2024a\)](#).

5.5 Uncertainty model definition for reliability assessment

One of the primary goals of WP4 is to develop and validate models for structural reliability computation, which are used to demonstrate a practical application of probabilistic design. This is done while considering the results from the uncertainty quantification (and reduction) activities that took place in WPs 2 and 3. Here we briefly discuss how the results and insights gained from WPs 1, 2 and 3 are utilized in the reliability assessment, specifically the model choices and uncertainty model. This section is based on ([Dimitrov et al., 2024a](#)) where more information can be found.

We distinguish between three types of stochastic variables included in the reliability assessment problem: 1) environmental random variables constituting a random vector \mathbf{V} , 2) random variables \mathbf{Z} , called system variables, independent from \mathbf{V} , and 3) model uncertainty variables \mathbf{U} . The variables in \mathbf{Z} represent properties which affect the structural behavior such as e.g., material stiffness. Each structure under consideration (e.g., a wind turbine) is considered to represent a single realization from the probability distribution of \mathbf{Z} . On the other hand, the variables in \mathbf{V} are external to the structure and represent conditions that will be continuously changing over the lifetime of the structure, such as environmental parameters. As a result, the distribution of \mathbf{V} needs to be determined and sampled with respect to a short-term reference period. Figure 5.12 shows an overview of the elements of the modelling chain, and the associated uncertainties considered in the reliability analysis activities in WP4. In order to reduce the problem to a manageable extent, the primary focus is on the loading side of the limit state equation. The material resistance is considered probabilistic (included in \mathbf{Z}), but no concrete efforts are made for refining the models or quantifying the uncertainties on this side of the equation. Instead, generic values are taken from literature. As shown in Figure 5.12, the load-related random variables can be broadly grouped in two categories. The first category is the stochastic inputs to the load modelling chain, which contains a combination of aleatory uncertainties (e.g. due to random variation in the environmental conditions \mathbf{V} , and the soil stiffness, which is considered part of \mathbf{Z} because it affects the structural behavior), as well as some epistemic uncertainties due to, e.g., measurement uncertainty. The second category, uncertainties in the modelling chain, comprises only epistemic uncertainties affecting the models that are used (referred to as variables \mathbf{U}).

The subset of the uncertainty variables (from those shown in Figure 5.12) to be used in

reliability computations was determined separately for the FLS and ULS reliability cases. Calculations considering wake-induced effects indicated that wind turbines belonging to the outermost rows with maximum exposure to ambient conditions are subjected to the most significant loading. This applies to both ULS and FLS. Therefore, the FLS calculations are considering a single worst-case-scenario turbine located in the outermost row of the wind farm, without explicitly considering wake model uncertainties. Similarly for the ULS case, the ambient conditions can be considered as a worst-case reference for any wind turbine in the wind farm. The effect of aerodynamics uncertainties was omitted as the calculations indicated that it has relatively small effects. The uncertainty in hydrodynamics was estimated primarily for the fatigue case, where it was found that the material (and system) uncertainties prevail, hence the latter were retained for keeping the overall problem sufficiently simple. Based on these considerations, the final choice of variables in \mathbf{U} and \mathbf{Z} was made. These are outlined further in Sections 5.6 and 5.7, for the ULS and FLS cases respectively.

5.6 Reliability assessment for ULS

The reliability assessment for ULS consists in estimating the probability of failure of the structure due to rare and extreme events. This probability considers several sources of uncertainties: those on the environmental conditions defined by a long-term variability (described by the distributions introduced in section 3.6) and by the short-term variability of wind and waves and those on model parameters such as the yaw misalignment.

These failures can occur under stationary conditions (the incoming wind and wave processes are stationary) or with transient conditions (typically due to the occurrence of a gust). These properties of the random processes have a major impact on the method used to estimate the failure probability. The goal of the project with regards to the ULS reliability assessment is to identify a method to estimate this failure probability with enough accuracy within a reasonable number of calls to the time-consuming simulator.

For a detailed description of the problem, the methods used and the results, we refer to deliverable D4.2 (Cousin et al., 2024).

5.6.1 ULS reliability calculations for stationary conditions

For the stationary case, several approaches has been compared on a toy case: the contour method, a Bayesian neural network, an outcrossing method, and a Sequential Sampling Method (SSM), Gramstad et al. (2020). We identified that only the sequential sampling method is ready to be used on a more realistic case since it provides a probability estimation with few calls to the simulator. A Kriging model is sequentially enriched to predict the parameters of the extreme distribution of loads for a given long-term set of variables. The convergence of the method in returning period is shown in Figure 5.13 where the reference value computed with a brute force Monte Carlo procedure is plotted as dark dashed line.

This method has then been applied to a fixed offshore wind turbine and to a floating case as well. For the fixed case, a IEC 61400 Design Load Basis is carried out to identify the most critical location on the structure which is the von Mises stress of the monopile at mudline, for the DLC61 (extreme turbulent wind in non operating conditions). The SSM enrichment of DoE in parameter space is shown in Figure 5.14.

The annual failure probability at this point is estimated at 2.1×10^{-13} with the sequential method, with a confidence interval of $[0.1 \times 10^{-13}, 7.4 \times 10^{-13}]$. This estimation required 2400 simulations.

The sequential method has also been applied with success on the floating case estimating the annual failure probability due to the von Mises stress at tower bottom at 3.7×10^{-5} with 3250 simulations.

The maximum annual failure probability allowed by the standards (IEC (2019a); DNVGL (2018)) being of 10^{-4} , these analyses reveal that for both cases, the structure can withstand extreme events with sufficiently high reliability. Moreover, with a failure probability way below the 10^{-4} threshold, the studied fixed wind turbine has a very conservative design.

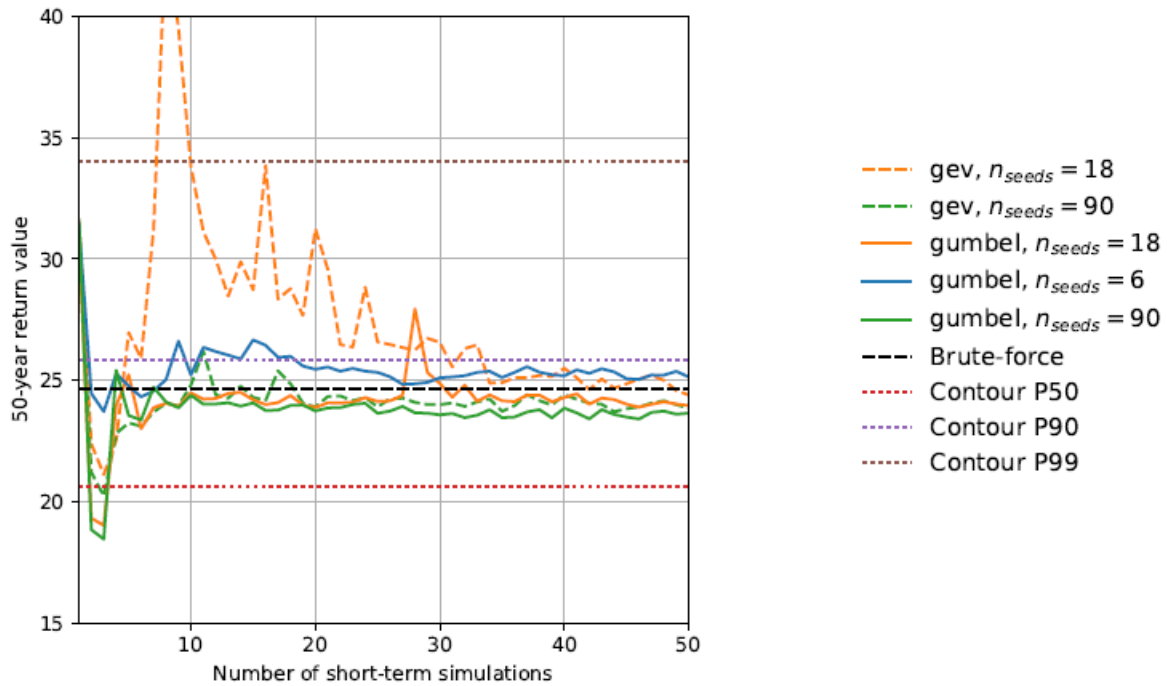


Figure 5.13: . Estimated 50-year return values on a 2D toy problem from sequential sampling, as function of the number of Short Term simulation used to train the GP. Results from brute-force sampling and from a direct sampling contour method are also included. Figure reproduced from Cousin et al. (2024).

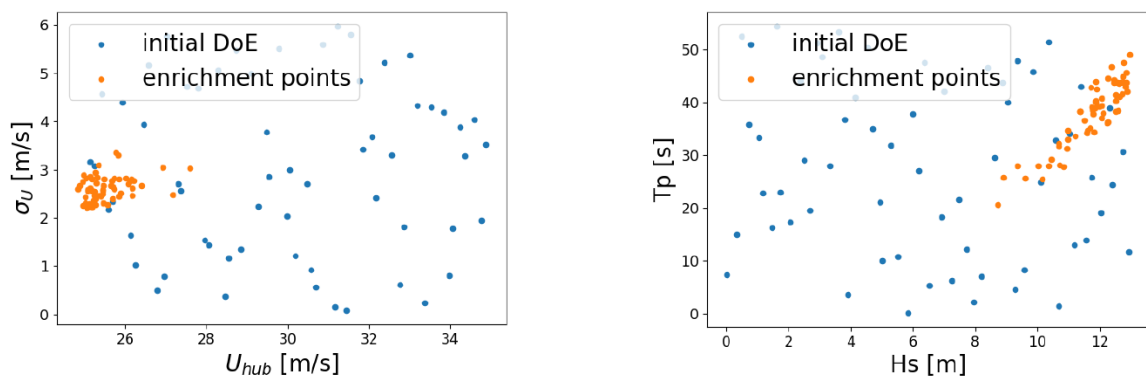


Figure 5.14: . 2D projection of the DoE used in the sequential sampling method. Figure reproduced from Cousin et al. (2024).

5.6.2 ULS reliability calculations for transient conditions

Initially, this study considered a stochastic space, consisting of the gust amplitude, time constant and emergency shutdown timing, along with the other long term parameters (*i.e.* wind speed, turbulence intensity, wave height, wave period, yaw-misalignment, wave-misalignment). The synthetic gusts were generated with the \tanh function as shown in equation 5.4. Where the gust parameters A and T were selected from the corresponding joint distributions given in section 3.5.

$$U(\mathbf{x}, t) = u(\mathbf{x}, t) + \frac{AT}{\pi} \left(1 + \tanh \left(\frac{\pi (t - t_{gust})}{T} \right) \right). \quad (5.4)$$

A series of preliminary Monte-Carlo simulations was carried out to understand the largest drivers for the loads. The study looked at different gust statistics, different ways of generating the turbulence and gusts, whether shutdown should be considered and buckling utilization ratios and different components. Overall, the study showed that the tower and monopile at the Teeside were oversized for the site conditions, (see Figure 5.15).

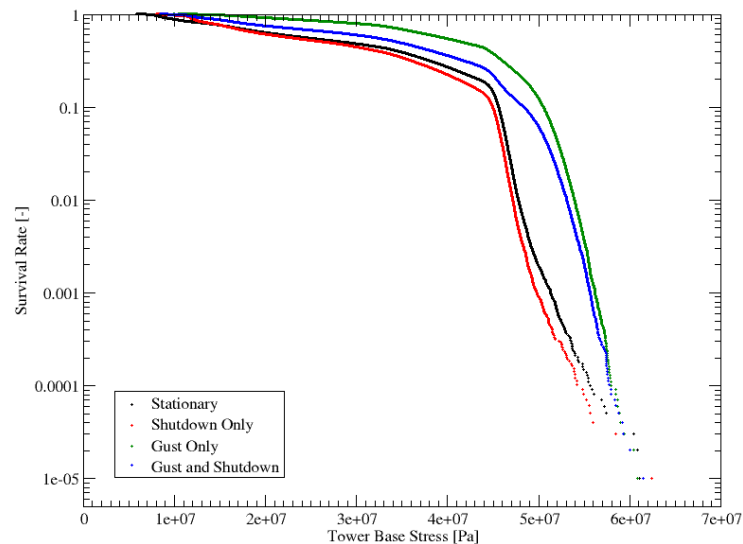


Figure 5.15: Survival plot for maximum tower base Von-Mises stress, based on different Monte-Carlo simulation configurations. Each simulation consisted of 100,000 samples. Figure reproduced from Cousin et al. (2024).

The main driver for the tower base loads was identified by selecting a subset of simulations that produced the highest loads for a range of return periods. Plotting the direction in the standard stochastic space against the distance in the same standard space (*i.e.*, the space defined by a Rosenblatt transform), showed that extreme gust amplitudes were responsible for the largest loads (see figure 5.16).

Since the failure probability is mainly driven by the occurrence of gust events which can be described by few parameters, there is no need to consider the full short-term variation of the wind speed, and classical reliability methods in small dimension can be applied (Bourinet (2018)).

An adaptive Kriging (AK) method using the SUR learning criterion (Duhamel et al. (2023)) is chosen to estimate the failure probability in the transient case considering possible occurrence

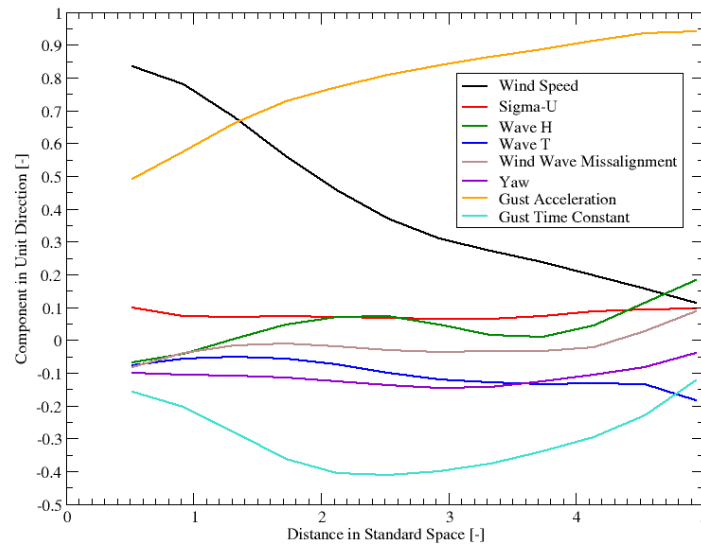


Figure 5.16: The direction in standard space vs. distance in standard space, for the simulations responsible for the largest stress, within the Monte-Carlo simulations. Figure reproduced from Cousin et al. (2024).

of a shutdown and a gust. The method is applied to the fixed wind turbine. The convergence of the AK is illustrated in Figure 5.17 with a reduction of the pseudo bound distance on the failure probability. With 200 simulations, the annual failure probability is estimated at 1.09×10^{-8} .

This work will be the subject of an upcoming publication McWilliam et al. (2025c).

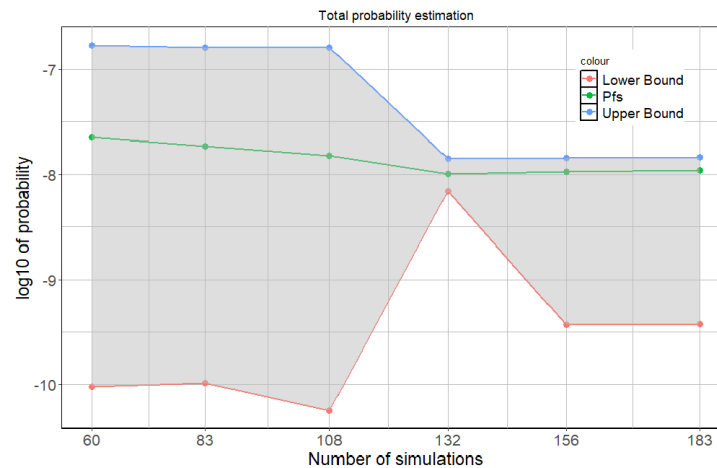


Figure 5.17: . Failure probability estimation with transient input wind along the active learning iterations. Figure reproduced from Cousin et al. (2024).

5.7 Reliability assessment for FLS

Most of this section is developed in the HIPERWIND Deliverable 4.3 report (Fekhari et al., 2024a).

5.7.1 Fatigue reliability assessment problem

As every structural reliability assessment problem, the fatigue reliability assessment problem for WTs can be expressed via a limit state function G . This G -function $G(X, Z)$ depends on the following variables displayed in two independent groups:

- Environmental random variables constituting a random vector X (wind mean speed U , turbulence σ_U , significant wave height H_s , peak wave period T_P , wind direction θ , wave direction α), at the origin of the fatigue loading (alternating stress) ; the joint distribution of the random vector is estimated on a conventional time window of 10 minutes ; for this reference time window one realization of X is sampled;
- Random variables Z , called system variables, independent from X ; they can be split as follows: $\{Z\} = \{D_{CR}\} \cup \{Z'\}$ where D_{CR} stands for the critical damage; the Z variables only appear in the reliability analysis;

Fatigue initiation is a cumulative phenomenon where we count all the cycles of alternating stresses that have occurred over a period of time (for us an assumed lifetime). Assuming linear accumulation (as with the Miner's rule considered for the use case), it can be shown that the accumulated damage for a given Z' -realization is as follows, and consequently named "mean global damage":

$$D_{global} = E_X[d(X, Z')] \quad (5.5)$$

Consequently, the failure probability writes:

$$P(D_{CR} - D_{global} < 0) = P_{Z'}(D_{CR} - E_X[d(X, Z')] < 0) \quad (5.6)$$

5.7.2 Methodology (computational aspects)

The choice of techniques for probabilistic fatigue assessment was based on two considerations: 1) the availability of site-specific environmental data, and 2) the computational efforts required to carry out the analysis. As a result we used a flexible and efficient sampling method, called "kernel-herding", to perform given-data uncertainty propagation for probabilistic fatigue assessment (i.e., directly subsampling from environmental data without inferring a probabilistic parametric model). This sampling method conveniently extracts from a measured dataset a small number of relevant input points (i.e., environmental conditions) in order to use them as simulation inputs. Finally, this method is compatible with the intensive use of high-performance computer facilities, as it uses parallel computing. It is described in detail in Fekhari et al. (2024b). It has been implemented in a Python Package based on the OpenTURNS uncertainty treatment platform and called `otkerneldesign`, available at <https://efekhari27.github.io/otkerneldesign/master/>.

5.7.3 Use case description: numerical simulation model, probabilistic model

The use case for fatigue reliability assessment is the bottom-fixed Teesside offshore wind farm, which has been operated by EDF since 2014. The site consists of 27 SWT2.3-93 wind turbines

Table 5.1: Marginal distributions used for the Z -variables considered for the reliability analysis

Z -variable	Symbol	Marginal distribution	Comment
Soil coefficient	S	Normal ($\mu = 1, \sigma = 0.2$)	Applied to the soil stiffness matrix
Yaw misalignment	θ	Truncated Normal ($\mu = 0, \sigma = 5^\circ, -10^\circ, +10^\circ$)	Deg.
SN curve coefficient	a	Log-normal ($\mu = 1, \sigma = 0.3$)	
Critical damage (Miner's sum at failure)	D_{CR}	Log-normal ($\mu = 1, \sigma = 0.3$)	Cf. (JCSS, 2011)

installed on monopile foundations. There are approximately 5 years of SCADA and met mast data available to the study team, as well as a wave buoy. The reliability assessment is performed at the tower base, where the structural resistance is evaluated in terms of Von Mises stresses in an isotropic material (steel). The Teesside, UK use case fatigue analysis resorts to the DIEGO code. DIEGO (for "Dynamique Intégrée des Éoliennes et Génératrices Offshore") is a code developed by EDF R&D [Milano et al. \(2019\)](#); [Kim et al. \(2022\)](#) to simulate the aero-hydro-servo-elastic behavior of OWTs. It takes the turbulent wind speed field generated by TurbSim [Jonkman and Buhl \(2006\)](#) as input and computes the dynamical behavior of the system (including the multiaxial mechanical stress at different nodes of the structure). Since the wind field generation shows inherent stochasticity, each 10-minute long simulation is repeated with different pseudo-random seeds and one averages the estimated damage over these repetitions. 11 repetitions are considered for Teesside. For the Teesside case, the fatigue reliability assessment is performed at the mudline level, for one WT belonging to the first row (i.e. exposed to the most severe fatigue conditions). Note that a more precise clustering analysis performed on the floating case of the South Brittany wind farm confirmed the conservatism of the first row [Lovera et al. \(2023\)](#). 4 Z -variables are considered for the Teesside offshore wind farm fixed case and their distribution is given in Table 5.1.

5.7.4 Some results

Preliminary evaluations have been performed for the cumulated damage (mean global damage D_{global}), for specific values of the Z' variables, in particular for a case corresponding to pessimistic values of Z' gives a value of D_{global} around 10^{-3} . A distribution analysis of D_{global} shows a central part roughly between 10^{-4} and 10^{-3} . Consequently, failures probabilities are low. Using the reference D_{CR} lognormal distribution, the failure probability P_f evaluated on an anticipated lifetime period of 25 years is about 10^{-12} . This tends to confirm that, as the Teesside wind farm was designed for ULS, FLS is not the dominating failure mode. Note that the failure probability w.r.t. the critical damage has been estimated using FORM, FORM-IS and subset simulation algorithms, which all provide similar results. These simulations were performed after building a surrogate model of the mean cumulative damage at the mudline level of the foundation. P_f is highly sensitive to the D_{CR} distribution assumption. When considering a positive truncated

normal distribution instead, P_f becomes much higher (about 10^{-6}), corresponding to less than 10^{-7} in term of annual probability. However, it remains significantly lower than the annual 10^{-4} probability threshold sometimes considered in the literature. A robustness analysis on the Z distribution parameters confirms that the fatigue reliability is mostly driven by the critical damage D_{CR} . To evaluate the impact of the wake effect within the wind farm, a similar study was repeated by taking the most wake-perturbed metocean distribution inside Teesside's wind farm. The values of failure probability when considering the wake-perturbed conditions appeared to be very close to the ones estimated previously, leading to similar conclusions and showing that the wake effect does not significantly affect the fatigue reliability on the Teesside bottom-fixed case.

5.8 Design utilization study and updates

Since the ULS reliability assessment of the fixed wind turbine revealed a very conservative design, a new approach was proposed to reduce the material cost of the structure. The purpose is to solve an optimization problem aiming at minimizing the mass of the structure while satisfying several constraints. Manufacturability, weldability, natural frequencies, buckling constraints as well as the constraint on the ULS failure probability are considered.

The main difficulty to solve this problem is to estimate the failure probability of the new configurations of the structure which are obtained at each optimization iteration. Indeed, even with the efficient SSM method discussed in 5.6.1, numerous simulations are required.

The optimization is simplified using the fact that, when modifying the thickness of the turbine and monopile, the time series of moments and forces at the mudline are unchanged, as illustrated for example in Figure 5.18.

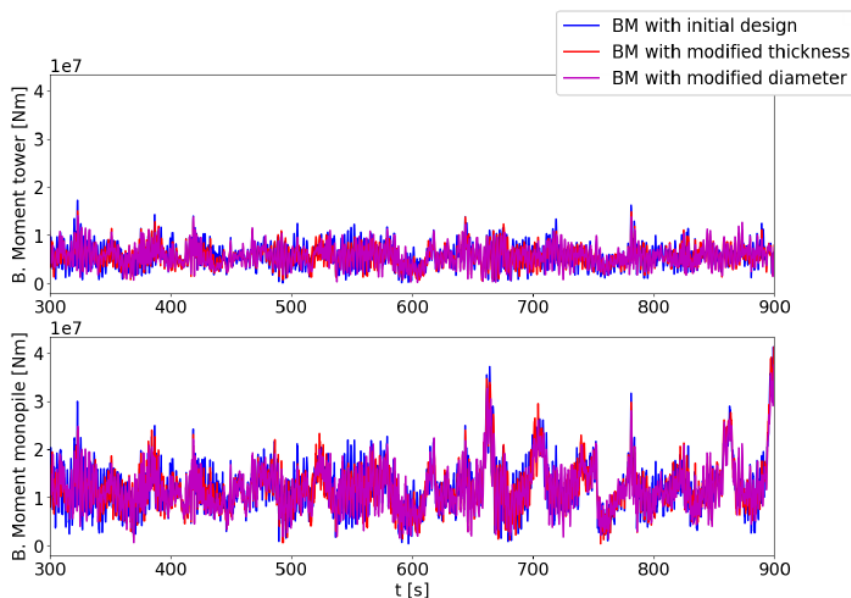


Figure 5.18: Time series of the bending moment for tower base (top) and monopile at mudline (bottom) with mean speed of 35m/s, Turbulence Intensity of 11%, yaw and wind-wave misalignments of 30°, significant wave height of 13 m and wave peak period of 43 s. Figure reprinted from Hiperwind D4.2 report (Cousin et al., 2024).

Assuming this moment preservation is perfectly satisfied, the updated failure probability can be obtained using the outputs of the simulations performed for the initial failure probability estimation. We then succeed to solve the optimisation problem without new simulations and to reduce the total mass of the structure by 21%. An illustration of the difference between the original and updated tower thickness profiles is shown in Figure 5.19, and the mass reduction distribution among the tower, transition piece and monopile foundation is given in Figure 5.20.

This procedure has not been repeated for the floating case since its ULS failure probability is already close to the 10^4 threshold. Moreover, another optimization approach would need to be applied to reduce the mass for this structure since the conservation of the moment and forces with design transformation does not hold here.

This work is discussed in more details in deliverable D4.2 (Cousin et al., 2024).

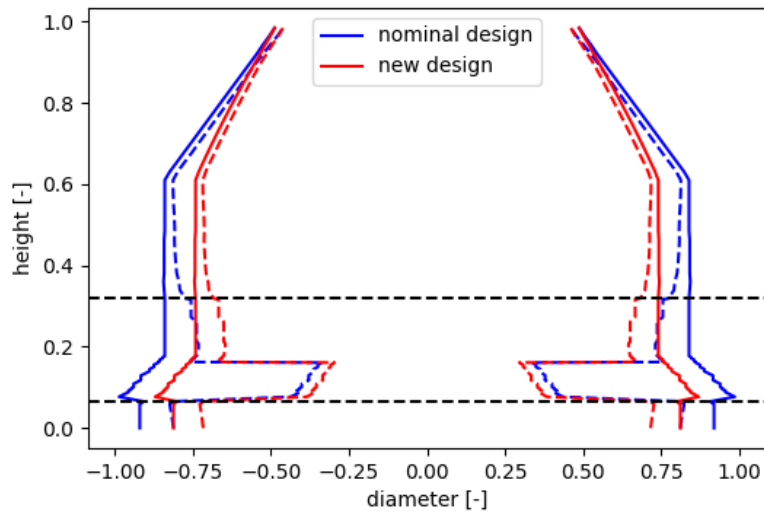


Figure 5.19: Profiles of the nominal design and the new design (with normalized axes). Figure reprinted from Hiperwind D4.2 report (Cousin et al., 2024).

Part of the structure	mass (initial design) [tons]	mass (new design) [tons]
Monopile	71.62	55.76
MP+TP	226.52	176.34
Transition piece	139.62	108.69
Tower	139.31	114.10
Total	577.08	454.89

Figure 5.20: Mass reduction for each part of the structure. Figure reprinted from Hiperwind D4.2 report (Cousin et al., 2024).

6 Component reliability assessment (WP5 outcomes)

6.1 Load-based bearing degradation model

This section is based on the work reported in Deliverables 5.1 and 5.4 ([Remigius et al., 2023](#); [Abrahamsen et al., 2024b](#)).

The component reliability study of the Hiperwind project has focused on the evaluation of the reliability of bearings of wind turbines by combining the ISO 281 standard "Roller bearings - Dynamic load rating and rating life" [ISO281 \(2007\)](#) and the IEC 61400-1 ed. 4 standard "Wind energy generation systems Part 1 - Design requirements" [IEC \(2020\)](#) specifying the typical Design Load Cases (DLC) of wind turbines. The focus has been on the main bearings of the Teesside offshore wind farm holding 27 Siemens Wind Turbines of the type SWT 2.3 - 93 with a power rating of 2.3 MW and a rotor diameter of 93 m [Moros et al. \(2024\)](#). The turbines are placed 1.5 km from shore on the east coast of the United Kingdom near the river Tees and the water depth ranges between 13-16 meters. The Teesside wind farm started operation in 2014 and is operated by EDF. The original plan of the Hiperwind project was to investigate the lifetime models of several drive train components of the SWT 2.3 - 93 turbines of Teesside, but the lack of details of the gearbox of the turbine resulted in focusing on the main bearing, because public information could be found from second-hand spare part trading websites like SparesInMotion. The main bearing is well represented by a FAG 230/800 double-row spherical roller bearing and lubricated with a grease similar to Klüberplex BEM 41-301. The size of this bearing is given by an outer diameter of 1.2 m, a width of 0.3 m and it can support a shaft with a diameter of 0.8 m. The weight is approximately 1 metric ton. The final argument for investigating the main bearing is also that it is a very expensive part to replace because a jack-up vessel will be needed to dismount the turbine rotor before the main bearing can be replaced and the turbine rotor put back on the turbine. Thus even though the main bearing failures are not reported as a major issue in the literature [Moros et al. \(2024\)](#), the impact will be significant and predictions of the expected time of failures can be used as input to the maintenance planning.

A Physics-based lifetime model of the FAG 230/800 main bearing of SWT 2.3 - 93 turbine was formulated from the ISO 281 [ISO281 \(2007\)](#), the technical report TR 1281 [TR1281-2 \(2008\)](#), the ISO 16281 [ISO16281 \(2008\)](#) and the technical note TPI 176 from Schaeffler [Schaeffler \(2013\)](#) as well as the catalog properties of the bearing and the grease (see Hiperwind deliverable report D5.1 [Remigius et al. \(2023\)](#) and D5.3 [Abrahamsen et al. \(2024a\)](#)). The purpose of the model is to be able to evaluate the impact of the wind environmental conditions in terms of wind speed distribution and turbulence on the main bearing lifetime. Secondly, the model should incorporate the so-called lifetime modification factor for system approach $a_{i,ISO}$, which takes into account the viscosity and the cleanliness of the grease. The challenge of the last part is that the viscosity will change with the operation temperature and a thermal model was therefore created to estimate the operation temperature from the friction heating of the bearing [Abrahamsen et al. \(2024a\)](#). The loads of the main bearing were evaluated in 600 second time series using an aeroelastic model of the SWT 2.3 - 93 turbine as implemented in the aeroelastic Hawc2 code of DTU [Larsen and Hansen \(2023\)](#); [Remigius et al. \(2023\)](#); [Abrahamsen et al. \(2024b\)](#). It was then possible to create contour maps of the main bearing basic lifetime for a large parameter space of wind speeds and turbulence intensities. This parameter map was used to create a position contour map of the main bearing lifetime of the Teesside offshore wind turbines.

The basic lifetime L_{10h} of bearings according to ISO 281 [ISO281 \(2007\)](#) is given as

$$L_{10h} = \frac{10^6 \text{ rev}}{60 \text{ sec/min} \cdot n} \left(\frac{C}{P_{eq}} \right)^b \quad (6.1)$$

where n is the rotation speed, C the dynamic rating of the bearing, $b = 10/3$ is the exponent for roller bearings and P_{eq} is the equivalent load of bearing. The unit of L_{10h} is in hours, but one can specify the lifetime in the unit of years L_{10y} . The L_{10h} lifetime is the operation time after which 10 % of an ensemble of identical bearings will have failed when operated under similar conditions. One can scale the L_{10h} lifetime to a failure fraction n % and also other operational conditions by imposing the modification factor for reliability a_1 and the modification factor for system approach a_{iso} whereby the modified lifetime L_{nm} is given as

$$L_{nm} = a_1 a_{iso} L_{10} \quad (6.2)$$

where the modification factor for reliability a_1 is given by a Weibull distribution as described in Hiperwind deliverables 5.1, 5.2 and 5.4. The life modification factor for the system approach depends on the grease viscosity at the operation temperature as well as the cleanliness of the grease (see Hiperwind deliverable 5.1 [Remigius et al. \(2023\)](#), 5.3 [Abrahamsen et al. \(2024a\)](#) and 5.4 [Abrahamsen et al. \(2024b\)](#)).

The instantaneous load of the bearing $P(t)$ is obtained from the axial $F_a(t)$ and radial $F_r(t)$ load of the bearing by applying manufacturer-specific factors X and Y

$$P(t) = X F_r(t) + Y F_a(t) \quad (6.3)$$

where $(X,Y) = (1, 3.07)$ if $F_a(t)/F_r(t) < 0.22$ and $(X,Y) = (0.67, 4.57)$ if $F_a(t)/F_r(t) > 0.22$ for the FAG 230/800 bearing.

The equivalent load P_{eq} of the main bearing is then found from the accumulated damage of time-varying loads $P(t)$, rotation speed $n(t)$ and the a_{iso} factor as

$$P_{eq} = \left(\frac{\int_{t=0}^{t_i} \frac{(P(t))^b n(t) dt}{a_{iso}(t)}}{\int_{t=0}^{t_i} \frac{n(t) dt}{a_{iso}(t)}} \right)^{1/b} \quad (6.4)$$

where the integral over time often corresponds to a 600 seconds aeroelastic time series of the turbine loads. If the a_{iso} can be considered constant during the time series then it can be omitted from the integral.

The methodology outlined above can be combined with aeroelastic simulations, because the radial $F_r(t)$ and axial $F_a(t)$ bearing loads can be determined by solving the equation of motion of the turbine given specific inflow wind conditions. From the IEC 61400-1 [IEC \(2020\)](#) standard, the Normal Turbulence Model associated with Design Load Case 1.2 (Normal operation) provides a correlation between turbulence intensity TI and the wind speed u as

$$TI = \frac{\sigma_1}{u} = \frac{I_{ref}(0.75u + b)}{u} \quad (6.5)$$

where the reference turbulence intensity is denoted I_{ref} and the b-value is assumed constant at $b = 5.6 \text{ m/s}$. A parameter space of wind speeds $u = 4 - 26 \text{ m/s}$ and reference turbulence

intensity $I_{ref} = 0.10 - 0.18$ was created with a separation between points of 1 m/s and 0.002 in order to investigate the resulting main bearing lifetime. Additional 3 wind directions and 12 seeds were added per point of the parameter space, resulting in 33948 aeroelastic simulations holding a 600-second time series.

Figure 6.1 shows the equivalent load of the main bearing of the SWT 2.3 - 93 turbine as a function of the wind speed u and the turbulence intensity TI . The dashed lines indicate a constant reference intensity and the IEC turbulence classes A, B and C with $I_{ref} = 0.16, 0.14$ and 0.12 are shown along with the boundaries of the parameter space of $I_{ref} = 0.10$ and 0.18 . Detailed analysis of aeroelastic simulations has shown that the variation of the equivalent load of Figure 6.1 is mainly caused by the axial load of the bearing since the radial load is basically the gravitational force of the rotor mass resting on the main bearing. Thus the equivalent main bearing load is basically a replica of the turbine thrust curve as a function of the wind speed u , and this is why it peaks at the rated wind speed of the turbine. An interesting feature of Figure 6.1 is that the main bearing load at the rated wind speed $u = 10\text{ m/s}$ is decreasing as the turbulence intensity is increased from $TI = 0.14$ to 0.25 . This effect can be explained by the fact that the thrust curve will peak at the rated wind speed and increasing the fluctuations of the wind will cause less time spent at the peak of the thrust curve. A resulting effect of the main bearing load when calculated into the basic lifetime is shown in Figure 6.2 and it is seen that the lowest L_{10y} lifetime is obtained around the rated wind speed of the turbine.

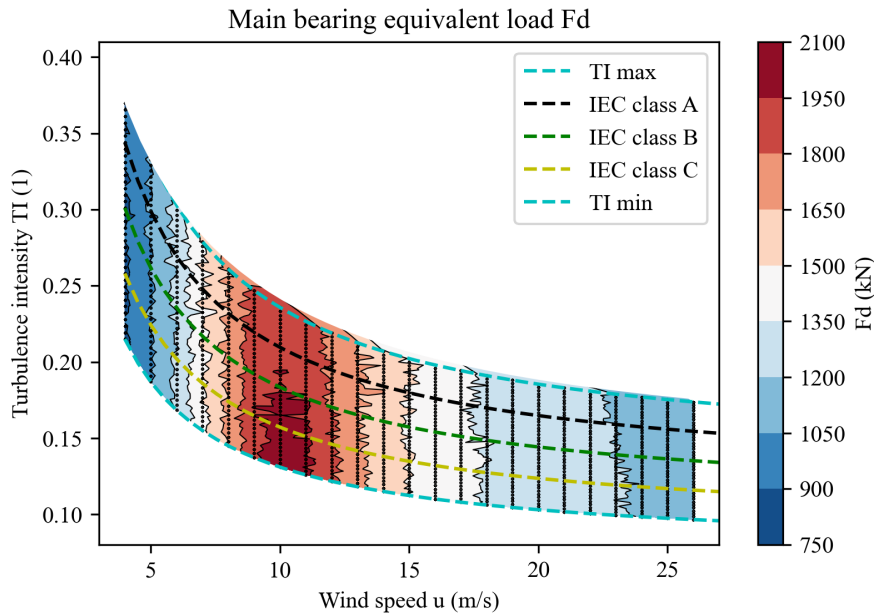


Figure 6.1: Main bearing equivalent load P_{eq} of the aeroelastic simulation representing $u = 4-26$ m/s and $I_{ref} = 0.1-0.18$. The IEC turbulence wind classes A, B and C with $I_{ref} = 0.16, 0.14$ and 0.12 are shown by dashed lines.

The ten-minute wind speed distribution as given by a Rayleigh distribution can then be specified as

$$f(u) = \frac{u}{s^2} e^{-u^2/2s^2} \quad (6.6)$$

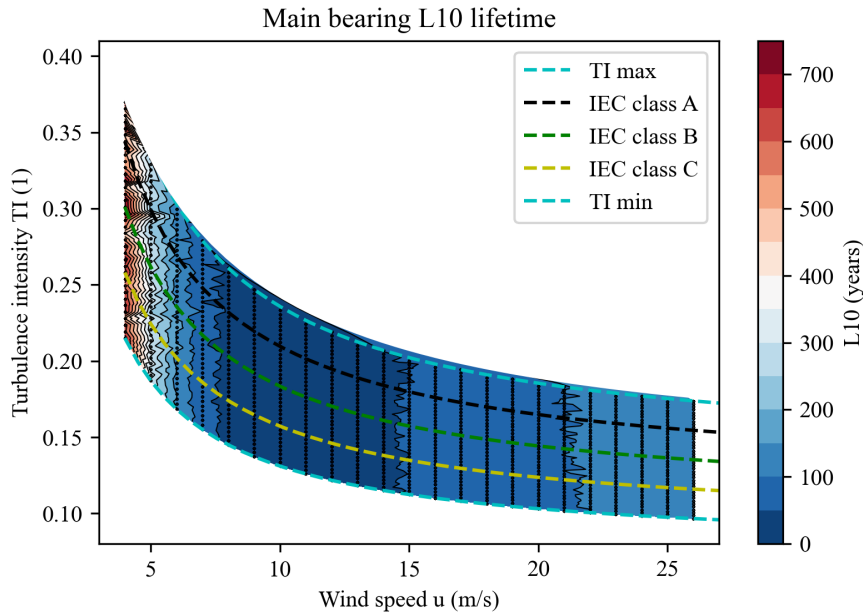


Figure 6.2: Main bearing basic lifetime L_{10y} of the aeroelastic simulation representing $u = 4-26$ m/s and $I_{ref} = 0.1-0.18$. The IEC turbulence wind classes A, B and C with $I_{ref} = 0.16, 0.14$ and 0.12 are shown by dashed lines.

where u is the ten-minute mean wind speed and the annual average wind speed v_{ave} is related to the scale parameter $s = \sqrt{\frac{2}{\pi}}V_{ave}$. The Rayleigh distribution can then be used to assign the statistical weight of the L_{10y} lifetimes along a line of constant I_{ref} shown in Figure 6.2 and the resulting main bearing lifetime map is shown in Figure 6.3 as function of the annual average wind speed v_{ave} and the reference turbulence intensity I_{ref} . The original IEC design wind class IIB of the SWT 2.3 - 93 turbine is indicated as a dot and the average wind speed of the Teesside wind farm is indicated as a vertical dashed line. Thus it is seen that the basic lifetime of the main bearing is expected to increase from approximately 25 to 27 years by moving the turbine from design conditions and to the Teesside annual wind speed if the reference turbulence intensity is maintained at $I_{ref} = 0.16$. If however the reference turbulence intensity is lowered to $I_{ref} = 0.10$ then the basic lifetime of the main bearing will remain at around 25 years. Details of the basic main bearing lifetime map can be found in Hiperwind deliverable D5.1 Remigius et al. (2023) and D5.4 Abrahamsen et al. (2024b).

6.2 Wind farm reliability map

This section is based on the work reported in Deliverable 5.4 (Abrahamsen et al., 2024b).

One application of the main bearing basic lifetime map of Figure 6.3 is to determine the local wind environment of the wind turbines of the Teesside wind farm and then to investigate the spread of the basic main bearing lifetime across the wind farm. This was done by fitting the annual average wind speed v_{ave} and the reference turbulence intensities I_{ref} to the SCADA data of the 27 Teesside wind turbine and Figure 6.4 shown the resulting L_{10y} map of the wind farm Abrahamsen et al. (2024b). It is observed that wind turbines at the corner of the wind farm WT9 and WT19 are predicted to have the shortest basic lifetime L_{10y} in the order of 24 years,

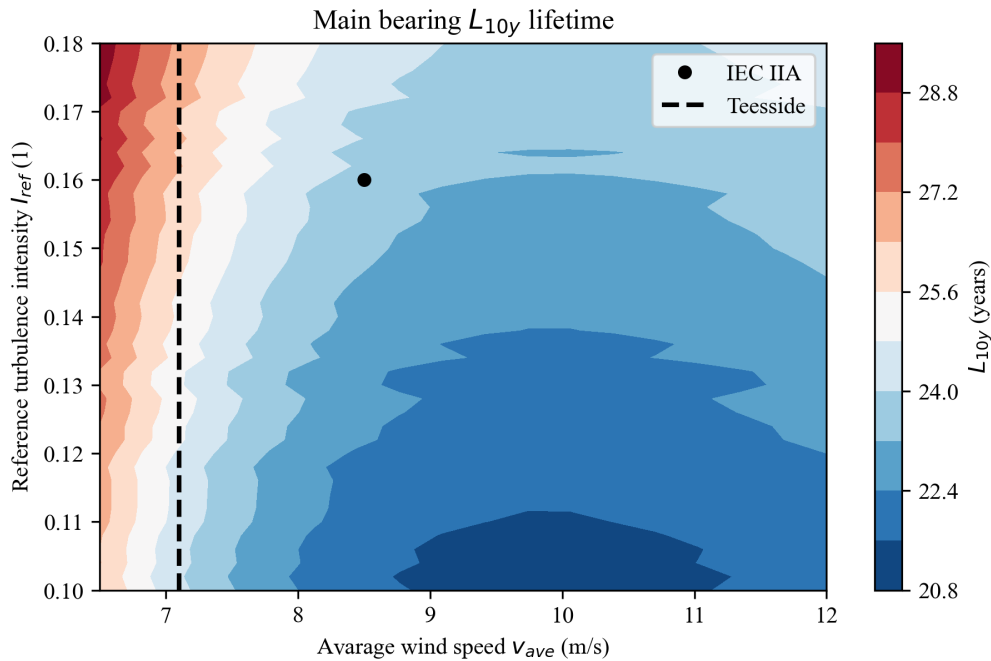


Figure 6.3: Main bearing basic lifetime L_{10y} shown as function of the annual average wind speed v_{ave} of the Rayleigh distribution and the reference turbulence intensity I_{ref} . The IEC design wind class IIB of the SWT 2.3 - 93 turbines is shown as a dot and the annual average wind speed $v_{ave} = 7.1$ m/s of the Teesside offshore wind farm is shown as a vertical dashed line [Moros et al. \(2024\)](#).

the turbines at the outer edges have a predicted lifetime of approximately 25-26 years and the middle row of turbines of the farm have a basic predicted lifetime of approximately 27 years. Turbine WT13 is peaking up with a predicted basic lifetime of about 29 years, but this is believed to be an artifact of a measurement error, which could not be resolved from the analysis. The appearance of the map can be explained by the outer turbine being exposed to non-disturbed wind with higher mean velocity and therefore longer periods with high thrust forces, whereas the turbines in the center row will experience the wakes from the turbines at the edges which results in generally lower wind speeds. From the Teesside lifetime map one can determine the failure probability of the main bearings using the modification factor for reliability a_1 of the ISO 281 standard [ISO281 \(2007\)](#). Figure 6.5 shows the cumulative failure probability for all assets in the wind farm as function of the basic main bearing lifetime. It is seen that one out of the 27 main bearings is expected to fail after approximately 12-15 years, two out of 27 after 19-24 years, and 3 out of 27 after 25-32 years. Thus this prediction provided an input to the scheduling of maintenance of the Teesside wind farm under the condition that the L_{10y} is the correct lifetime prediction and that no corrections for the operational state of the main bearings are needed. The latter is discussed as part of the validation activity.

6.3 Validation of the bearing degradation model

This section is based on the work reported in Deliverable 5.3 ([Abrahamsen et al., 2024a](#)).

A major challenge identified as part of the Hiperwind work on the physics-based main bearing lifetime model is how to determine the so-called modification factor for system approach a_{iso} of

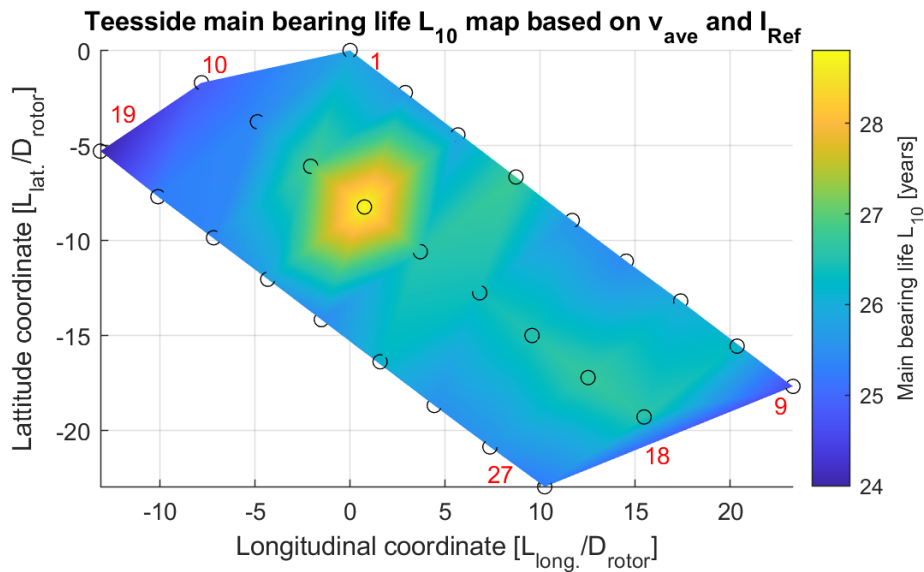


Figure 6.4: Main bearing basic lifetime L_{10y} shown for the position of the wind turbines WT1 to WT27 (red numbers) of the Teesside wind farm in units of the turbine rotor diameter.

the ISO 281 standard [ISO281 \(2007\)](#) from the aeroelastic simulation of the turbine loads [IEC \(2020\)](#). The a_{iso} factor takes into account the viscosity of the grease used to lubricate the main bearing, and since this is highly temperature dependent, then one will need to provide some assumptions about the operating temperature of the main bearing. In the Hiperwind project a thermal model of the main bearing was proposed based on the frictional heat generation of the bearing as described by Schaeffler in the note TPI 176 [Schaeffler \(2013\)](#). It was assumed that the heat capacity of the bearing could be neglected in the thermal model, which described the expected main bearing temperature as given by the balance between the heat dissipated in the bearing and the heat transport through the bearing housing as well as the main shaft going to the hub flange. Thus, the model is not able to describe the time delay of a temperature increase if the heat input is changed, but assumes that the bearing is attaining the long-term equilibrium temperature instantaneously. This simplification allows one to solve for the main bearing temperature directly from the many factors of the ISO 281 needed to estimate the a_{iso} factor [ISO281 \(2007\)](#). The Hiperwind thermal model was validated against the measured main bearing temperatures observed in 2019 and Figure 6.6 shows the comparison between the main bearing temperatures measured in 2019 and the predicted main bearing temperature from the physics-based model of Hiperwind [Abrahamsen et al. \(2024b\)](#). It is observed that there is a reasonably good agreement in terms of the range of the operation temperatures, and this provides confidence that the lifetime estimation, including the a_{iso} , should be correct. By assuming that the grease of the main bearing can be considered completely clean with a contamination factor of $e_C = 1.0$, the lowest a_{iso} factor found was approximately 8. This indicates the modified lifetime of the main bearing must be multiplied by this factor of 8, whereby the predicted modified lifetime of the main bearings becomes approximately 200 years. This is considerably longer than the 25-

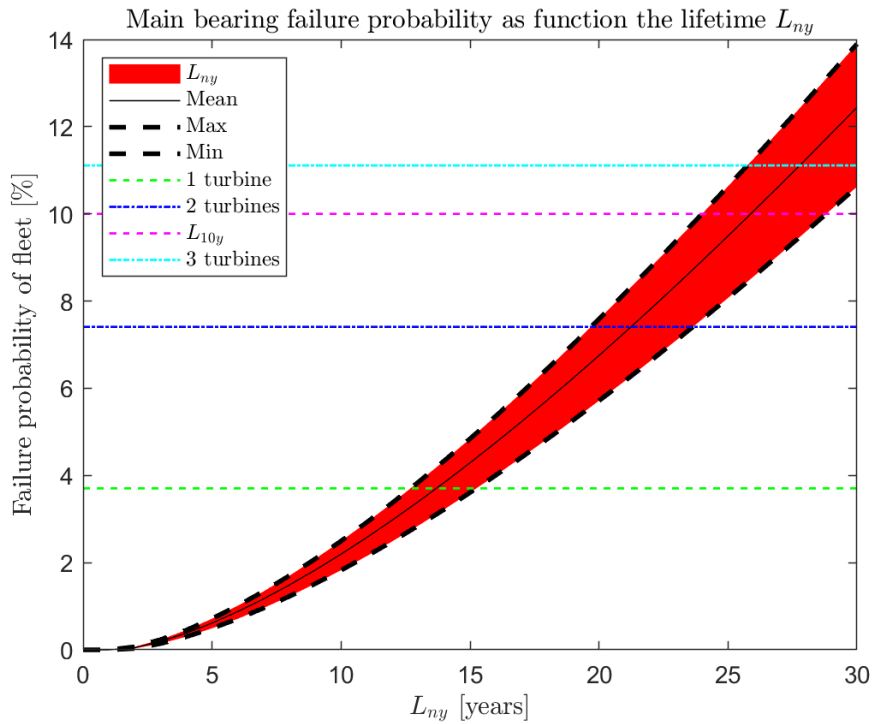


Figure 6.5: Failure probability of the main bearing of the Teesside wind farm as function of the basic lifetime L_{10y} . The horizontal dashed lines indicate a failure rate corresponding to 1, 2, and 3 out of the 27 turbines experiencing bearing failure.

year design lifetime of the SWT 2.3 - 93 turbine and matches the current failure statistics of the Teesside wind farm, where no main bearings have failed until now. It will, however, be interesting to follow the failure statics of the Teesside wind farm to determine if the basic or the modified lifetime will be closest to the observed lifetimes. The challenges of estimating the time-varying a_{iso} factor for wind turbines is discussed in the Hiperwind deliverable D5.4 [Abrahamsen et al. \(2024b\)](#) and is considered a challenge for the wind community when applying a physics-based lifetime model of the main bearings of the turbines.

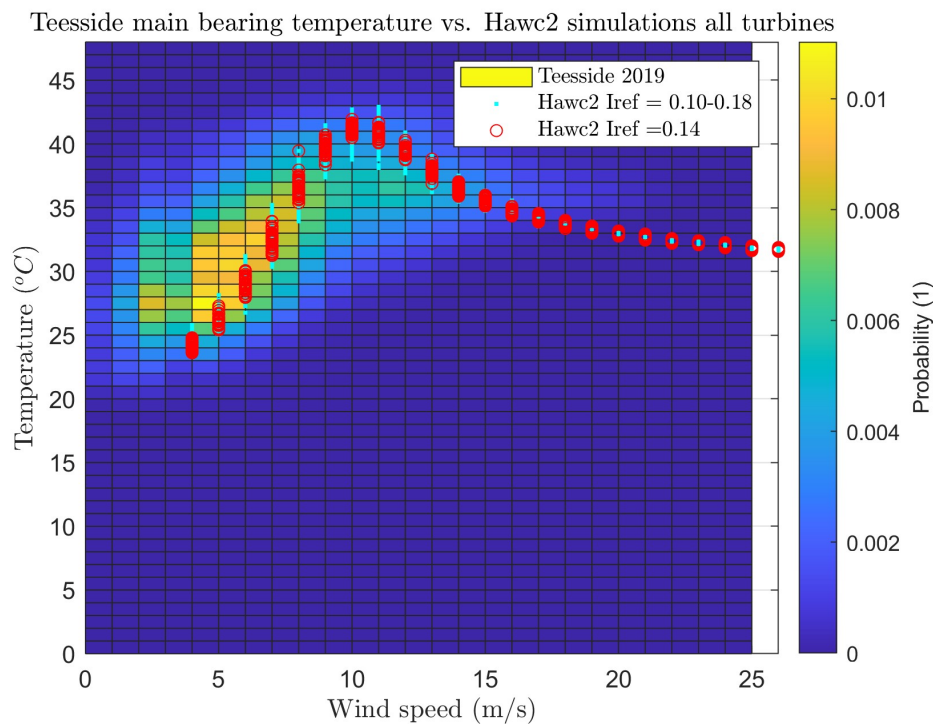


Figure 6.6: Probability of observing a main bearing temperature in the SCADA data of the 27 SWT 2.3 - 93 turbines of the Teesside offshore wind farm in 2019 as a function of the wind speed measured at the turbines. The prediction of the main bearing temperature from the physics-based thermal model is shown in the red open circles for the reference turbulence intensities of $I_{ref} = 0.14$ corresponding to the Teesside offshore wind farm. The predicted main bearing temperatures of the range of reference turbulence intensities $I_{ref} = 0.10 - 0.18$ is also shown for comparison.

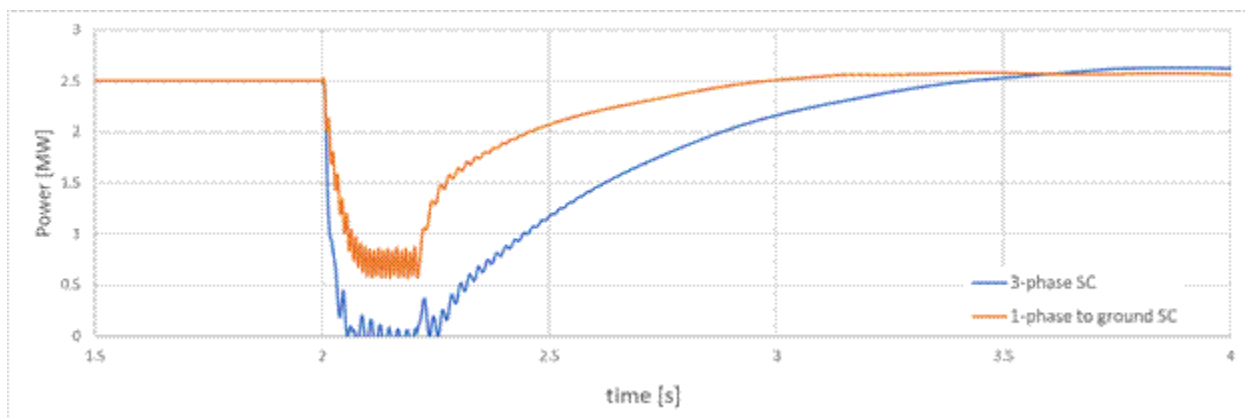


Figure 6.7: Active power generation during Grid voltage sag at 12m/s wind speed. The response has been simulated using an IEC-2.5MW type 4 wind turbine model in powerFactory.

6.4 Reliability of electrical components and effect of grid events on mechanical loads

This section summarizes the outcomes of Deliverable 5.2 (Paz et al. (2023)). The objective of D5.2 was to develop a framework to simulate grid perturbations and their impacts on the turbines mechanical and electrical components.

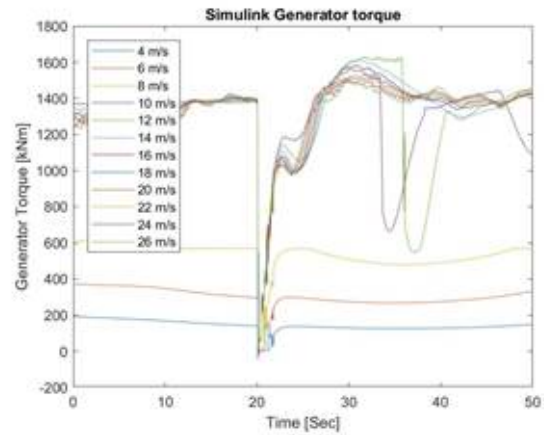
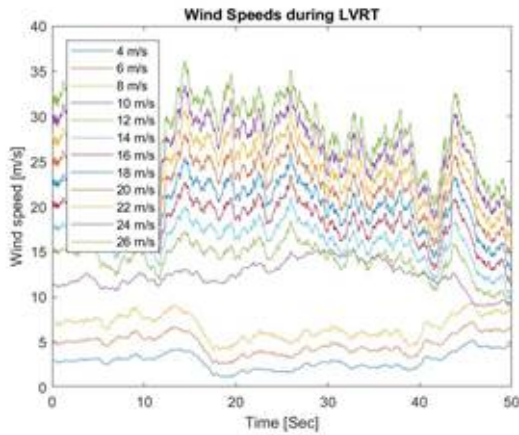
6.4.1 Method overview

An integrated model was developed to combine modeling of the electrical components, using Simulink (The MathWorks Inc. (2024)), with aeroelastic simulations, using DTU's HAWC2 (Larsen and Hansen (2023)). Such a combined approach allowed for estimating the loads on the mechanical components induced by grid perturbations and to quantify the lifetime reduction induced by these events.

A more detailed presentation of the simulation is given in the D5.2 report (Paz et al., 2023).

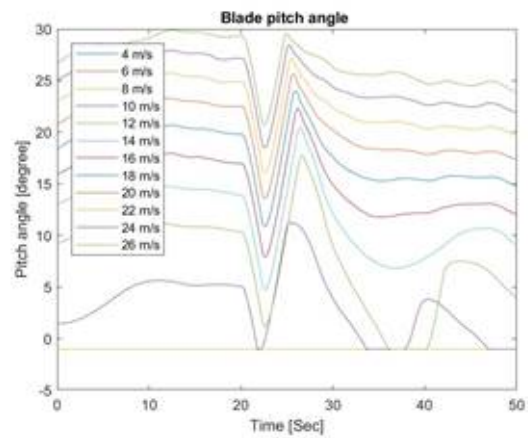
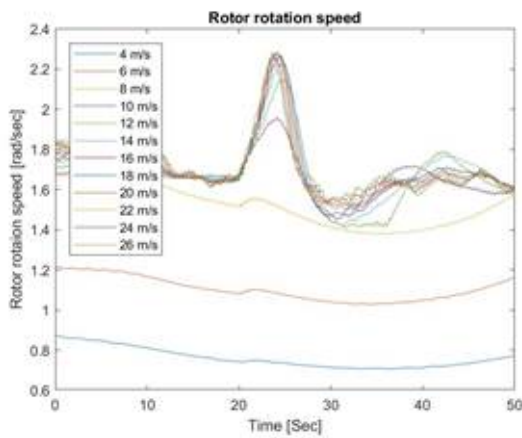
6.4.2 Results

The simulation framework was used to study the impact of a low voltage ride through (LVRT) event on the load on the main bearing for the Teesside's turbine model. During such events the turbine must keep producing power as illustrated on figure 6.7. Multiple wind-conditions were simulated, covering the entire operating range of the Teesside's turbine model. Simulation results for the main turbines operating channels are shown on figure 6.8. The simulations demonstrate that even during LVRT events, the turbine can manage torque and rotational speeds, thereby limiting excessive wear on critical components such as the main bearing. The control strategies implemented in the modeled system help prevent over-speed and manage torque effectively, contributing to the turbine's long-term reliability. Additionally, such time domain simulations reveal how LVRT affects turbine components, including rotor speed and blade pitch angle. These simulations form the basis for the fatigue evaluation of mechanical components, providing insights into the long-term impacts of grid disturbances.



(a) Wind speed time series for seed no. 3 out of 7 and with a turbulence intensity of $I_{ref} = 0.16$ for different average wind speeds as given by the labels

(b) Generator torque of seed no. 3 corresponding to the wind speed time series given by the labels and with a LVRT of approximately 1-3 second starting at $t = 20s$.



(c) Turbine rotor rotation speed is observed to increase after the Low Voltage Ride Through and return to the initial level after 10 seconds.

(d) Blade pitch angle response to the Low Voltage Ride Through.

Figure 6.8: HAWC2 response time series during Low Voltage Ride Through (LVRT) at $t = 20s$ under *DLC 2.4* with a turbulence intensity of $I_{ref} = 0.16$. Only 50 seconds out of 100 seconds are shown to highlight the features after the LVRT, whereas all 100 second time series are used for the fatigue evaluation.

6.4.3 Conclusion

The results from this study suggest that while LVRT introduces additional stress on wind turbine components, modern control systems and protection hardware like break-choppers are effective in mitigating its impact. The integrated mechanical and electrical model developed for this study highlights how LVRT events contribute to increased loads, especially on the drive train and bearings. However, based on the simulations, these loads remain within acceptable limits, ensuring compliance with grid codes and operational safety margins.

The Teesside case study provides valuable insights into how integrated frameworks could predict and mitigate the impact of grid disturbances, extending component lifespan and reducing maintenance costs. Future work could focus on expanding the analysis to include other drive train components like the gearbox, using more detailed turbine-specific data.

7 Impact assessment and optimizations (WP6 outcomes)

7.1 Optimization of O&M scheduling

An advanced O&M optimization tool is developed in deliverable 6.1 (Charousset and Gruet (2024)) in the HIPERWIND project. It aims to minimize the cost for replacing the major components for offshore wind and the revenue loss due to the downtime caused by MCR (Major Component Replacement) through short- and long-term optimization of the maintenance scheduling.

7.1.1 Framework of the optimization

The cost and revenue loss caused by MCR is strongly related to the failure scenarios, the market price scenarios, and the weather scenarios that impact the site accessibility and the power generation. In this O&M optimization tool, we have accounted for these scenarios as follows:

- The statistical models for weather time series generation are variations of Auto-Regressive Moving Average models (ARMA) that takes into account both the seasonality and the correlation between weather variables thanks to complementary neural network models. A statistical criteria was used to select 200 different year-long time series that would represent the variability due to the stochastic nature of weather variables.
- The pan4res model was used to simulate the behavior of the European electricity system on the years 2018, 2025, 2030, 2035, 2040, 2045, and 2050 at country and hour resolution. We then obtained marginal costs time series for each European country. Plan4res is a stochastic model accounting for meteorological scenarios. A total of 37 marginal costs scenarios were used in the optimization.
- Reliability models for wind turbine components were used to simulate the failure scenarios through the life time of the wind farm. In total, 1000 failure scenarios were generated with each scenario consisting of a sequence of numbers representing the failed components through the life time of the wind farm. After analysis of the patterns, these 1000 scenarios were reduced to 104 unique scenarios with different probability.

7.1.2 Formulation of the optimization problem

The optimization problem is formulated into a two-stage optimization problem with different horizon and time granularity.

In the first stage, a short-term optimization problem is performed to find the optimal schedule for a given year and a given number of components to be replaced. The output is a cost matrix with the dimensions of the number of years in the life time of the wind farm (e.g. 25 years) and the maximum number of components to be replaced (e.g. up to 5 gearboxes in one year). The horizon is one year, and the time granularity is one day.

In the second stage, a long-term optimization is performed to find the optimal number of components to be replaced through the life time of the wind farm based on the simulated failure scenarios through the life time of the wind farm and the cost matrix from the first-stage optimization. The horizon is the life time of the wind farm, and the time granularity is one year.

7.1.3 Numerical implementation

The short-term optimization was solved with a Monte-Carlo optimisation conducted on all weather and market price scenarios through the life time of the wind farm and all possible number of

components to be replaced in one year. For each optimization problem corresponding to a combination of scenarios, a mixed integer linear programming was implemented.

Two different approaches can be used to solve the long-term optimization problem:

- Deterministic programming approach: solve the deterministic problem on each of the failure scenarios, and then compute the average;
- Stochastic dynamic programming approach: Solve the stochastic problem on a scenario tree

7.2 O&M optimization for value

The developed O&M optimization tool was demonstrated by one offshore wind farm in the UK. The full study is reported in Hiperwind D6.3 ([Charousset et al., 2024](#)), with a brief extract below.

The short-term and long-term optimization problems were solved together to quantify the impact of the optimization of O&M on the cost and revenue of the wind farm throughout its life time. Though the proposed optimization framework can be applied to account for multiple types of wind turbine components, only one type of wind turbine component (gearbox) is considered in the case study. Gearbox replacement requires specialized heavy-lift jack-up vessels, and it takes about one to two weeks for one gearbox to be replaced.

Three cases were considered in the short-term optimization. The first case features a variable electricity price based on the price scenarios to simulate the market price. The second case considers a fixed electricity price to simulate the context of CfD (Contract of Difference) in the UK. The purpose of the third case is to provide a relatively realistic short-term schedule but without considering any revenue loss in the cost function. In the comparison, the third case is referred to as “non-optimized” in terms of revenue loss.

The comparison of the market price case and the non-optimized case shows that the short-term optimized scheduling may lead to more downtime and sometimes more energy loss, but always less revenue loss. This may be explained by placing the gearbox replacement in the time period with a low-wind speed and/or a low electricity price. The comparison of the CfD price case and the non-optimized case shows that the short-term optimized scheduling always leads to less downtime and less energy loss, and consequently less revenue loss. This reflects the fact that the revenue is solely influenced by the wind speed but not by the electricity price that is fixed. In order to reduce the revenue loss, the gearbox replacement is placed at the low-wind time period.

Three cases were also considered for the long-term O&M, including one reference case, one recalculated reference case, and one optimized case. Both the reference case and the recalculated reference case do not involve any optimization. The reference case features replacing a fixed number of gearboxes for several years and may increase the number of replaced gearboxes after a few years. The recalculated reference case adapts the reference case to reflect the variation in the number of failed gearbox throughout the life time of the wind farm. The optimized case was obtained by performing the long-term optimization based on the gearbox failure scenarios and the short-term optimization results. The optimal long-term scheduling or decision making was determined by using stochastic optimization based on the scenario tree created out of the probabilised scenarios.

Figure 7.1 shows the average revenue loss throughout the life time of the wind farm for 104 failure scenarios. Market price case was used in the short-term optimization. It shows that the

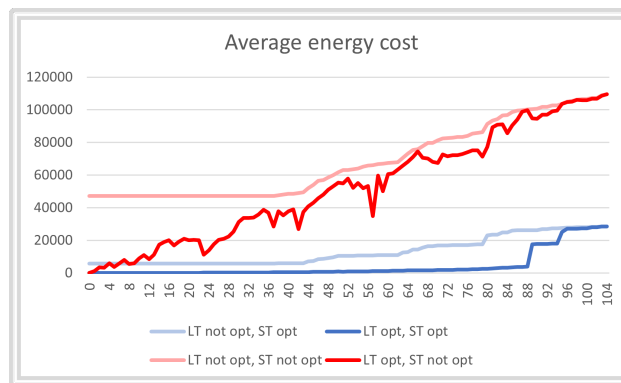


Figure 7.1: The average revenue loss throughout the life time of the wind farm for the 104 failure scenarios. Market price case was used in the short-term optimization.

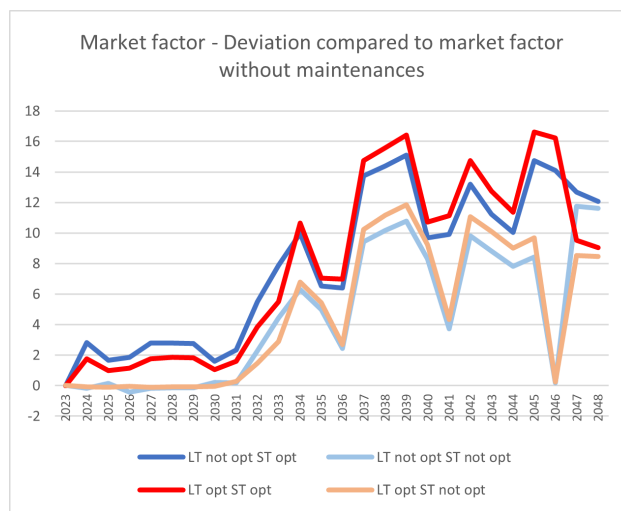


Figure 7.2: Increase in the market value factor throughout the life time of the wind farm for the 104 failure scenarios. Market price case was used in the short-term optimization.

short-term optimization can significantly reduce the revenue loss for all failure scenarios regardless of the long-term scheduling is optimal or not. The optimized long-term scheduling can generally further reduce the average revenue loss, but the change shows a strong variation with the failure scenario and whether the short-term scheduling is optimized.

Figure 7.2 shows the increase in the average market value factor throughout the life time of the wind farm for the 104 failure scenarios with market price case used in the short-term optimization. It shows that while the short-term optimization always increases the market value factor, the long-term optimization only increases the market value factor from 2034 to 2047.

7.3 LCOE modelling tool and Hiperwind impact assessment

This section summarizes the outcomes of Deliverable 6.2 ([Jacquet, 2024](#)). The objective of Deliverable 6.2 was to determine the impact of the technologies developed in HIPERWIND on the Levelized Cost of Energy (LCOE). Inputs for this deliverable were provided by work package 4 (mass reduction of the structural components) and work deliverable 6.1 (optimized maintenance schedule).

7.3.1 Method overview

A modular framework for LCOE calculation was developed with the objective of providing enough granularity to assess the specific impact of a technology improvement (e.g., reduction of the mass of a component) while considering the value chain in its globality. In this architecture, the CAPEX is modelled as the sum of three main components, namely the turbine, balance of plant (BoP) and owner costs. Each of the categories is broken down in sub-components for more granularity. Similarly, OPEX is defined as the sum of the operation costs, assumed to be proportional to the wind farm annual energy production (AEP), and the maintenance costs. For the maintenance cost, several activities are defined, each one associated with a given probability of occurrence and costs (including material and vessel). Monte-Carlo simulation is used to define the number of activities to perform during a year, given their probability of occurrence. The resulting cost is the sum of the individual activity costs.

A more detailed description of the LCOE model and its component is given in [Jacquet \(2024\)](#).

7.3.2 Cost reductions from HIPERWIND improvements

The mass reductions for the tower ($\approx 18\%$) and foundation ($\approx 25\%$) provided by work package 4 ([Cousin et al. \(2024\)](#)) can easily be converted to reductions in cost, considering that, for structural steel components, eighty percent of the cost arises from the material mass. Considering the contributions of these two components to the turbine and BoP costs, this results in **4.32%** reduction of the overall CAPEX. Such a result fits within the targeted range for CAPEX reduction that was estimated at the beginning of the project ([4%, 6%]).

The optimized maintenance schedule from deliverable 6.1 ([Charousset and Gruet \(2024\)](#)) allows for a 14% reduction of the repair time needed for gearbox replacement. This directly impacts the vessel costs, and, thus, the maintenance costs. Generalizing this finding to all major components replacement, this translates into a reduction of the OPEX for the Teesside wind farm of **7.48%**. The OPEX reduction, therefore also fits within the targeted range ([5% – 10%]). Reduction of the turbine downtime also impact the wind farm annual energy production. The gain is estimated to be approximately **0.3%**. The fact that this gain is small in comparison with the downtime reduction from deliverable 6.1 is explained by the fact that major component replacement only have a limited contribution to the overall availability losses. The latter are essentially caused by minor maintenance activities for which no optimization was performed in the context of HIPERWIND.

7.3.3 LCOE results

The LCOE is calculated for the Teesside wind farm, both with (optimized case) and without (baseline case) considering the HIPERWIND improvements. Results are summarized in the table

Table 7.1: Results for LCOE calculation for the Teesside wind farm both for the baseline and optimized case.

	Baseline	Optimized	Δ_{rel}
	\$/MWh		%
CAPEX	136.1	130.20	-4.32%
Turbine	48.75	47.32	-2.9%
BoP	83.86	79.39	-5.3%
Owner's costs	3.49	3.49	0%
OPEX	64.5	60.9	-6.8%
Operation	8.37	8.37	0%
Maintenance	56.08	51.72	-7.8%
Total	200.55	190.29	-5.12%

7.3.3 and shown on the figures 7.3 and 7.4 for the baseline and optimized cases respectively. The LCOE reduction is found to be 5.12% for the Teesside wind farm.

LCOE is also calculated for a virtual wind farm of $75 \times 8MW$ turbines. The latter, inspired by the work of NREL (Stehly and Duffy (2021)), is chosen to be more representative of the wind farm that were installed over the past years and to highlight the dependency of LCOE to design choices that are not part of the HIPERWIND scope. The turbine rating, for instance, was found to have a significant influence on the OPEX. Indeed, a smaller rating requires more turbines to be installed in order to reach a fixed farm output, inducing a larger number of maintenance activities and increased costs. The interest rate was also adjusted for the LCOE calculation of the virtual wind farm to be representative of the current state of the market ($\approx 6\%$), compared to the Teesside wind farm that was simulated using an interest rate representative of the early 2010s ($\approx 12\%$). Results for the virtual wind farm are summarized in the table 7.2, and show on the figures 7.5 and 7.6 for the baseline and optimized cases respectively. For this scenario, the LCOE reduction is found to be 10.36%, which exceeds the initial target of 9% set at the beginning of the project.

Considering several scenarios for LCOE calculation highlights the dependency of the metric to parameters that are not directly within the scope of HIPERWIND. The wind farm design (turbine rating) and the cost of capital are key parameters that drastically influence the LCOE of a given project. The consequence is that, for the case of the Teesside wind farm, the LCOE reduction is estimated to approximately 5%, which is lower than the target set at the beginning of the project, even though the intermediate targets are met for both the CAPEX and OPEX reduction. Conversely, applying the same cost reductions to the virtual wind farm ultimately makes the LCOE drop by more than 10%, which exceeds the project target.

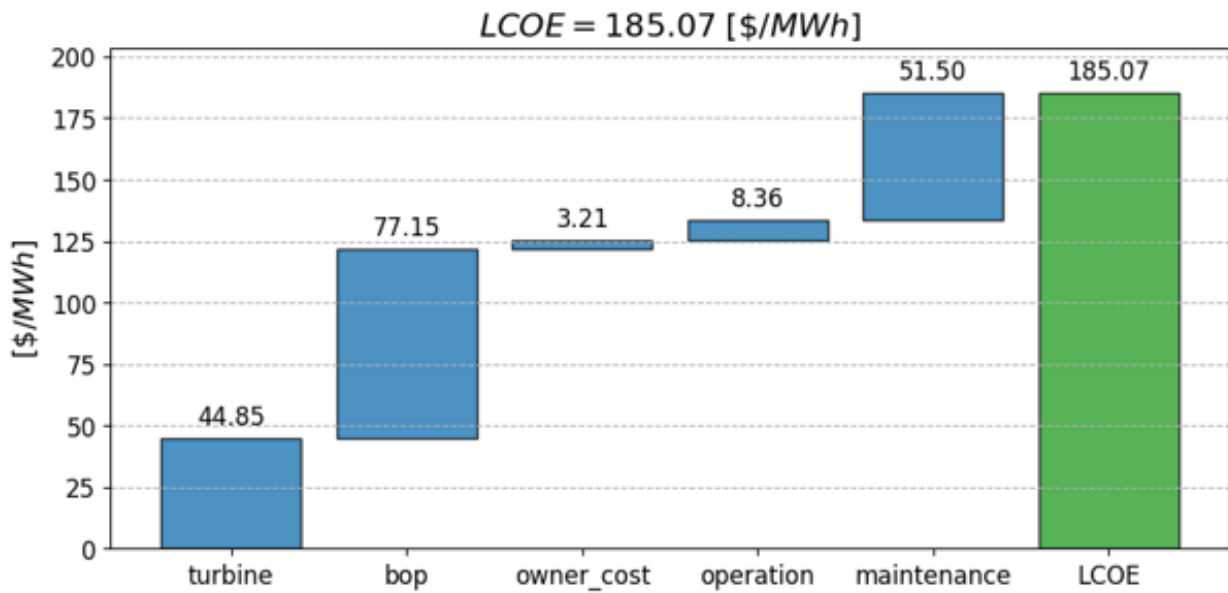


Figure 7.3: LCOE results for the Teeside wind farm without considering HIPERWIND improvements (baseline case)

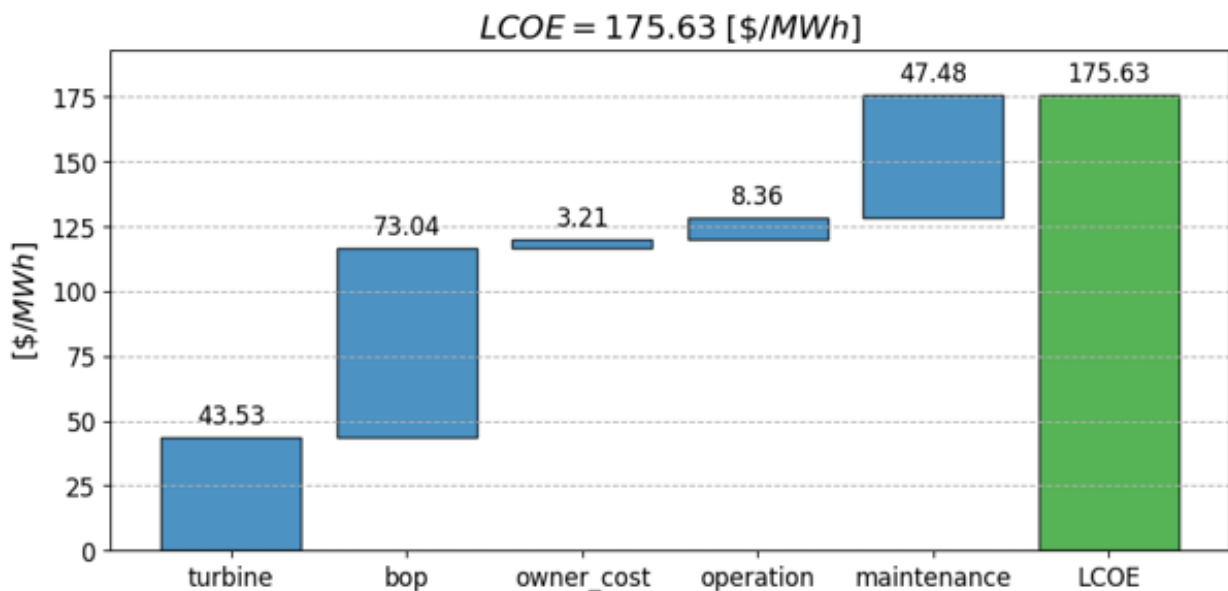


Figure 7.4: LCOE results for the Teeside wind farm considering all HIPERWIND improvements (optimized case)

	Baseline	Optimized	Δ_{rel}
	\$/MWh		%
CAPEX	64.19	61.25	-4.6%
Turbine	23.00	22.26	-3.2%
BoP	39.55	37.35	-5.6%
Owner's costs	1.65	1.64	-0.3%
OPEX	28.43	21.78	-23.4%
Operation	8.41	8.3	-0.3%
Maintenance	20.03	13.40	-33.1%
Total	92.62	830.3	-10.36%

Table 7.2: Results for LCOE calculation for the virtual wind farm both for the baseline and optimized case.

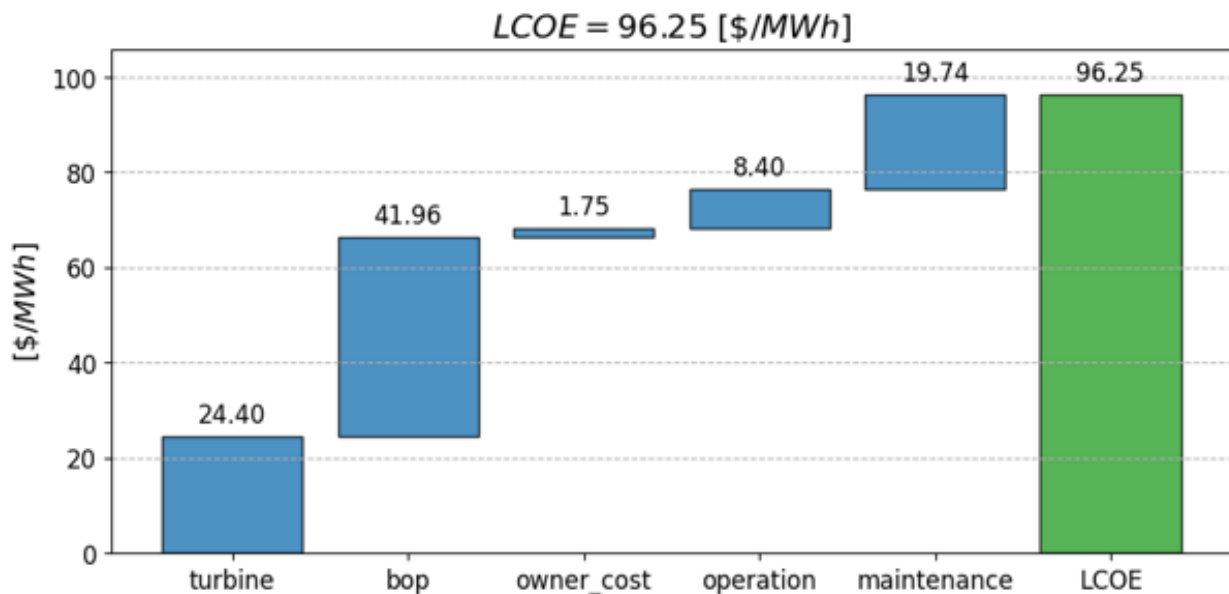


Figure 7.5: LCOE results for the virtual wind farm without considering HIPERWIND improvements (baseline case)

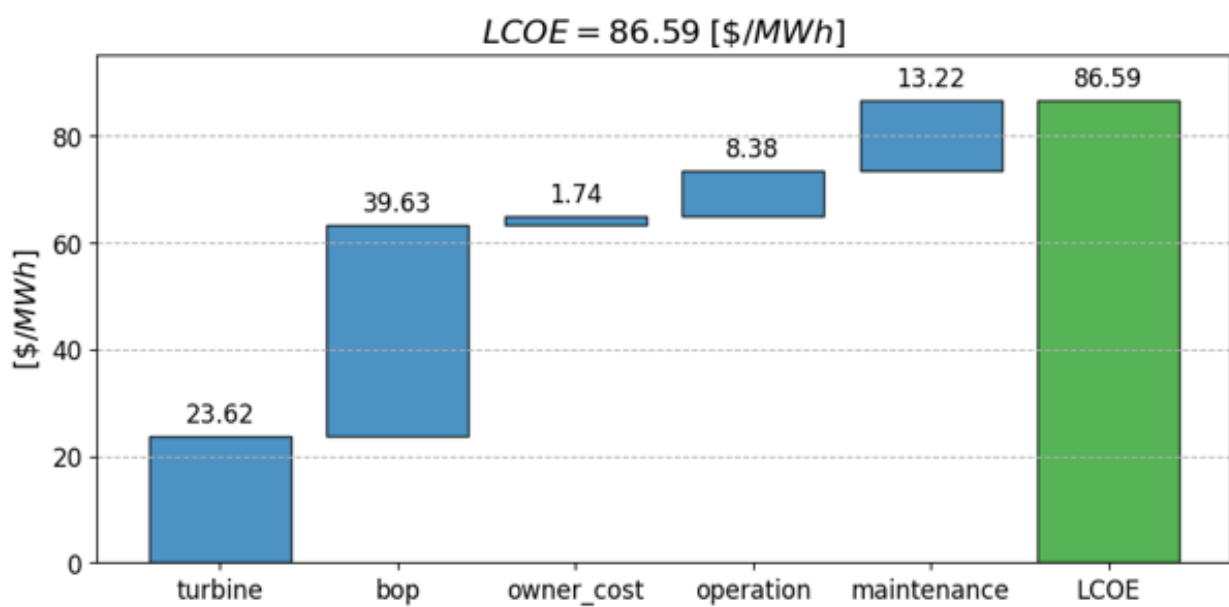


Figure 7.6: LCOE results for the virtual wind farm considering all HIPERWIND improvements (optimized case)

8 Conclusions

Below is a brief summary of the primary conclusions from the project:

- We showed practical examples of design under uncertainty
- Along the way, we obtained a number of useful scientific results, model chain improvements, and software tools
- Understanding uncertainties leads to design improvements
- An integrated design approach is critical for efficient design
- A significant LCOE reduction was achieved (but cost of capital is a major external factor).

We have also identified several areas where further work is necessary:

- Understanding uncertainties in structural/material properties
- Full-scale Reliability-Based Design Optimization (RBDO) needs further efficiency improvements in order to become practical
- Ensuring others can use the Hiperwind results (dissemination and tool releases).

Acknowledgements

This work is a part of the Highly advanced Probabilistic design and Enhanced Reliability methods for the high-value, cost-efficient offshore WIND (HIPERWIND) project, which has received funding from the European Union's Horizon 2020 Research and Innovation Programme under Grant Agreement No. 101006689. The support is greatly appreciated. The authors gratefully acknowledge the computational and data resources provided on the Sophia HPC Cluster at the Technical University of Denmark, DOI: 10.57940/FAFC-6M81 .

References

- A. B. Abrahamsen, S. Dou, A. Zeghidour, N. Berranah, and C. Jacquet. Hiperwind deliverable report d5.3 - physics-based component model validation. Technical report, H2020 HIPERWIND project (Grant agreement No 101006689), 2024a.
- A. B. Abrahamsen, S. Dou, A. Zeghidour, N. Berranah, C. Jacquet, X. Zhang, and D. Remigius. Hiperwind deliverable report d5.4 - development and implementation of probabilistic and uncertainty quantification methods for reliability sensitivity analysis. Technical report, H2020 HIPERWIND project (Grant agreement No 101006689), 2024b.
- C. Allen, A. Viscelli, H. Dagher, A. Goupee, E. Gaertner, N. Abbas, M. Hall, and G. Barter. Definition of the UMaine VoltturnUS-S Reference Platform Developed for the IEA Wind 15-Megawatt Offshore Reference Wind Turbine. Technical Report NREL/TP-5000-76773, 1660012, MainId:9434, National Renewable Energy Laboratory, July 2020. URL <https://www.osti.gov/servlets/purl/1660012/>.
- S. Arai. Forces On And Flows Around a Horizontal Rectangular Cylinder Submerged In Regular Waves. In *Proceedings of the International Ocean and Polar Engineering Conference*, pages ISOPE-I-93-257, 06 1993.
- E. Ardillon, M. Bakhoday-Paskyabi, A. Cousin, N. Dimitrov, M. Dupoirion, S. Eldevik, E. Fekhari, C. Ferreira, M. Guiton, B. Jézéquel, P.-A. Joulin, A. Lovera, L. Mayol, and M. M. Penchah. Hiperwind deliverable report D3.2 - turbine loading and wake model uncertainty. Technical report, H2020 HIPERWIND project (Grant agreement No 101006689), 2022. URL https://www.hiperwind.eu/-/media/sites/hiperwind/publications/hiperwind_d3-2_v2.pdf.
- M. Bakhoday-Paskyabi. Impact of swell waves on atmospheric surface turbulence: wave-turbulence decomposition methods. *Wind Energy Science*, 9, 2024.
- M. Bakhoday-Paskyabi and M. Flügge. Predictive capability of wrf cycling 3dvar: Lidar assimilation at fino1. *Journal of Physics: Conference Series*, 2021.
- M. Bakhoday-Paskyabi, H. Bui, and M. M. Penchah. Hiperwind deliverable report D2.1 - atmospheric-wave multi-scale flow modelling. Deliverable d2.1, H2020 HIPERWIND project (Grant agreement No 101006689), May 2022a. URL https://www.hiperwind.eu/-/media/sites/hiperwind/publications/hiperwind_d2-1_final.pdf.
- M. Bakhoday-Paskyabi, M. Krutova, H. Bui, and X. Ning. Multiscale simulation of offshore wind variability during frontal passage: Brief implication on turbines' wakes and load. *Journal of Physics: Conference Series*, 2362, 2022b.

- X. Barthelemy, M. Banner, W. Peirson, F. Fedele, M. Allis, and F. Dias. On a unified breaking onset threshold for gravity waves in deep and intermediate depth water. *Journal of Fluid Mechanics*, 841:463–488, 04 2018. doi: 10.1017/jfm.2018.93.
- M. Bastankhah and F. Porté-Agel. A new analytical model for wind-turbine wakes. *Renew. Energy*, 70:116–123, 2014.
- M. Benoit, O. Gramstad, Øystein Lande, C. Peyrard, and F. Robaux. Hiperwind deliverable report D2.2 - wave field characterization and associated uncertainties. Deliverable d2.2, H2020 HIPERWIND project (Grant agreement No 101006689), February 2023. URL https://www.hiperwind.eu/-/media/sites/hiperwind/publications/hiperwind_d2-2_report.pdf.
- J. Bleeg. A graph neural network surrogate model for the prediction of turbine interaction loss. In *Journal of Physics: Conference Series*, volume 1618, page 062054. IOP Publishing, 2020. doi: 10.1088/1742-6596/1618/6/062054.
- F. Blondel and M. Cathelain. A new Gaussian-based analytical wake model for wind turbines considering ambient turbulence intensities and thrust coefficient effects. *J. Wind Eng. Ind. Aerodyn.*, 177:275–292, 2018.
- F. Blondel and M. Cathelain. An alternative form of the super-Gaussian wind turbine wake model. *Wind Energy Sci.*, 5(3):1225–1236, 2020.
- F. Blondel, P.-A. Joulin, and C. L. Guern. Towards vortex-based wind turbine design using gpus and wake accommodation. *Journal of Physics: Conference Series*, 2767(5):052016, jun 2024. doi: 10.1088/1742-6596/2767/5/052016. URL <https://dx.doi.org/10.1088/1742-6596/2767/5/052016>.
- J.-M. Bourinet. *Reliability analysis and optimal design under uncertainty-Focus on adaptive surrogate-based approaches*. PhD thesis, Université Clermont Auvergne, 2018.
- H. Bui, M. B. Paskyabi, and M. M. Penchah. Implementation of a simple actuator disk for large-eddy simulation in the weather research and forecasting model (wrf-sadles v1.2) for wind turbine wake simulation. *Geoscientific Model Development*, 17, 2024.
- M. Capaldo, M. Guiton, G. Huwart, E. Julan, N. Krasimirov Dimitrov, T. Kim, A. Lovera, and C. Peyrard. Design brief of HIPERWIND offshore wind turbine cases: bottom fixed 10MW and floating 15MW. Technical report, EDF ; DTU ; IFPEN, June 2021. URL <https://ifp.hal.science/hal-04033059>.
- S. Charousset and P. Gruet. Hiperwind deliverable report d6.1 - development of advanced operation and maintenance modelling. Technical report, H2020 HIPERWIND project (Grant agreement No 101006689), 2024.
- S. Charousset, P. Gruet, J. Lonchamp, N. Berrabah, and S. Dou. Hiperwind deliverable report d6.3 - quantification of the impacts of hiperwind on market value. Technical report, H2020 HIPERWIND project (Grant agreement No 101006689), 2024.
- C. Clément, P. Bozonnet, G. Vinay, P. Pagnier, A. Borrás Nadal, and J. Réveillon. Evaluation of Morison approach with CFD modelling on a surface-piercing cylinder towards the investigation of FOWT Hydrodynamics. *Ocean Engineering*, 251:111042, 2022.

- A. Cousin, M. Munoz Zuniga, L. Franceschini, M. Guiton, C. Agrell, N. Dimitrov, O. Gramstad, S. Marelli, M. McWilliam, S. Schaer, E. Vanem, H. Wang, S. Winter, and M. Kelly. Hiperwind deliverable report D4.2 - methods for efficient ULS reliability calculations and their impact on probabilistic design. Technical report, H2020 HIPERWIND project (Grant agreement No 101006689), 2024.
- N. Dimitrov. Surrogate models for parameterized representation of wake-induced loads in wind farms. *Wind Energy*, 22(10):1371–1389, 2019. doi: 10.1002/we.2362.
- N. Dimitrov and T. Göçmen. Virtual sensors for wind turbines with machine learning-based time series models. *Wind Energy*, 25(9):1626–1645, 2022. doi: <https://doi.org/10.1002/we.2762>. URL <https://onlinelibrary.wiley.com/doi/abs/10.1002/we.2762>.
- N. Dimitrov and A. Natarajan. Application of simulated lidar scanning patterns to constrained gaussian turbulence fields for load validation. *Wind Energy*, 20(1):79–95, 2017. ISSN 1095-4244. doi: 10.1002/we.1992.
- N. Dimitrov and A. Natarajan. From scada to lifetime assessment and performance optimization: how to use models and machine learning to extract useful insights from limited data. *Journal of Physics: Conference Series*, 1222(1):012032, may 2019. doi: 10.1088/1742-6596/1222/1/012032. URL <https://dx.doi.org/10.1088/1742-6596/1222/1/012032>.
- N. Dimitrov and A. Natarajan. Wind farm set point optimization with surrogate models for load and power output targets. In *Journal of Physics: Conference Series*, volume 2018, page 012013. IOP Publishing, 2021. doi: 10.1088/1742-6596/2018/1/012013.
- N. Dimitrov, S. Marelli, and S. Schär. Hiperwind deliverable report D4.1 - novel surrogate modelling approaches for wind turbine reliability assessment. Technical report, H2020 HIPERWIND project (Grant agreement No 101006689), 2022.
- N. Dimitrov, M. Kelly, M. McWilliam, M. Guiton, A. Cousin, P. Joulin, M. Mayol, M. Munoz-Zuniga, L. Franceschini, A. Lovera, E. Fekhari, E. Ardillon, C. Peyrard, M. Bakhoday-Paskyabi, S. Marelli, S. Schar, E. Vanem, C. Agrell, O. Gramstad, and H. Wang. End-to-end wind turbine design under uncertainties: a practical example. *Journal of Physics: Conference Series*, 2767(8):082017, jun 2024a. doi: 10.1088/1742-6596/2767/8/082017. URL <https://dx.doi.org/10.1088/1742-6596/2767/8/082017>.
- N. Dimitrov, M. Pedersen, and Ásta Hannesdóttir. An open-source python-based tool for mann turbulence generation with constraints and non-gaussian capabilities. *Journal of Physics: Conference Series*, 2767(5):052058, jun 2024b. doi: 10.1088/1742-6596/2767/5/052058. URL <https://dx.doi.org/10.1088/1742-6596/2767/5/052058>.
- DNVGL. DNVGL-ST-0119 Floating Wind Turbine Structures: Technical Report. Technical report, DNVGL, Høvik, 2018.
- D. Dommermuth and D. K.-P. Yue. A high-order spectral method for the study of nonlinear gravity waves. *Journal of Fluid Mechanics*, 184:267 – 288, 1987. URL <https://api.semanticscholar.org/CorpusID:120305884>.

- S. Dou and N. Dimitrov. Modelling of turbine power and local wind conditions in wind farm using an autoencoder neural network. *Journal of Physics: Conference Series*, 2265(3):032069, may 2022. doi: 10.1088/1742-6596/2265/3/032069. URL <https://dx.doi.org/10.1088/1742-6596/2265/3/032069>.
- S. Dou, A. Pegalajar-Jurado, S. Wang, H. Bredmose, and M. Stolpe. Optimization of floating wind turbine support structures using frequency-domain analysis and analytical gradients. *Journal of Physics: Conference Series*, 1618(4):042028, Sept. 2020. ISSN 1742-6588, 1742-6596. doi: 10.1088/1742-6596/1618/4/042028. URL <https://iopscience.iop.org/article/10.1088/1742-6596/1618/4/042028>.
- P. Doubrawa, S. Sirnivas, and M. Godvik. Effects of upstream rotor tilt on a downstream floating wind turbine. *Journal of Physics: Conference Series*, 1934(1):012016, may 2021. doi: 10.1088/1742-6596/1934/1/012016. URL <https://dx.doi.org/10.1088/1742-6596/1934/1/012016>.
- C. Duhamel, C. Helbert, M. Munoz Zuniga, C. Prieur, and D. Sinoquet. A sur version of the bichon criterion for excursion set estimation. *Statistics and Computing*, 33(2):41, 2023.
- E. Fekhari, V. Chabridon, S. Marelli, E. Ardillon, and N. Dimitrov. Hiperwind deliverable report D4.3 - methods for adaptive calculation of fls loads and reliability, and their impact on probabilistic fatigue design. Technical report, H2020 HIPERWIND project (Grant agreement No 101006689), 2024a.
- E. Fekhari, V. Chabridon, J. Muré, and B. looss. Given-data probabilistic fatigue assessment for offshore wind turbines using bayesian quadrature. *Data-Centric Engineering*, 5:e5, 2024b. doi: 10.1017/dce.2023.27.
- A. C. Fitch, J. B. Olson, J. K. Lundquist, J. Dudhia, A. K. Gupta, J. Michalakes, and I. Barstad. Local and mesoscale impacts of wind farms as parameterized in a mesoscale nwp model. *Monthly Weather Review*, 140(9):3017–3038, 2012.
- E. Gaertner. Definition of the IEA wind 15-megawatt offshore reference wind turbine. Technical Report TP-5000-75698, NREL, Golden, CO, 2020.
- H. Glauert. 'Aerodynamic theory', chapter 'Airplane propellers', pages 169–360. "Springer, Berlin, Heidelberg", 1935.
- O. Gramstad, C. Agrell, E. Bitner-Gregersen, B. Guo, E. Ruth, and E. Vanem. Sequential sampling method using gaussian process regression for estimating extreme structural response. *Marine Structures*, 72:102780, 2020.
- M. Gräfe, M. R. El Amri, M. Guiton, and N. Dimitrov. Hiperwind deliverable report D4.5 - validation of the newly developed fls and uls distribution predictions and quantification of the resulting uncertainty reduction. Technical report, H2020 HIPERWIND project (Grant agreement No 101006689), 2024.
- A. N. Hahmann, O. García-Santiago, and A. Peña. Current and future wind energy resources in the north sea according to cmip6. *Wind Energy Science*, 7(6):2373–2391, 2022. ISSN 23667451, 23667443. doi: 10.5194/wes-7-2373-2022.

- C. Hirt and D. Nichols. Methods for Calculating Multi-Dimensional, Transient Free Surface Flows Past Bodies. In *First International Conference on Numerical Ship Hydrodynamics*. Gaithersburg, Maryland., 1975.
- IEC. IEC 61400-3 Wind turbines - Part 3 : Design requirements for offshore wind turbines. edition 1.0 2019-04. Standard, International Electrotechnical Commission, 2019a.
- IEC. International standard IEC 61400-1 ed. 4. wind turbines – part 1: Design requirements. *IEC 61400-1 Ed. 3*, 2019b.
- IEC. *Standard 61400–1, Edition 4. Wind turbine generator systems – Part 1: Design requirements*. International Electrotechnical Commission, Geneva, Switzerland, 2020.
- M. Ishii. *Thermo-fluid Dynamics Theory of two-Phase Flow*. Eyrolles, Collection de la direction des Etudes et recherches d'Electricité de France, 1975.
- ISO16281. Rolling bearings – method for calculating the modified reference rating life for universal load bearings rating life calculation, based on a systems approach to fatigue stresses : Iso ts 16281:2008(e). Technical report, ISO, 2008.
- ISO281. Rolling bearings – Dynamic load ratings and rating life: DS/ISO 281:2007. Technical report, ISO, 2007.
- C. Jacquet. Hiperwind deliverable report d6.2 - quantification of the impacts of hiperwind on offshore wind lcoe. Technical report, H2020 HIPERWIND project (Grant agreement No 101006689), 2024.
- H. M. Johlas, L. A. Martínez-Tossas, M. J. Churchfield, M. A. Lackner, and D. P. Schmidt. Floating platform effects on power generation in spar and semisubmersible wind turbines. *Wind Energy*, 24(8):901–916, 2021. doi: <https://doi.org/10.1002/we.2608>. URL <https://onlinelibrary.wiley.com/doi/abs/10.1002/we.2608>.
- B. J. Jonkman and J. Buhl, M. L. Turbsim user's guide. Technical report, National Renewable Energy Laboratory, 9 2006. URL <https://www.osti.gov/biblio/891594>.
- J. Jonkman. Turbsim user's guide: Version 1.50. Technical report, National Renewable Energy Laboratory, 2009.
- J. Jonkman, S. Butterfield, W. Musial, and G. Scott. Definition of a 5-MW reference wind turbine for offshore system development. Technical report, National Renewable Energy Laboratory, 2009.
- P.-A. Joulin, M. L. Mayol, V. Masson, F. Blondel, Q. Rodier, M. Cathelain, and C. Lac. The actuator line method in the meteorological les model meso-nh to analyze the horns rev 1 wind farm photo case. *Frontiers in Earth Science*, 7, 2020.
- E. Jézéquel, M. Cathelain, V. Masson, and F. Blondel. Validation of wind turbine wakes modelled by the meso-nh les solver under different cases of stability. *Journal of Physics: Conference Series*, 1934(1):012003, may 2021. doi: 10.1088/1742-6596/1934/1/012003. URL <https://dx.doi.org/10.1088/1742-6596/1934/1/012003>.

- B. Kale, S. Buckingham, J. van Beeck, and A. Cuerva-Tejero. Implementation of a generalized actuator disk model into wrf v4.3: A validation study for a real-scale wind turbine. *Renewable Energy*, 197:810–827, 2022.
- M. Kelly. Flow acceleration statistics: a new paradigm for wind-driven loads, towards probabilistic turbine design. *Wind Energy Science*, in press, 2024. doi: 10.5194/wes-8-975-2023.
- M. Kelly and E. Vanem. Hiperwind deliverable report D2.3 - environmental joint probability distributions and uncertainties. Technical report, H2020 HIPERWIND project (Grant agreement No 101006689), 2022. URL https://www.hiperwind.eu/-/media/sites/hiperwind/publications/hiperwind_deliverable2-3_final.pdf.
- M. Kelly, R. A. Cersosimo, and J. Berg. A universal wind profile for the inversion-capped neutral atmospheric boundary layer. *Quarterly Journal of the Royal Meteorological Society*, 145(720): 982–992, 2019. ISSN 1477870x, 00359009. doi: 10.1002/qj.3472.
- M. Kelly, S. J. Andersen, and A. Hannesdóttir. Statistical impact of wind-speed ramp events on turbines, via observations and coupled fluid-dynamic and aeroelastic simulations. *Wind Energy Science*, 6(5):1227–1245, 2021. doi: 10.5194/wes-6-1227-2021.
- T. Kim, A. Natarajan, A. Lovera, E. Julan, C. Peyrard, M. Capaldo, G. Huwart, P. Bozonnet, and M. Guiton. A comprehensive code-to-code comparison study with the modified IEA15MW-Umaine floating wind turbine for H2020 Hiperwind project. *Journal of Physics: Conference Series*, 2265(4):042006, may 2022. doi: 10.1088/1742-6596/2265/4/042006. URL <https://dx.doi.org/10.1088/1742-6596/2265/4/042006>.
- G. C. Larsen, H. A. Madsen, K. Thomsen, and T. J. Larsen. Wake meandering: a pragmatic approach. *Wind Energy: An International Journal for Progress and Applications in Wind Power Conversion Technology*, 11(4):377–395, 2008. doi: 10.1002/we.267.
- T. Larsen and A. Hansen. *How 2 HAWC2, the user's manual*. Number 1597(ver. 13-0)(EN) in Denmark. Forskningscenter Risoe. Risoe-R. Technical University of Denmark, 2023. ISBN 978-87-550-3583-6.
- T. Larsen, G. Larsen, H. Aagaard Madsen, and S. Petersen. Wake effects above rated wind speed. an overlooked contributor to high loads in wind farms. In *Scientific Proceedings. EWEA Annual Conference and Exhibition 2015*, pages 95–99. European Wind Energy Association (EWEA), 2015. ISBN 9782930670003. EWEA Annual Conference and Exhibition 2015 ; Conference date: 17-11-2015 Through 20-11-2015.
- C. Le Cunff, J.-M. Heurtier, L. Piriou, C. Berhault, T. Perdrizet, D. Teixeira, G. Ferrer, and J.-C. Gilloteaux. Fully Coupled Floating Wind Turbine Simulator Based on Nonlinear Finite Element Method: Part I — Methodology. In *International Conference on Offshore Mechanics and Arctic Engineering*, volume Volume 8: Ocean Renewable Energy, page V008T09A050, 06 2013. doi: 10.1115/OMAE2013-10780. URL <https://doi.org/10.1115/OMAE2013-10780>.
- A. Lovera, E. Fekhari, B. Jézéquel, M. Dupoirion, M. Guiton, and E. Ardillon. Probabilistic wake induced wind parameters and clustering for load analysis. In *Proceedings of the WAKE 2023 conference*, 2023.

- R. MacCamy and R. Fuchs. Wave forces on piles: a diffraction theory. beach erosion. Technical report, Board office of the chief of engineers. Department of the Army, Corps of engineers, 1954.
- F. J. Madsen, A. Pegalajar-Jurado, and H. Bredmose. Performance study of the QuLAF pre-design model for a 10 MW floating wind turbine. *Wind Energy Science*, 4(3):527–547, Sept. 2019. ISSN 2366-7451. doi: 10.5194/wes-4-527-2019. URL <https://wes.copernicus.org/articles/4/527/2019/>.
- M. Y. Mahfouz, M. Salari, S. Hernandez, H. Bredmose, and A. Pegalajar-Jurado. D1.3 Public design and FAST models of the two 15MW floater, 2020.
- S. Marelli and B. Sudret. UQLab: A Framework for Uncertainty Quantification in MATLAB. In *The 2nd International Conference on Vulnerability and Risk Analysis and Management (ICVRAM 2014)*, United Kingdom, 2014.
- B. Maronga, S. Banzhaf, C. Burmeister, T. Esch, R. Forkel, D. Fröhlich, V. Fuka, K. F. Gehrke, J. Geletič, S. Giersch, T. Gronemeier, G. Groß, W. Heldens, A. Hellsten, F. Hoffmann, A. Inagaki, E. Kadasch, F. Kanani-Sühring, K. Ketelsen, B. A. Khan, C. Knigge, H. Knoop, P. Krč, M. Kurppa, H. Maamari, A. Matzarakis, M. Mauder, M. Pallasch, D. Pavlik, J. Pfafferott, J. Resler, S. Rissmann, E. Russo, M. Salim, M. Schrempf, J. Schwenkel, G. Seckmeyer, S. Schubert, M. Sühring, R. von Tils, L. Vollmer, S. Ward, B. Witha, H. Wurps, J. Zeidler, and S. Raasch. Overview of the palm model system 6.0. *Geoscientific Model Development*, 13(3):1335–1372, 2020. doi: 10.5194/gmd-13-1335-2020. URL <https://gmd.copernicus.org/articles/13/1335/2020/>.
- M. McWilliam, N. Bonfils, N. Dimitrov, and S. Dou. Hiperwind deliverable report D3.1 - wind farm parameterization and turbulent wind box generation. Technical report, H2020 HIPERWIND project (Grant agreement No 101006689), 2022. URL https://www.hiperwind.eu/-/media/sites/hiperwind/publications/hiperwind_d3-1_corrected_19-01-2023.pdf.
- M. McWilliam, M. Kelly, and N. Dimitrov. Reference data and simulations for wind turbine loads due to extreme wind acceleration events. <https://doi.org/10.11583/DTU.22067816.v1>, 2023a.
- M. McWilliam, M. Kelly, and N. Dimitrov. The effect of filtered acceleration events on wind turbine loads. In *The Wind Energy Science Conference, 2023, Glasgow, United Kingdom*, 2023b.
- M. McWilliam, M. Kelly, N. Dimitrov, and J. Mann. Generating constrained turbulence for load simulations. Manuscript in preparation for publication, 2025a.
- M. McWilliam, M. Kelly, N. Dimitrov, and J. Mann. Loads comparison between iec extreme events and similar acceleration events at høvsøre. Manuscript in preparation for publication, 2025b.
- M. McWilliam, M. Munoz-Zuniga, M. Kelly, and N. Dimitrov. Support structure reliability analysis with stochastic transient events. Manuscript in preparation for publication, 2025c.
- D. Milano, C. Peyrard, M. Capaldo, D. Ingram, Q. Xiao, and L. Johanning. Impact of High Order Wave Loads on a 10 MW Tension-Leg Platform Floating Wind Turbine at Different

- Tendon Inclination Angles. In *International Conference on Offshore Mechanics and Arctic Engineering*, volume Volume 10: Ocean Renewable Energy, page V010T09A076, 06 2019. doi: 10.1115/OMAE2019-96243. URL <https://doi.org/10.1115/OMAE2019-96243>.
- S. Mimouni, F. Archambeau, M. Boucker, J. Lavieville, and C. Morel. A second order turbulence model based on a reynolds stress approach for two-phase boiling flow and application to fuel assembly analysis. *Nuclear Engineering and Design*, 240(9):2225–2232, 2010.
- J. Mirocha, B. Kosovic, M. Aitken, and J. Lundquist. Implementation of a generalized actuator disk wind turbine model into the weather research and forecasting model for large-eddy simulation applications. *Journal of Renewable and Sustainable Energy*, 6(1):013104, 2014.
- B. Molin. *Offshore Structure Hydrodynamics*. Cambridge Ocean Technology Series. Cambridge University Press, 2023.
- D. Moros, N. Berrabah, K. D. Searle, and I. G. Ashton. Maintenance & failure data analysis of an offshore wind farm. *Journal of Physics: Conference Series*, 2767(6):062006, jun 2024. doi: 10.1088/1742-6596/2767/6/062006. URL <https://dx.doi.org/10.1088/1742-6596/2767/6/062006>.
- X. Ning and M. Bakhoday-Paskyabi. Evaluation of sea surface roughness parameterization in meso-to-micro scale simulation of the offshore wind field. *Journal of Wind Engineering and Industrial Aerodynamics*, 242, 2023.
- X. Ning and M. Bakhoday-Paskyabi. Parameterization of wave-induced stress in large-eddy simulations of the marine atmospheric boundary layer. *Journal of Geophysical Research*, 2024.
- NREL. Openfast documentation, release v2.5.0. Technical report, National Renewable Energy Laboratory, 2021.
- B. Paz, L. Yi-chao, N. Marx Hermoso, W. Remigius, and A. B. Abrahamsen. Hiperwind deliverable report d5.2 - electrical grid model. Technical report, H2020 HIPERWIND project (Grant agreement No 101006689), 2023.
- A. Peña, R. R. Floors, A. Sathe, S.-E. Gryning, R. Wagner, M. Courtney, X. G. Larsén, A. N. Hahmann, and C. B. Hasager. Ten years of boundary-layer and wind-power meteorology at Høvsøre, Denmark. *Boundary-layer Meteorology*, 158(1):1–26, 2016. ISSN 15731472, 00068314. doi: 10.1007/s10546-015-0079-8.
- J. G. Pedersen, S.-E. Gryning, and M. Kelly. On the structure and adjustment of inversion-capped neutral atmospheric boundary-layer flows: Large-eddy simulation study. *Boundary-layer Meteorology*, 153(1):43–62, 2014. doi: 10.1007/s10546-014-9937-z. URL <http://dx.doi.org/10.1007/s10546-014-9937-z>.
- M. M. Pedersen, A. M. Forsting, P. van der Laan, R. Riva, L. A. A. Romàn, J. C. Risco, M. Friis-Møller, J. Quick, J. P. S. Christiansen, R. V. Rodrigues, B. T. Olsen, and P.-E. Réthoré. Pywake 2.5.0: An open-source wind farm simulation tool. Technical report, DTU Wind, Technical University of Denmark, 2 2023. URL <https://gitlab.windenergy.dtu.dk/TOPFARM/PyWake>.

- A. Pegalajar-Jurado, M. Borg, and H. Bredmose. An efficient frequency-domain model for quick load analysis of floating offshore wind turbines. *Wind Energy Science*, 3(2):693–712, Oct. 2018. ISSN 2366-7451. doi: 10.5194/wes-3-693-2018. URL <https://wes.copernicus.org/articles/3/693/2018/>.
- C. Peyrard, F. Robaux, A. Borrás-Nadal, P.-A. Joulin, L. Mayol, S. Eldevik, M. Guiton, A. Cousin, M. Benoit, N. Dimitrov, A. Lovera, and C. Ferreira. Aero-servo-hydroelastic model uncertainty. Technical report, H2020 HIPERWIND project (Grant agreement No 101006689), 2022. URL https://www.hiperwind.eu/-/media/sites/hiperwind/publications/hiperwind_d3-3_january2024.pdf.
- S. Popinet. A vertically-lagrangian, non-hydrostatic, multilayer model for multiscale free-surface flows. *J. Comput. Phys.*, 418:109609, 2020. URL <https://api.semanticscholar.org/CorpusID:213769156>.
- I. Reinwardt, L. Schilling, D. Steudel, N. Dimitrov, P. Dalhoff, and M. Breuer. Validation of the dynamic wake meandering model with respect to loads and power production. *Wind Energy Science*, 6(2):441–460, 2021. doi: 10.5194/wes-6-441-2021. URL <https://wes.copernicus.org/articles/6/441/2021/>.
- D. Remigius, B. Paz, Y. Liu, W. Remigius, and A. B. Abrahamsen. Hiperwind deliverable report d5.1 - component life models. Technical report, H2020 HIPERWIND project (Grant agreement No 101006689), 2023.
- O. Rodríguez-Hernández, J. D. Río, and O. Jaramillo. The importance of mean time in power resource assessment for small wind turbine applications. *Energy for Sustainable Development*, 30:32–38, 2016.
- C. Rosales and C. Meneveau. A minimal multiscale Lagrangian map approach to synthesize non-Gaussian turbulent vector fields. *Physics of Fluids*, 18(7):075104, 07 2006. ISSN 1070-6631. doi: 10.1063/1.2227003. URL <https://doi.org/10.1063/1.2227003>.
- Schaeffler. Tpi 176 : Lubrication of rolling bearings. Technical report, "Schaeffler Technologies", 2013.
- S. Schär, S. Marelli, and B. Sudret. Automatic manifold identification for mnarx models. MASCOT-NUM Annual Meeting 2023, Le Croisic, France, 2023a. Poster presentation.
- S. Schär, S. Marelli, and B. Sudret. Reliability analysis of wind turbines using manifold-narx surrogate models. Engineering Mechanics Institute 2023 International Conference (EMI 2023), Palermo, Italy, 2023b. Conference presentation.
- S. Schär, S. Marelli, and B. Sudret. An automated surrogate modelling approach for the uncertainty quantification of dynamical systems. MASCOT-NUM Annual Meeting 2024, Hyères, Giens Peninsula, France, 2023c. Poster presentation.
- S. Schär, S. Marelli, and B. Sudret. Emulating the dynamics of complex systems using autoregressive models on manifolds (mNARX). *Mechanical Systems and Signal Processing*, 208:110956, 2024. ISSN 0888-3270. doi: <https://doi.org/10.1016/j.ymssp.2023.110956>.

- B. Seiffert, G. Ducrozet, and F. Bonnefoy. Simulation of breaking waves using the high-order spectral method with laboratory experiments: Wave-breaking onset. *Ocean Modelling*, 119, 09 2017. doi: 10.1016/j.ocemod.2017.09.006.
- B. R. Seiffert and G. Ducrozet. A Comparative Study of Wave Breaking Models in a High-Order Spectral Model. In *International Conference on Offshore Mechanics and Arctic Engineering*, volume Volume 7B: Ocean Engineering, page V07BT06A050, 06 2017. doi: 10.1115/OMAE2017-61664. URL <https://doi.org/10.1115/OMAE2017-61664>.
- K. Shaler, B. Anderson, L. A. Martínez-Tossas, E. Branlard, and N. Johnson. Comparison of free vortex wake and blade element momentum results against large-eddy simulation results for highly flexible turbines under challenging inflow conditions. *Wind Energy Science*, 8(3): 383–399, 2023.
- B. K. Sriperumbudur, A. Gretton, K. Fukumizu, B. Schölkopf, and G. Lanckriet. Hilbert space embeddings and metrics on probability measures. *J. Mach. Learn. Res.*, 99:1517–1561, 2010.
- T. Stehly and P. Duffy. 2020 Cost of Wind Energy Review. Technical Report TP-5000-81209, NREL, Golden, CO, 2021.
- G. Steinfeld, B. Witha, M. Dörenkämper, and M. Gryschka. Hochauflösende large-eddy-simulationen zur untersuchung der strömungsverhältnisse in offshore-windparks. *promet – Meteorologische Fortbildung*, 39:163–180, 2015.
- B. Sudret. Global sensitivity analysis using polynomial chaos expansions. *Reliability Engineering & System Safety*, 93(7):964–979, July 2008. ISSN 09518320. doi: 10.1016/j.res.2007.04.002. URL <https://linkinghub.elsevier.com/retrieve/pii/S0951832007001329>.
- H. Sun, C. Qiu, L. Lu, X. Gao, J. Chen, and H. Yang. Wind turbine power modelling and optimization using artificial neural network with wind field experimental data. *Applied Energy*, 280:115880, 2020. doi: 10.1016/j.apenergy.2020.115880.
- J. Sutherland. *The Dynamics of Nonlinear Water Wave Groups*. PhD thesis, University of Edinburgh, 1992.
- The MathWorks Inc. Simulink: Simulation and model-based design, 2024. URL <https://www.mathworks.com/products/simulink.html>.
- A.-L. Tiberi-Wadier, A. Laugel, and M. Benoit. *Construction of the Numerical Wave Databases Anemoc-2 on the Mediterranean Sea and the Atlantic Ocean Through Hindcast Simulations Over the Period 1979–2010*, pages 127–143. Springer Singapore, Singapore, 2016. ISBN 978-981-287-615-7. doi: 10.1007/978-981-287-615-7_9. URL https://doi.org/10.1007/978-981-287-615-7_9.
- TR1281-2. Rolling bearings – Explanatory notes on ISO 281 – Part 2: Modified rating life calculation, based on a systems approach to fatigue stresses : DS/ISO/TR 1281-2:2008(e). Technical report, ISO, 2008.
- E. Vanem and T. Fazeres-Ferradosa. A truncated, translated Weibull distribution for shallow water sea states. *Coastal Engineering*, 172:104077:1–8, 2022.

- E. Vanem, E. Fekhari, N. Dimitrov, M. Kelly, A. Cousin, and M. Guiton. A joint probability distribution model for multivariate wind and wave conditions. In *Proc. 42nd International Conference on Ocean, Offshore and Arctic Engineering (OMAE 2023)*. American Society of Mechanical Engineers (ASME), June 2023a.
- E. Vanem, E. Fekhari, N. Dimitrov, M. Kelly, A. Cousin, and M. Guiton. A Joint Probability Distribution Model for Multivariate Wind and Wave Conditions. In *Volume 2: Structures, Safety, and Reliability*, page V002T02A013, Melbourne, Australia, June 2023b. American Society of Mechanical Engineers. ISBN 978-0-7918-8684-7. doi: 10.1115/OMAE2023-101961. URL <https://asmedigitalcollection.asme.org/OMAE/proceedings/OMAE2023/86847/V002T02A013/1166968>.
- E. Vanem, E. Fekhari, N. Dimitrov, M. Kelly, A. Cousin, and M. Guiton. A joint probability distribution for multivariate wind-wave conditions and discussions on uncertainties. *Journal of Offshore Mechanics and Arctic Engineering*, 146(6):061701:1–15, 2024a.
- E. Vanem, Ø. Lande, and E. Fekhari. A simulation study on the usefulness of the bernstein copula for statistical modeling of metocean variables. In *Proc. 43rd International Conference on Ocean, Offshore and Arctic Engineering (OMAE 2024)*. American Society of Mechanical Engineers (ASME), June 2024b.
- V. Venugopal. *Hydrodynamic force coefficients for rectangular cylinders in waves and currents*. PhD thesis, University of Glasgow, 2002.
- V. Venugopal, K. S. Varyani, and N. D. Barltrop. Wave force coefficients for horizontally submerged rectangular cylinders. *Ocean Engineering*, 33(11-12):1669–1704, 2006.
- H. Wang, O. Gramstad, S. Schär, S. Marelli, and E. Vanem. Comparison of probabilistic structural reliability methods for ultimate limit state assessment of wind turbines. *Structural Safety*, 111: 102502:1–16, 2024.
- B. J. West, K. A. Brueckner, R. S. Janda, D. M. Milder, and R. L. Milton. A new numerical method for surface hydrodynamics. *Journal of Geophysical Research*, 92:11803–11824, 1987. URL <https://api.semanticscholar.org/CorpusID:128695037>.
- J. Wheeler. Methods for Calculating Forces Produced by Irregular Waves. In *OTC Offshore Technology Conference*, volume All Days, pages OTC–1006–MS, 05 1969. doi: 10.4043/1006-MS. URL <https://doi.org/10.4043/1006-MS>.
- C. Yan, Y. Pan, and C. L. Archer. A general method to estimate wind farm power using artificial neural networks. *Wind Energy*, 22(11):1421–1432, 2019. doi: 10.1002/we.2379.
- B. Yildirim and N. Dimitrov. Hiperwind deliverable report D4.4 - floating wind turbine structural design procedure including sls. Technical report, H2020 HIPERWIND project (Grant agreement No 101006689), 2024.
- B. Yildirim, N. Dimitrov, A. B. Abrahamsen, and A. Kolios. A reduced order/simplified method for uncertainty quantification on the floating wind turbine design basis. *Journal of Physics: Conference Series*, 2767(8):082013, jun 2024. doi: 10.1088/1742-6596/2767/8/082013. URL <https://dx.doi.org/10.1088/1742-6596/2767/8/082013>.

9 Appendix: Additional resources

9.1 List of project deliverables

All public deliverables are available on www.hiperwind.eu and in the EU CORDIS document system, <https://cordis.europa.eu/project/id/101006689>. At the time of completion of this report, several deliverable reports were not formally released yet and the links to the reports are not available.

No.	Title	Dissemination level	Reference
D1.1	Supply of measurement data to the necessary parties from the appropriate platform	Confidential	
D1.2	Design brief for the use cases and models in engineering tools	Confidential	
D1.3	Baseline FLS and ULS simulation results from the use cases	Confidential	
-	Design brief of HIPERWIND offshore wind turbine cases: bottom fixed 10MW and floating 15MW	Public	Link
D2.1	Atmospheric-wave multi-scale flow modelling that will resolve the flow fields from mesoscale to farm/turbine scale	Public	Link
D2.2	Realistic representation of nonlinear wave conditions applicable for offshore wind turbine design	Public	Link
D2.3	Environmental joint probability distributions and uncertainties	Public	Link
D3.1	Wind farm parameterization and turbulent wind box generation	Public	Link
D3.2	Turbine loading and wake model uncertainty	Public	Link
D3.3	Aero-servo-hydro-elastic model uncertainty	Public	Link
D4.1	Novel surrogate modelling approaches for wind turbine reliability assessment.	Public	Link
D4.2	Methods for efficient ULS reliability calculations and their impact on probabilistic design	Public	
D4.3	Methods for adaptive calculation of FLS loads and reliability, and their impact on probabilistic fatigue design	Public	
D4.4	Floating wind turbine structural design procedure including SLS	Public	
D4.5	Validation of the newly developed FLS and ULS distribution predictions and quantification of the resulting uncertainty reduction	Public	

D5.1	Offshore wind turbine drivetrain component degradation and lifing models	Public	Link
D5.2	Quantification of the impact of electrical events on drivetrain mechanical component degradation.	Public	Link
D5.3	Validation of component lifing and reliability models including grid events	Public	
D5.4	Development and implementation of probabilistic and uncertainty quantification methods for reliability sensitivity analysis	Public	
D6.1	Advanced O&M model	Public	
D6.2	Quantification of the impacts of HIPERWIND on LCoE	Public	
D6.3	Quantification of the impacts of HIPERWIND on Market Value	Public	

9.2 List of software tools created in the project

Table 9.2: List of dedicated software tools developed during the project

Tool name	Short description	Link/reference
Hipersim	A tool for turbulence box generation and application of constraints. Available as a Python package under the MIT license.	Dimitrov et al. (2024b) Gitlab repository
SADLES:	This is a tool in Fortran equipped with processing codes in Python. The tool implements an Actuator Disc Model within the large eddy simulation (LES) component of WRF, without turbine control integration for now. There is a published paper	Bui et al. (2024)
WaveCoh:	This tool, developed in Python and MATLAB, enables wind-wave decomposition from offshore measurements or high-frequency model data. Additionally, it includes a theoretical wave-affected coherence function for generating turbulence boxes over the swell sea-state conditions. There is a published paper	Bakhoday-Paskyabi (2024)
Offline WRF-Swell coupling:	This tool features a few wave modules developed within WRF mesoscale model, incorporating various wave parameterizations to facilitate the offline coupling of the wave field to the overlying wind. It also includes a parameterization for wind-and-wave misalignment to enhance model accuracy and effectiveness.	We have submitted a paper on this work, and the tools will be released publicly as soon as possible.
O&M Optimization Tool	A tool combining short-term and long-term optimization routines to reduce maintenance costs through improving component replacement schedules.	Proprietary (EDF).
WAVEKit: Wind Asset Value Economics Toolkit	A comprehensive toolkit in Python for analyzing the economic viability of offshore wind energy projects. The tool chain provides tools and scripts to calculate the Levelized Cost of Energy (LCOE) and perform economic analysis.	Tool under review. Public release planned for November 2024.
otkerneldesign	A Python Package for sampling using the Kernel herding method. Based on the OpenTURNS uncertainty treatment platform.	Repository link

9.3 Links to additional project resources

The project website, containing links to deliverables, videos from event recordings, and other results:

www.hiperwind.eu

Hiperwind activities provided inputs to the [Probwind](#) project (funded by the Danish Energy Agency through the EUDP programme with grant number 64019-0587). Specifically, the proposed synthetic gust shapes in D10: Pre-standard for Probabilistic Design and Background Document are developed as part of Hiperwind: https://vbn.aau.dk/files/713487195/ProbWind_D10-Pre-standard_for_probabilistic_design_and_background_document_v2.pdf

9.4 External peer-reviewed publications generated by Hiperwind as of September 2024

N. Dimitrov and T. Göçmen. Virtual sensors for wind turbines with machine learning-based time series models. *Wind Energy*, 25(9):1626–1645, 2022. doi: <https://doi.org/10.1002/we.2762>. URL <https://onlinelibrary.wiley.com/doi/abs/10.1002/we.2762>

M. Kelly. Flow acceleration statistics: a new paradigm for wind-driven loads, towards probabilistic turbine design. *Wind Energy Science*, in press, 2024. doi: 10.5194/wes-8-975-2023

N. Dimitrov, M. Pedersen, and Ásta Hannesdóttir. An open-source python-based tool for mann turbulence generation with constraints and non-gaussian capabilities. *Journal of Physics: Conference Series*, 2767(5):052058, jun 2024b. doi: 10.1088/1742-6596/2767/5/052058. URL <https://dx.doi.org/10.1088/1742-6596/2767/5/052058>

N. Dimitrov, M. Kelly, M. McWilliam, M. Guiton, A. Cousin, P. Joulin, M. Mayol, M. Munoz-Zuniga, L. Franceschini, A. Lovera, E. Fekhari, E. Ardillon, C. Peyrard, M. Bakhoday-Paskyabi, S. Marelli, S. Schar, E. Vanem, C. Agrell, O. Gramstad, and H. Wang. End-to-end wind turbine design under uncertainties: a practical example. *Journal of Physics: Conference Series*, 2767(8):082017, jun 2024a. doi: 10.1088/1742-6596/2767/8/082017. URL <https://dx.doi.org/10.1088/1742-6596/2767/8/082017>

S. Dou and N. Dimitrov. Modelling of turbine power and local wind conditions in wind farm using an autoencoder neural network. *Journal of Physics: Conference Series*, 2265(3):032069, may 2022. doi: 10.1088/1742-6596/2265/3/032069. URL <https://dx.doi.org/10.1088/1742-6596/2265/3/032069>

E. Vanem, E. Fekhari, N. Dimitrov, M. Kelly, A. Cousin, and M. Guiton. A Joint Probability Distribution Model for Multivariate Wind and Wave Conditions. In *Volume 2: Structures, Safety, and Reliability*, page V002T02A013, Melbourne, Australia, June 2023b. American Society of Mechanical Engineers. ISBN 978-0-7918-8684-7. doi: 10.1115/OMAE2023-101961. URL <https://asmedigitalcollection.asme.org/OMAE/proceedings/OMAE2023/86847/V002T02A013/1166968>

E. Vanem, E. Fekhari, N. Dimitrov, M. Kelly, A. Cousin, and M. Guiton. A joint probability distribution model for multivariate wind and wave conditions. In *Proc. 42nd International Conference on Ocean, Offshore and Arctic Engineering (OMAE 2023)*. American Society of Mechanical Engineers (ASME), June 2023a

E. Vanem, Ø. Lande, and E. Fekhari. A simulation study on the usefulness of the bernstein copula for statistical modeling of metocean variables. In *Proc. 43rd International Conference on Ocean, Offshore and Arctic Engineering (OMAE 2024)*. American Society of Mechanical Engineers (ASME), June 2024b

E. Vanem, E. Fekhari, N. Dimitrov, M. Kelly, A. Cousin, and M. Guiton. A joint probability distribution for multivariate wind-wave conditions and discussions on uncertainties. *Journal of Offshore Mechanics and Arctic Engineering*, 146(6):061701:1–15, 2024a

H. Wang, O. Gramstad, S. Schär, S. Marelli, and E. Vanem. Comparison of probabilistic structural reliability methods for ultimate limit state assessment of wind turbines. *Structural Safety*, 111:102502:1–16, 2024

E. Vanem and T. Fazeres-Ferradosa. A truncated, translated Weibull distribution for shallow water sea states. *Coastal Engineering*, 172:104077:1–8, 2022

- S. Schär, S. Marelli, and B. Sudret. Reliability analysis of wind turbines using manifold-narx surrogate models. Engineering Mechanics Institute 2023 International Conference (EMI 2023), Palermo, Italy, 2023b. Conference presentation
- S. Schär, S. Marelli, and B. Sudret. Emulating the dynamics of complex systems using autoregressive models on manifolds (mNARX). *Mechanical Systems and Signal Processing*, 208: 110956, 2024. ISSN 0888-3270. doi: <https://doi.org/10.1016/j.ymssp.2023.110956>
- E. Fekhari, V. Chabridon, J. Muré, and B. looss. Given-data probabilistic fatigue assessment for offshore wind turbines using bayesian quadrature. *Data-Centric Engineering*, 5:e5, 2024b. doi: 10.1017/dce.2023.27
- M. McWilliam, M. Kelly, and N. Dimitrov. Reference data and simulations for wind turbine loads due to extreme wind acceleration events. <https://doi.org/10.11583/DTU.22067816.v1>, 2023a
- M. McWilliam, M. Kelly, N. Dimitrov, and J. Mann. Loads comparison between iec extreme events and similar acceleration events at høvsøre. Manuscript in preparation for publication, 2025b
- M. McWilliam, M. Kelly, N. Dimitrov, and J. Mann. Generating constrained turbulence for load simulations. Manuscript in preparation for publication, 2025a
- M. McWilliam, M. Munoz-Zuniga, M. Kelly, and N. Dimitrov. Support structure reliability analysis with stochastic transient events. Manuscript in preparation for publication, 2025c
- M. Bakhoday-Paskyabi, M. Krutova, H. Bui, and X. Ning. Multiscale simulation of offshore wind variability during frontal passage: Brief implication on turbines' wakes and load. *Journal of Physics: Conference Series*, 2362, 2022b
- M. Bakhoday-Paskyabi. Impact of swell waves on atmospheric surface turbulence: wave-turbulence decomposition methods. *Wind Energy Science*, 9, 2024
- H. Bui, M. B. Paskyabi, and M. M. Penchah. Implementation of a simple actuator disk for large-eddy simulation in the weather research and forecasting model (wrf-sadles v1.2) for wind turbine wake simulation. *Geoscientific Model Development*, 17, 2024
- X. Ning and M. Bakhoday-Paskyabi. Evaluation of sea surface roughness parameterization in meso-to-micro scale simulation of the offshore wind field. *Journal of Wind Engineering and Industrial Aerodynamics*, 242, 2023
- X. Ning and M. Bakhoday-Paskyabi. Parameterization of wave-induced stress in large-eddy simulations of the marine atmospheric boundary layer. *Journal of Geophysical Research*, 2024